Université de Lille – Sciences et Technologies

École Doctorale des Sciences de la Matière, du Rayonnement et de l’Environnement

Thèse de Doctorat

En vue de l’obtention du grade de

Docteur de l’Université de Lille

Discipline: Optique et Lasers, Physico-Chimie et Atmosphère

Spécialité : Chimie theorique, physique, analytique

Qicheng Wu

Développement de nouvelles méthodologies chimiométriques pour mieux prendre en compte les spécificités des données spectrales LIBS

Développement de nouvelles méthodologies chimiométriques pour mieux prendre en compte les spécificités des données spectrales LIBS Développement de nouvelles méthodologies chimiométriques pour mieux prendre en compte les spécificités des données spectrales LIBS

Soutenue le 15 décembre 2022:

Président du jury:

M. Pierre LANTERI	Professeur, Université de Lyon

Rapporteurs:

M. Jean-Marc BAELE	Professeur, Université de Mons, Belgique
M. Jorge PISONERO	Professeur, University of Oviedo, Spain

Examinateurs:

Mme Cécile FABRE	Maître de Conférences HDR, Université de Lorraine
M. Bruno BOUSQUET	Professeur, Université de Bordeaux

Invité:

M. Vincent MOTTO-ROS	Maître de Conférences HDR, Université de Lyon

Directeur de Thèse:

M. Ludovic DUPONCHEL	Professeur, Université de Lille

Université de Lille – Sciences et Technologies

École Doctorale des Sciences de la Matière, du Rayonnement et de l'Environnement

Thèse de Doctorat

En vue de l'obtention du grade de

Docteur de l'Université de Lille

Discipline: Optique et Lasers, Physico-Chimie et Atmosphère

Spécialité : Chimie theorique, physique, analytique

Qicheng Wu

Development of new chemometric methodologies to better take into account the specificities of LIBS spectral data

Développement de nouvelles méthodologies chimiométriques pour mieux prendre en compte les spécificités des données spectrales LIBS

Développement de nouvelles méthodologies chimiométriques pour mieux prendre en compte les spécificités des données spectrales LIBS

Soutenue le 15 décembre 2022:

Président du jury:

M. Pierre LANTERI	Professeur, Université de Lyon.

Rapporteurs:

M. Jean-Marc BAELE	Professeur, Université de Mons, Belgique,
M. Jorge PISONERO	Professeur, University of Oviedo, Spain.

Examinateurs:

Mme Cécile FABRE	Maître de Conférences HDR, Université de Loraine,
M. Bruno BOUSQUET	Professeur, Université de Bordeaux.

Invité:

M. Vincent MOTTO-ROS	Maître de Conférences HDR, Université de Lyon.

Directeur de Thèse:

M. Ludovic DUPONCHEL	Professeur, Université de Lille.

ACKNOWLEDGMENTS

The life of being a PhD student is about to finish, a little bit more than three years brought me many laughter and tears. I experienced many new things, living alone in a foreign country, trying to learn how to cook, trying to learn French, working with a group of people who speak different mother tongues but very passionate about their works…

I want to say thanks to many people, first of all, of course, professor Ludovic Duponchel. You gave me this opportunity, lead me to the world of chemometrics. I am extremely grateful for your patience, your enthusiasm and immense knowledge. This endeavor would not have been possible without your continuous support during these three years, especially the period of writing.

Then, many thanks to associate professor Raffaele Vitale for your help in the work, I am very thankful for all suggestions you provided.

Also, I would like to thank the China Scholarship Council for the opportunity and financial support of doing this PhD.

Really big thanks to my dear friend Hui, I couldn’t be able to finish this journey without your support and help, I couldn’t imagine my life without you. Thank you very much for all the nice food you prepared for me, and many nice times we spent together. For me, you are the family, may we have many more happy times in the future. Special thanks to Ali Eftekhari and Dario Cevoil, for your wise advice and the help. I would like to extend my sincere thanks to the students in the lab, thank all of you for the support and many happy times.

Great thanks to my family, especially my mon for the many long phone calls we had during this PhD to help me relaxing and the belief in me. Thanks should also go to my dear friends (张乃丹，汪雅静，佟彤) in China, for all those emotional support you provided thousands of miles away.

Qicheng Wu
吴祺琤

GENERAL REMARK

This thesis has been particularly impacted by the COVID health crisis that we have all endured. It is undeniable that it had repercussions on the research period of this thesis and particularly because it has not been possible to obtain additional months of funding to limit this impact. This does not detract from the quality of the work presented in this manuscript even if we would all have liked to have more time to go further in this very interesting research with strong expectations from the LIBS community.

Pr. L. Duponchel.

TABLE OF CONTENTS

LIST OF FIGURES

LIST OF TABLES

ABBREVIATIONS AND ACRONYMS

AAS: Atomic Absorption Spectroscopy
ANN: Artificial Neural Network
BP: Backpropagation
CCR: Correct Classification Rate
CF-LIBS: Calibration-Free Laser-Induced Breakdown Spectroscopy
CWT: Continuous Wavelet Transform
EDX: Energy-Dispersive X-Ray Spectroscopy
ICP-AES: Inductively coupled atomic emission spectroscopy
ICP-OES: Inductively Coupled Plasma Optical Emission Spectrometry
KNN: K-Nearest Neighbor
LA-ICP-MS: Laser Ablation Inductively Coupled Plasma Mass Spectrometer
LIBS: Laser-Induced Breakdown Spectroscopy
LOD: Limit of Detection
LSSVM: Least Squares Support Vector Machine
LTE: Local thermodynamic equilibrium
MLR: Multiple Linear Regression
MS: Mass Spectroscopy
Nd:YAG: Neodymium-doped Yttrium Aluminium Garnet
NIST: National Institute of Standards and Technology
NN: Neural Network
PC(s): Principal Component(s)
PCA: Principal Component Analysis
PLS: Partial Least Square
PLS-DA: Partial Least Square Discriminate Analysis
RF: Random Forest
RLA: Resonant Laser Ablation
SEM: Scanning Electron Microscopy
SIMCA: Soft Independent Modeling of Class Analog
SSD: Sum of Squared Difference
SVM: Supporter Vector Machine
SW: Spectral Windows

WT: Wavelet Transform

XRF: X-Ray Fluorescence

ABSTRACT

Today, Laser-Induced Breakdown Spectroscopy (LIBS) imaging is in full change. Indeed, always more stable instrumentations are developed, which significantly increases the signal quality and naturally the analytical potential of the technique for the characterization of complex and heterogeneous samples at the micro-scale level. Obviously, other intrinsic features such as a limit of detection in the order of ppm, a high field of view and high acquisition rate make it one of the most complete chemical imaging techniques to date. It is thus possible in these conditions to acquire several million spectra from one single sample in just hours. For sure, different chemometric approaches allow us today to propose a valorization of the acquired spectral data at both qualitative and quantitative levels. From a fundamental point of view, the main characteristics of the plasma, such as its temperature and electron density, have a significant impact on the intensities of the emission lines and even on the presence of some of them over a wide range of wavelengths. Of course, theoretical models could allow us, in some way and under very strict conditions, to correct the emission line intensities but this would remain a complex and very time-consuming task. In fact, we could only consider this strategy for a few spectra but not for hundreds of thousands or even millions of spectra of a LIBS hyperspectral imaging dataset that is available today. The first problem we have been working on in this thesis is to develop a robust predictive model to quantify an element from a LIBS spectrum independently of the plasma temperature and electron density. The second problem we addressed during this thesis is related to the intrinsic structure of a hyperspectral imaging dataset. Indeed, we always want to extract information on both major and minor compounds and even traces potentially contained in the hyperspectral data cube we have just acquired. However, minor compounds and traces are often present on a small number of pixels representing a very small variance in the spectral dataset. Unfortunately, the majority of chemometric algorithms exploiting the concept of expressed variance do not (or hardly) allow the detection of these compounds, especially when the signal-to-noise ratio is limited. It is therefore the second purpose of this thesis to introduce an algorithm which can give all compounds a chance to be detected regardless of their concentration.

RÉSUMÉ

Aujourd'hui, l'imagerie LIBS est en pleine évolution. En effet, des instruments toujours plus stables sont développés, ce qui augmente significativement la qualité du signal et naturellement le potentiel analytique de la technique pour la caractérisation d'échantillons complexes et hétérogènes à l'échelle du micron. Bien évidemment, d'autres caractéristiques intrinsèques telles qu'une limite de détection de l'ordre du ppm, un champ d’analyse élevé et une vitesse d'acquisition importante en font l'une des techniques d'imagerie chimique les plus complètes à ce jour. Il est ainsi possible dans ces conditions d'acquérir plusieurs millions de spectres d'un seul échantillon en quelques heures. Certes, différentes approches chimiométriques nous permettent aujourd'hui de proposer une valorisation des données spectrales acquises tant au niveau qualitatif que quantitatif. D'un point de vue fondamental, les principales caractéristiques du plasma, telles que sa température et sa densité électronique, ont un impact significatif sur les intensités des raies d'émission et même sur la présence de certaines d'entre elles sur une large gamme de longueurs d'onde. Bien sûr, des modèles théoriques pourraient nous permettre, d'une certaine manière et sous des conditions très strictes, de corriger les intensités des raies d'émission mais cela resterait une tâche complexe et très longue. En fait, nous ne pourrions envisager cette stratégie que pour quelques spectres, mais pas pour des centaines de milliers, voire des millions de spectres d'un ensemble de données d'imagerie hyperspectrale LIBS disponibles aujourd'hui. C'est le premier problème sur lequel nous avons travaillé dans cette thèse dans le but de développer un modèle prédictif robuste pour quantifier un élément à partir d'un spectre LIBS indépendamment de la température du plasma et de la densité électronique. Le deuxième problème que nous avons abordé au cours de cette thèse est lié à la structure intrinsèque d'un jeu de données d'imagerie hyperspectrale. En effet, nous souhaitons toujours extraire des informations sur les composés majeurs et mineurs et même sur les traces potentiellement contenues dans le cube de données hyperspectrales que nous venons d'acquérir. Cependant, les composés mineurs et les traces sont souvent présents sur un petit nombre de pixels représentant une très faible variance dans le jeu de données spectrales. Malheureusement, la majorité des algorithmes chimiométriques exploitant le concept de variance exprimée ne permettent pas (ou peu) la détection de ces composés, surtout lorsque le rapport signal/bruit est limité. C'est donc le second objectif de cette thèse que d'introduire un algorithme permettant de donner une chance à tous les composés d'être détectés quelle que soit leur concentration.

INTRODUCTION

As a spectroscopic technique, LIBS has numerous applications in many areas and this technique has showed its ability to the world. Compared with some other commonly used spectroscopy, LIBS has many advantages, such as the fast data acquisition, no sample preparation, capable of analysing sample in gas, liquid and solid form and the amazing ability to analysis almost all the elements. LIBS showed great power in qualitative analysis, however, the quantitative analysis is perhaps its Achilles's heel if we are very strict about the origin of the signal. The reason for making LIBS quantitative analysis a bit complex is the varying nature of the plasma, with different temperature and electron density coming from matrix effects. Although temperature and electron number density information are important, the vast majority of studies either do not consider them or simplify the effects they might have on the analysis due to the difficulty of acquiring them. Of course, there are different solutions for this issue, from using standard reference to complex physical calibrations, the coupling of other analytical instruments or the use of chemometric strategies. In reality, it is first not always possible to have references, the calibration is way too complex and not very practical for large datasets, and coupling with other instrument is not always as easy. Compared with previous solutions, chemometrics has significant advantages, for instance, no extra measurement needed, friendly to big data, and once the analysis model has been established, it is reusable. Among the many chemometric methods, artificial neural network (ANN) is an approach that has been quite quickly exploited in the field of LIBS and is suitable for large spectral datasets. Needless to mention the rise and popularity of ANN in many fields in recent years, the astonishing ability of dealing with non-linear complex problems makes it a celebrity in many scientific domains. The first objective of this thesis will be to develop a data processing strategy for LIBS spectra based on neural networks in order to propose a quantitative analysis that is robust to the potential variations of temperature and electron density of the plasma observed in complex and heterogeneous samples.

With the development of analytical instrument, the datasets we acquired become bigger and bigger, especially in LIBS hyperspectral imaging. For example, the datasets acquired in the 2000s contained a thousand spectra, whereas today they can contain more than 10 million spectra acquired in a few hours on a single sample. The instrumental developments have of course allowed this growth without compromising the quality of the spectra. During all these years, we could also observe a real increase in the skills of the LIBS community which opened to the concepts of chemometrics. From this very positive observation concerning LIBS imaging, we could then ask ourselves where is the problem? It comes in fact from the natural will of a researcher to want to discover everything of his complex sample, i.e. to detect both major, minor and even trace elements. Unfortunately, the majority of chemometrics algorithms based on the notion of variance do not allow to detect all of them and it is therefore the interest of this work to propose an alternative chemometrics strategy for a real exhaustive exploration of large LIBS imaging datasets.

This thesis manuscript will therefore be organized in three chapters. The first chapter will cover the principles of LIBS spectroscopy and chemometrics with a state of the art. The second chapter will report on the first experimental part of this thesis with the development of a neural network strategy for robust quantification in the face of temperature and electron density variations in the plasma. The third chapter, the second experimental part of this thesis, will develop a chemometric strategy for the detection of all chemical contributions of a complex sample independently of their explained variance within the considered imaging spectral dataset.

Chapter I

Laser induced breakdown spectroscopy and Artificial neural network: an overview and theoretical basis

I. LASER INDUCED BREAKDOWN SPECTROSCOPY AND ARTIFICIAL NEURAL NETWORK: AN OVERVIEW AND THEORETICAL BASIS

I.1. Laser-induced breakdown spectroscopy (libs)

I.1.1 Introduction of LIBS

Laser-Induced Breakdown Spectroscopy, known as LIBS, is an emission spectroscopy capable of analysis of multi-elements in basically any kinds of samples both qualitative and quantitative[1]. LIBS is a rather powerful spectroscopy for it is rapid, very little or no sample preparation needed, small quantity of sample required, analyzed in-situ and remotely. LIBS uses a high energy laser pulse on the sample to excite and ionize it to generate plasma, which will later produce spectra of the sample for analysis. Nd: YAG (Neodymium doped Yttrium Aluminum Garnet) lasers is one of the most commonly used lasers for LIBS. In general, the process of LIBS starts with the ablation of a small amount of sample from laser to generate plasma, the light from the plasma will then be directed and collected through an optical system, then the spectrum will be generated and detected by spectrometer for further analysis. The LIBS spectrum for the existence of different elements is distinguished by the characteristic wavelength of each element with the help of NIST (National Institute of Standards and Technology), and the quantity of each element can be told by measuring the intensities of spectrum. Further quantification of each element can be done with either calibration curves or through a calibration free LIBS (CF-LIBS). For the many advantages of LIBS, it has been applied in many areas, such as remote sensing[2][3][4], forensic[5][6][7][8], environmental analysis[9][10][11][12][13][14][15], ceramic raw materials in cultural heritage[16][17], wood products[18][19][20][21][22][23], industry[24][25][26], dominant and trace elements in alloys[27][28][29][30], aerosols[31][32][33][34][35] and many more.

I.1.2 History

After the invention of pulsed ruby laser in 1960, and the development of Q-switched laser in 1963, laser was capable of breakdown and generate laser plasma that can be used analytically, LIBS was born. In the 60s and 70s, LIBS have developed the abilities to detect samples in gas and liquid form, and theory and modeling were also developed to assist the better understanding of the laser-induced plasma. During the 70s and the early 80s, some applications for LIBS were appeared with the work from Los Alamos National Laboratory[36][37]. But it was not until in the 1980s with the huge improvement in laser, the introduction of Nd: YAG laser, and detector technology that made LIBS popular in different areas[38].

In the 90s, with the huge development of computer, laser and spectrometers, there were further development in instruments of LIBS. With the invention of calibration-free LIBS(CF-LIBS)[39] and the use of LIBS on NASA's Mars rover Curiosity around 2000, LIBS again caught people's attention and became one of the major techniques for qualitative and quantitative analysis[40].

I.1.3 Characterization of the laser parameters and the ablation process (Principle of LIBS)

I.1.3.1. Laser light

The description of laser light is frequently determined by terms like intensity, irradiance, fluence, radiant exposure, power of energy, density, volumetric energy density, and photo flux. All these terms can be decided with equations in Table I-1 needed.

Table I-1 Examples of basic expressions characterizing the laser beam, its intensity distribution, its propagation, and its focusing behavior[41]

Expression	Description	Equation number
$P = \iiint I_{pulse}(r,\lambda,\varphi)\, d\varphi d\lambda dr$	Light power (Ref[42], p.52)	T1.1
$E = \iiint I_{pulse}(r,\lambda,\varphi,t)\, d\varphi d\lambda dr dt$	Pulse energy (integrated over all distributions)	T1.2
$E = \int_{pulse} P(t)dt$	Power-energy relation of a pulse	T1.3
$t_0 = \frac{\int_{pulse} tP(t)dt}{\int_{pulse} P(t)dt}$	Time of the pulse center (i.e. when $I(t) = I_{max}$). This formula is valid for any pulse shape	T1.4
$I(t) = I_0 \exp(-\frac{t^2}{\tau_0^2})$	Gaussian temporal profile (Ref[36], p. 26)	T1.5
$\tau_p = 2\tau_0\sqrt{ln2}$	FWHM (full width at half-maximum) (Ref[36])	T1.6
$\bar{I} = \frac{\Phi_p}{\tau_p} = \int_{-\infty}^{+\infty} \frac{I(t)dt}{\tau_p} = 1.06 I_0$	Average pulse irradiance(Ref[36])	T1.7

$r = (\frac{2\lambda}{\pi})(\frac{f}{d})$	Laser radius, diameter, length, and divergence(assuming a cylindrical shape(Ref[43])	T1.8
$l = (\sqrt{\pi} - 1)\frac{\theta}{d}f^2$	Length and divergence assuming a cylindrical shape; $f = lengs\ focal\ length$(Ref[43])	T1.9
$w_0\theta = (\lambda/\pi)$	Diffraction-limit condition(Ref[42], p. 60)	T1.10
$M^2 = \frac{(w_0\theta)_{beam}}{(w_0\theta)_{diff\ lim}} = \frac{\pi d_0 D_l}{4f\lambda}$	Beam propagation factor($D_t = lens\ diameter$) (Ref[42], p, 60)	T1.11
$I = \frac{E_p \pi D_l^2}{4\tau_p f^2 \lambda^2}\left[\frac{1}{(M^2)^2}\right]$	Irradiance at the target (equation derived from the various definitions given)	T1.12
$spot\ size = \frac{0.61\lambda}{NA}$	Diffraction-limited spot size (Refs[44][45])	T1.13

I.1.3.2. Ablation

Ablation process is an important process for LIBS, and ablation efficiency is a parameter related to it. By definition, ablation process is the result of a complex interaction, involving laser parameters, sample properties, and plasma chemistry[41]. Table I-2 from review[41] listed the equations related to ablation efficiency. A simpler explanation is given with the example of surgery for medical application, as removing clots in the blood to restore the normal flow and at the same time maintain the integrity of blood vascular. As stated by its name, this parameter is an efficiency, like "quantum efficiency", has no units. It is defined by the ratio of number of atoms removed from the sample to the number of laser photons impinging on the surface[41]. However, in order to quantity this important parameter, another parameter, "ablation sensitivity" was introduced[46]. This parameter can be defined by the graphs in plotting the signal measured versus laser pulse energy, and has the unit of Volt/J, count/J and others if needed. Altogether ablation efficiency and ablation sensitivity are usually used to characterize the ablation process. Another thing that worth mentioning is that a similar definition used in LA-ICP-MS (Laser Ablation Inductively Coupled Plasma Mass Spectrometer) is called detection efficiency, which means the ratio of ions reaching the detector and the number of atoms released during laser ablation and takes into account aerosol losses during transportation as well as incomplete vaporization in the ICP (Inductively Coupled Plasma)[47].

Table I-2 Definitions related to the ablation process and parameters involved[41]

Expression	Description	Equation number
$\eta_{abl} = \frac{\rho\delta}{\Phi_0}$	Ablation efficiency (Ref[48], p. 611)	T2.1
$\eta_{abl} = \frac{\rho}{\mu_a\Phi_0}\ln\left(\frac{\Phi_0}{\Phi_{th}}\right)$	Ablation efficiency (blow-off model) (Ref[48], p.611)	T2.2
$\eta_{abl} = \frac{\Phi_0 - \Phi_{th}}{h_{abl}\Phi_0}$	Ablation efficiency (steady-state model) (Ref[48], p.611)	T2.3
$\eta_{abl} = \frac{Volume\ ablated}{Pulse\ energy} = \frac{S_l h_s}{Q_l}$	Ablation efficiency (Ref[49])	T2.4
$\eta_{abl} = \frac{Crater\ depth}{Pulse\ fluence} = \frac{h_s}{F_l} = \frac{h_s S_l}{Q_l}$	Ablation efficiency (Ref[50])	T2.5
$(\eta_{abl})_{VV} = \frac{m_{abl}\delta}{V_{abl}\Phi_0} = \frac{m_{abl}\delta S_l}{S_l\delta Q_l} = \frac{m_{abl}}{Q_l}$	Comparison T2.1 and T2.5	T2.6
$(\eta_{abl})_{SS} = \frac{S_l h_s}{Q_l} = \frac{m_{abl}}{\rho Q_l}$	Comparison T2.1 and T2.5	T2.7
$\eta_{abl} = \frac{Atoms\ removed\ per\ pulse}{Photons\ per\ pulse}$	Atom removal efficiency	T2.8
$\eta_{abl} = \frac{\rho_s S_l h_s N_A hv}{M_s Q_l} = \frac{\rho_s h_s}{F_l}\left(\frac{N_A hv}{M_s}\right)$	Atom removal efficiency	T2.9
$\frac{dm}{dt} = \frac{mass\ removed\ per\ pulse}{(unit\ area)(unit\ time)}$	Peak ablation rate(definition)	T2.10
$\dot{m}_{peak} = \frac{m_s}{S_l\tau_L}$	Peak ablation rate (Ref[51])	T2.11
$m_{ave} = \frac{m_s}{S_l\tau_L}(f_l\tau_L)$	Average ablation rate ($f_l = laser\ repetion\ rate$)	T2.12
$\frac{dh_s}{dt} = (\dot{h}_s)_{peak} = \frac{\dot{m}_{peak}}{\rho_s}$	Peak penetration rate (Ref[51])	T2.13
$(\dot{h}_s)_{ave} = \frac{\dot{m}_{ave}}{\rho_s}$	Average penetration rate	T2.14
$\dot{m} = \frac{\rho_0 d_T}{\tau_L}$	Mass removal rate (Refs[52][53][54]. [55][56][57])	T2.15
$\dot{m} = 110\left(\frac{\Phi_a}{10^{14}}\right)^{1/3}\lambda^{-4/3}$	Mass removal rate (Refs[52][53][54][55])	T2.16
$\dot{m} = 2.66\frac{(\psi)^{9/8}(I)^{1/2}}{(A)^{1/4}(\lambda)^{1/2}(\tau_L)^{1/4}}$	Mass removal rate (Ref. [57])	T2.17
$\psi \equiv \frac{A}{2[Z^2(Z+1)]^{1/2}}$	Parameter entering Eq. T2.17; A=atomic mass; Z=ionic charge(for singly charged ions Z=1)	T2.18

Ablation rate is another useful parameter in ablation process, it is characterized by the total mass ablated per unit time per unit area (gcm^{-2} s^{-1}). Since the laser sample interaction in LIBS is a rather complex process, the ablation mass and the useful ablation mass can be different, and the chemical properties of ablation in plasma can be different from sample in solid form. To conclude, a unified approach is still needed though the problems mention above.

I.1.4 Local thermodynamic equilibrium, theoretical equilibrium, plasma parameters and their evaluation

In this section, two of the most important parameters in LIBS will be introduced, electron number density (Ne) and plasma temperature(T), and also the concept of local thermodynamic equilibrium (LTE) will be discussed.

I.1.4.1. Local thermodynamic equilibrium (LTE)

Local thermodynamic equilibrium is defined as the plasma state reaching a local equilibrium. The best option would always be for the plasma to reach a complete local equilibrium. However, with all the other many processes to reach the perfect balance they all need to reach a single temperature, which is rather difficult criteria to meet. When the plasma is in a theoretical complete local equilibrium, the process of excitation of atoms by collision with electron is equal to the reverse deactivation process, and collisional ionization equal to three-body collisional recombination, and radiation emitted is equal to the radiation absorbed[41]. When the laws that used to describe the full thermodynamic equilibrium can apply, and at the same time the collisions dominate, a complete local thermodynamic equilibrium is reached. Since radiative transitions between low-lying levels (resonance transitions) are defined by high values of the Einstein coefficient of spontaneous emission, and the former are depopulated faster than the high levels, a radiative equilibrium is easier to reach. If these levels are not considered, a partial local thermodynamic equilibrium is reached[58].

Table I-3 shows equation related to LTE, among many equations, the first condition to be reached is the number of electron density should be less than a value to meet electron energy distribution function (EEDF), a Maxwell-Boltzmann distribution. Equation I-1tells us that for T = 6000 K, Ne should be less than 10^{21} cm^{-3}, and for T = 20 000 K, Ne should be less than one 6.7×10^{21}, and in most LIBS lab this can be acquired.

$$\varLambda = \frac{h}{\sqrt{2\pi mkT_e}} \qquad \textbf{I-1}$$

$$n_e(cm^{-1}) \ll \Lambda^{-3} = (\frac{2\pi kmT_e}{h^2})^{3/2} \qquad \textbf{I-2}$$

An ideal plasma source is of course preferred, however, compared with ICP, laser-induced plasma is not really an ideal plasma source for spectroscopy, to solve this problem, equation I-2is needed. When an energy is suddenly applied to a system that already reach equilibrium, an extra period of time will be needed for the new equilibrium to reach, and this period of time is called relaxation time τ_{relax}, and defined by equation I-3,

$$\tau_{relaxation} = \frac{\bar{N}}{v} = \frac{(Average\ numnber\ of\ gas\ kinetic\ collisions\ per\ molecule\ needed\ to\ exchange\ energy)}{(number\ of\ gas\ kinetic\ collisions\ per\ second\ per\ molecule)} \qquad \textbf{I-3}$$

Kinetic model were also brought into the LIBS for cases[59] to study the distribution of electron energy. These consideration are all list in Table I-3, and among them all, the first equation is McWhirter criterion[58], perhaps one if the most important equation to determine the LTE in LIBS. This criterion is derived from the form[60] which is originally used to minimum Ne necessary to ensure partial and complete thermodynamic equilibrium, and also requires the collisional rate larger than the radiative one at least 10 times[58]. There are many different applications that derived from McWhirter criterion and discussions, a conclusion could reach is that the only use of it is not enough to determine LTE.

Table I-3 Most useful and commonly reported equations and definitions in the LIBS plasma diagnostics[41]

Expression	Description	Equation number
$n_e \geq 1.6 \times 10^{12} (T)^{1/2} (\Delta E)^3$	McWhirter crierions, n_e(cm^{-3}); T (K); ΔE (eV) (Refs.[58][61])	T3.1
$\frac{T(t+\tau_{rel}) - T(t)}{T(t)} \ll 1$	Additional temporal condition for T; τ_{rel} =relaxation time	T3.2
$\frac{n_e(t+\tau_{rel}) - n_e(t)}{n_e(t)} \ll 1$	Additional temporal condition for n_e	T3.3
$\frac{T_e(x) - T_e(x+\lambda)}{T_e(x)} \ll 1$	Additional spatial condition for T; λ = diffusion length during τ_{rel}	T3.4
$\frac{n_e(x) - n_e(x+\lambda)}{n_e(x)} \ll 1$	Additional spatial condition for n_e	T3.5
$\sigma_{lu} = \left(\frac{2\pi^2}{\sqrt{3}}\right)\left(\frac{f_{lu}\bar{g}e^4}{\frac{1}{2}m_e v_i^2 \Delta E_{ul}}\right)$	Cross-section of inelastic collisions (cm^2); ΔE (erg); e (statC); v_i = electron velocity (cm s^{-1}) (Ref. [61])	T3.6
$X_{lu}(T_e) = n_e(\sigma_{lu}v) = 4\pi \frac{f_{lu}e^4 n_e(\bar{g})}{\Delta E_{ul}} \left(\frac{2\pi}{3mkT_e}\right)^{1/2} exp\left(-\frac{\Delta E_{ul}}{kT_e}\right)$	Collisional excitation rate (s^{-1}); m = electron mass (g); k (erg K^{-1}) (Ref. [61])	T3.7
$\tau_{rel} \approx \frac{1}{n_e(\sigma_{lu}v_e)} = \frac{6.3 \times 10^4}{n_e f_{lu} \langle\bar{g}\rangle} \Delta E_{ul}(kT_e)^{1/2} exp\left(\frac{\Delta E_{ul}}{kT_e}\right)$	Relaxation time; the numerical value results from ΔE and kT in n_e (Ref. [61])	T3.8
$\lambda = (D\tau_{rel})^{1/2} \approx 1.4 \times 10^{12} \frac{(kT)^{3/4}}{n_e}$	Diffusion length (cm); D = diffusion coefficient (cm^{2}s^{-1}); ΔE and kT in eV; n_e (cm-3) (Ref. [61])	T3.9
$\varepsilon_{line} = \left(\frac{A_{ul}n_u hv}{4\pi}\right)$	Spectrally integrated line emissivity (Wcm^{-3}sr^{-1}) (Refs. [62][63])	T3.10

$B_v(v) = \left(\frac{A_{ul} n_u h v}{4\pi}\right) S_v(v) \cdot \left(\frac{1}{K_v}\right)$	Line spectral radiance (Wcm^{-2}sr^{-1}Hz^{-1}) (Ref. [64])	T3.11
$K_v \equiv \frac{k^*(v)l}{\{1 - \exp[-k^*(v)l]\}} \equiv \frac{\tau(v)}{1 - \exp[-\tau(v)]}$	Self-absorption factor: (K_v), optical depth: $\tau(v)$ (Ref. [64])	T3.12
$B_{thermal} = (B)_{v_0}^{Plank}(T_p) \cdot \int_{line} \{1 - \exp[-k^*(v)l]\}$	Thermal line radiance (Wcm^{-2}sr^{-1}) k* = net absorption coefficient (Refs. [65][66][64])	T3.13
$I_{\lambda,ul} = F_{exp} \frac{8\pi hc}{\lambda^3} \left(\frac{n_u g_l}{n_l g_u}\right) \int \{1 - \exp[-k^*(v)l]\}$	Integrated line irradiance (Wm^{-2}) (Ref. [67], Chap. 3, p. 137—note a misprint here in the g's ratio)	T3.14
$\alpha_j = \frac{n_{i,j}}{n_j} = \frac{n_{i,j}}{n_{i,j} + n_{a,j}} \frac{n_{i,j}}{n_{a,j}} = \frac{\alpha_j}{(1 - \alpha_j)}$	Definition of degree of ionization, $n_{i,j}$= $n_{a,j}$ = ions (atoms) number density of species j (Ref. [68], p. 157)	T3.15
$\frac{(I_{ul}^+)_j}{(I_{ul})_j} = \left(\frac{g_u^+ A_{ul}^+ h v_{ul}^+}{g_u A_{ul} h v_{ul}}\right) [\frac{\alpha_j}{(1 - \alpha_j)}] \left(\frac{Z_{a,j}}{Z_{i,j}}\right) exp\left(\frac{E_u - E_u^+}{kT}\right)$	Ion-to-neutral ratio,(+) refers to ion parameters, E_u^+ = from ion ground level (Ref. [68], p. 158)	T3.16
$log \frac{\alpha_j}{(1 - \alpha_j)} = log \frac{S_{n,j}}{n_e}$ $= -log n_e + \frac{3}{2} log T - \frac{5040 E_{i,j}}{T}$ $+ log\left(\frac{Z_{a,j}}{Z_{i,j}}\right) + 15.684$	Relation between ion-to-neutral ratio and ionization degree (both T and n_e can be evaluated) (Ref. [68], p. 164)	T3.17
$n_e \frac{n_i}{n_a} = \frac{2(2\pi m_e k T_{ion})^{3/2}}{h^3} \frac{Z_i}{Z_a} exp\left(-\frac{E_{ion} - \Delta E_{ion}}{k T_{ion}}\right)$	Saha–Boltzmann equilibrium, T$_i$ = ionization temperature; ΔE_{ion} = depression of E_{ion} due to Debye shielding (Refs. [65][68][66])	T3.18
$I_{ul} = F_{exp} A_{ul} \frac{g_u}{2Z_i} [\frac{h^3}{(2\pi mk)^{3/2}}] n_e n_i T_{ion}^{-3/2} exp\left(\frac{E_{ion} - \Delta E_{ion}}{k T_{ion}}\right.$ $\left.- \frac{E_u}{k T_{exc}}\right)$	Line ''intensity'', (energy/unit time - unit volume) (Refs. [69][70])	T3.19
$\varepsilon_{\lambda,cont} = \left(\frac{16\pi e^6}{3c^2\sqrt{6\pi m^3 k}}\right) \frac{n_e n_i}{\lambda^2 \sqrt{T_e}} \left\{\xi \left[1 - exp\left(-\frac{hv}{kT_e}\right)\right]\right.$ $\left.+ Gexp\left(-\frac{hv}{kT_e}\right)\right\}$	Continuum spectral ''intensity'' (energy/unit time - unit volume - wavelength) (Refs. [69][70])	T3.20
$\frac{I_{ul}}{\varepsilon_c}(\lambda) = \left(\frac{h^4 3^{3/2} c^3}{256\pi^3 e^6 k}\right) \frac{A_{ul} g_u}{Z_i} \frac{1}{T_e}$ $\frac{exp\left(-\frac{E_i - \Delta E_i}{kT_e}\right) exp\left(\frac{-E_u}{kT_{exc}}\right)}{\left[\xi\left(1 - exp\frac{hc}{\lambda k T_e}\right) + Gexp\left(-\frac{hc}{\lambda k T_e}\right)\right]} \left(\frac{\lambda}{\Delta\lambda_{meas}}\right)$	Line-to-continuum ratio (note that temperatures are kept different) (Refs. [69][70][71])	T3.21
$n_e = \left(\frac{\Delta\lambda_{Stark} \cdot 10^9}{2.5\alpha_{1/2}}\right)^{3/2} = 8.02 \cdot 10^{12} \left(\frac{\Delta\lambda_{1/2}}{\alpha_{1/2}}\right)^{3/2}$	Stark width– n_e relation (linear Stark effect) (Refs. [72][73])	T3.22
$n_e = \frac{2(2\pi m_e kT)^{3/2}}{h^3} \frac{I_u A_{ul}^+ g_u^+}{I_u^+ A_{ul} g_u} exp\left(-\frac{E_{ion} + E_u^+ - E_u}{kT}\right)$	Ion-to-neutral ratio–n_e relation (see Eqs. T3.16, T3.18) (see also Ref. [67], Chap. 3, p. 133)	T3.23
$\Delta\lambda_{width} = w\left(\frac{n_e}{10^{16}}\right) [1 + 1.75 \cdot 10^{-4} n_e^{1/4} \alpha(1$ $- 0.068 n_e^{1/6} T^{-1/2})]$	Stark width– n_e relationship (quadratic Stark effect) (Refs. [74][75][76])	T3.24
$\Delta\lambda_{shift} = w\left(\frac{n_e}{10^{16}}\right) [\left(\frac{d}{w}\right) + 2.0 \cdot 10^{-4} n_e^{1/4} \alpha(1$ $- 0.068 n_e^{1/6} T^{-1/2})]$	Stark shift– n_e relationship (quadratic Stark effect) [Refs. [74](p. 135), [75][76]]	T3.25
$\frac{\delta v_D}{v_0} = \frac{\delta\lambda_D}{\lambda_0} = 7.16 \cdot 10^{-7} \sqrt{\frac{T}{M}}$	Doppler spectral profile, M (g/mol) = atomic mass; T (K) (Refs. [65][66])	T3.26

$\Delta\lambda_{res} \approx \frac{3}{16}\left(\frac{g_l}{g_u}\right)^{1/2}\left(\frac{\lambda_0^3 e^2 f_{lu}}{\pi^2 \varepsilon_0 m_e c^2}\right)n$	Resonance interaction broadening, ε_0 = vacuum permittivity ($C^2N^{-1}m^{-2}$); c = speed of light (ms^{-1}); n (m^{-3}) (Ref. [77])	T3.27
$\Delta\lambda_{vanderWaals,width} = 2.7C_6^{2/5}v^{3/5}n\frac{\lambda^2}{c}$	van der Waals broadening (width),C_6 = interaction constant (m^6s^{-1}) (Ref. [77])	T3.28
$\Delta\lambda_{vanderWaals,shift} = 0.98C_6^{2/5}v^{3/5}n\frac{\lambda^2}{c}$	van der Waals broadening (shift), v = relative velocity (ms^{-1}) (Ref. [77])	T3.29
$T = \frac{E_{u'} - E_u}{k} ln\left(\frac{I_{u'l'}g_u A_{ul}}{I_{ul}g_{u'}A_{u'l'}}\right) \frac{\Delta T}{T} = \frac{kT}{\Delta E}\left(\frac{\Delta R_1}{R_1} + \frac{\Delta R_A}{R_A}\right)$	Temperature evaluation from the line ratio and associated error (Refs. [65][66][62])	T3.30
$ln\left(\frac{I_{ul}^+ A_{ul} g_u}{I_{ul}A_{ul}^+ g_u^+}\right) = ln\left\{[\frac{2(2\pi m_e k)^{3/2}}{h^3}]\left(\frac{T^{3/2}}{n_e}\right)\right\} - \frac{(E_{ion} - \Delta E_{ion} + E_u^+ - E_u)}{kT}$	Saha–Boltzmann plot expression for evaluating plasma T_{exc} (Refs. [62][78] see also Ref. [67], Chap. 3, p. 132)	T3.31

I.1.4.2. Equilibrium expressions and diagnostic methods for the evaluation of T and Ne

An Ideal method could be described as follows[41],

1. It does not rely upon the assumption of LTE;
2. It does not require knowledge of the fundamental constants;
3. It does not necessitate the calibration of the detection system;
4. It should be relatively easy to implement in ordinary LIBS laboratory.

Which is difficult to find nevertheless. Table I-3 below shows many different methods for LTE diagnosis. All these method can be categorized as direct or indirect ones, and also active or passive ones by these two papers[79][72], respectively. Direct methods do not require assumptions of type and degree of equilibrium within the plasma to know the T and Ne. While the indirect methods require certain assumptions for the plasma system. Active methods can use external source to detect the plasma, while the passive would only use the plasma itself to measure parameters. Indirect methods require certain conditions to be met thus they suffer from the inherent contradiction. However, on the other side, these contradictions would allow the system to find certain consistency or a trend. All the different equations in Table I-2 and Table I-3 are for different conditions in real LIBS cases, things need to be mentioned here are, different temperatures appear in these equations, and extra attention should be paid to the unit of the parameters.

I.1.5 Experiment setup of LIBS

LIBS showed great potential in many different areas, and has many different sub-categories for different purposes. Like Resonant laser ablation (RLA) and resonantly enhanced LIBS (RE-LIBS) decrease the destruction of the sample compared to the conventional LIBS, and increased the LOD[80][81][82]. However, with the double-pulse laser and hyphenated LIBS, more information (both elemental information and molecular) about the sample can be acquired, or more information about the power. Micro-LIBS is also proposed to deal with the problem of the heterogeneous sample.

The stand-off LIBS for space exploration[83][84] and organic explosives[85][86] has also been developed. In the archaeological area, remote control LIBS is very handy[87][88]. Based on the information above, considerations about the set-up of LIBS will be discussed below in different sections and trying to cover as many aspects as possible with details.

I.1.5.1. Laser and focusing optics

In the area of description of laser light, many different terms were used to describe the properties of which, as it is more physics related, many details will not be discussed here in detail, Table I-1 listed equations for many parameters to characterize the laser itself. In the parts where it's more "chemical" related, the selection of ablation wavelength and pulse duration are popped out. As stated in article[36], the choice of wavelength should be based on the material, UV is better for ceramics, stones, and metal. In water analysis, due to the huge absorption of UV, IR would be a better choice. As for the pulse duration is concerned, a cleaner crater can be achieved with a ultrashort pulse, along with intense neutral atom emission[36]. The types of laser are dealt with for certain cases in these articles[89][90][91] for detailed study of interest. There isn't a single guideline for choice of laser light, but a general guideline could be given as: a single-mode profile should be used for single-shot analysis, and a multimode profile performs better for single-spot sampling. Based on one article[92], a single-mode Gaussian beam profile has the best performance in lateral resolution, depth profile, chemical mapping, and multimode profile should be used for trace analysis. Also, something not to be forgotten is the rise of fiber laser also showing good potential in LIBS, and providing higher power and higher repetition rate.

I.1.5.2. Optical transfer of plasma radiation, spectrometer and detection

Optical train is the term used for describing the radiation from plasma to detector, it has important role in signal collection efficiency of the entire system. In general, two types of optical train exist, one is the simplest when a commercial instrument is involved, which leaves one to trust the instrument for its optical quality and spectral characteristics. Another one is, of course, custom made, which gives one great opportunity to tune parameters to achieve better results. Detailed discussions about the merits of optical train are in books written by Gallou and Sirven[93], as this is not the purpose of this section.

I.1.6 Modeling LIBS spectra

It is important to model LIBS spectra, as the meaning of model here can be interpreted as the capability to give the description of the whole process from ablation to emission. Of course, it means having a detailed description of plasma-sample interaction, its plasma formation, its expansion, processes happened in plasma, collection of radiation, the signal generation, and the process from signal to concentration[94]. One could imagine a perfect model would be able to provide the estimation of the spectrum, all its characteristics, the detailed information of the sample composition and maybe many more deeper understandings of the whole system. Unfortunately, this ideal model is far to be real but almost perfect. Just take one tiny aspect of the whole system to clarify this, for instance, the interaction between laser and sample, according to the review[94]. The possible variations of conditions that such model has to consider are:

1. The sample can be in solid, liquid or gas state;
2. The sample can either absorb the laser or be transparent to it;
3. A solid sample can be a metal, a semiconductor or a dielectric with wide band gap;
4. The laser in use is just one pulse or a series of pulses;
5. Different laser wavelength can be used;
6. The duration of the laser pulse can be in nanosecond, picosecond or femtosecond time scale;
7. Is the laser characterized by its power or its beam shape;
8. Is the measurement under vacuum, atmosphere of certain gas, or a regular room atmosphere?
9. If the measurement uses two consecutive laser pulses, then the time delay between them can be adjusted for certain purposes;

The previous list shows that LIBS has a series of very complex situations to consider in experiment setup, and this is exactly because of the physical and chemical plasma processes are considered. It’s true that a complete system maybe probably can be determined in details but the balance of a perfect model and a model that is good enough for understanding should be reached. Thus, the model should try to use as few parameters as possible to simplify such process. Besides, those parameters should also be able to be observed in experiment. According to Bogaerts[95], all present plasma models are comprised, judiciously reduced problems, which nevertheless try capturing all the physical phenomena one wishes to understand. Putting this consideration in mind, the LIBS models being published are numerous. However, this is not a topic for this work, detailed studies having already published in reviews[95][96][97]. Fig. I-1 shows the scheme of the problems list above.

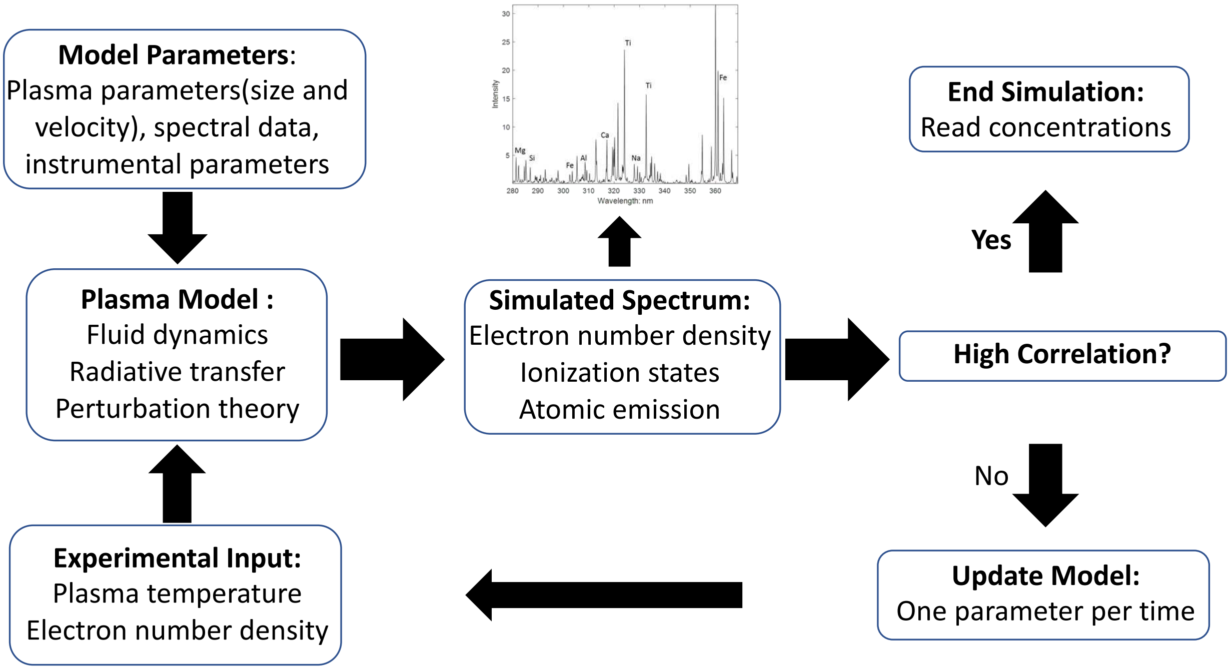

Fig. I-1 The scheme of problems for LIBS model

I.1.7 Quantitative LIBS

I.1.7.1. General considerations

The quantitative analysis of LIBS is a strong aspect of this method. However, it is not an easy task because of the very complex interactions between not only the laser and the sample, but also plasma and particles. The former interactions rely on the characteristics of laser and the properties of sample, the latter depends on time and space. All these combined together generate matrix effect, one thing that makes quantitative analysis difficult for LIBS. Despite probably is only well-known disadvantage of LIBS, LIBS has many advantages in the areas of qualitative chemical analysis. This method should not be seen as a technique with flaws. A statement made by Mermet[98] is perhaps very true about this fact, “regardless of the field of application , the acceptability of LIBS is still related to the problem of quantitation, involving accuracy, i.e., repeatability and trueness. ” . Though LIBS lacks of the ability of reproducibility, the great potential of this method cannot be ignored. A technique like LA-ICP-MS, a method that can be considered as a superstar method in analytical area, also has weaknesses when applied to trace analysis. Not to mention that LIBS can use internal standard calibration or external standard calibration for quantitative analysis. So, the technique cannot be seen as so weak considering the analytical techniques but also the fact improvements we can see in the field. As stated previously, LIBS has many applications in many fields, being the best advantage of LIBS. Also, the lack of sample preparation is yet another strong aspect of this method. The many publications of quantitative analysis with LIBS also showed that for certain specific cases, LIBS showed the ability of performing adequate analysis. To conclude, quantitation is possible with LIBS, but it is not perfect and this should be the area where focus goes.

I.1.7.2. Calibration and curves of growth

One of the important aspects that has been constantly mentioned in many books about spectrochemical analysis and plasma spectroscopy is the relation between thermal radiance $B_{thermal}$ of emission line as function of number density of atomic species in the plasma. Many equations related to this part are summarized in Table I-4, some of the very important part will be listed as follows.

Table I-4 Some equations related to the use of the spectral fluctuations approach in LIBS[94]

Expression	Description	Equation number
$\sigma_{sum} = \left\{[\sigma(B)_{p,\lambda_{off-peak}}]^2 + [\sigma(S)_{net,\lambda_0}]^2 + 2\theta\left[\sigma(B)_{p,\lambda_{off-peak}}\right][\sigma(S)_{net,\lambda_0}]\right\}^{1/2}$	This expression refers to a single isolated spectral line (signal S) superimposed on a flat background (signal B). The standard deviation resulting from the sum of the two signals contains the correlation coefficient θ	T4.1
$\sigma_{diff} = \left\{[\sigma(B)_{p,\lambda_{off-peak}}]^2 + [\sigma_{sum}]^2 - 2\theta\left[\sigma(B)_{p,\lambda_{off-peak}}\right][\sigma_{sum}]\right\}^{1/2}$	This expression relates the standard deviation of the difference of the two signals to the standard deviation of the sum and the correlation coefficient.	T4.2
$\theta = \frac{(\sigma_{sum})^2_{exp} + (\sigma_B)^2_{exp} - (\sigma_{diff})^2_{exp}}{2(\sigma_{sum})_{exp}(\sigma_B)_{exp}}$	The correlation coefficient cannot be calculated directly from the standard deviation of the sum of the two signals, but can be evaluated from the standard deviations of the sum of the difference and of the background.	T4.3
$(RSD)_{sum} = \frac{\sigma_{sum}}{(S+B)} = \frac{(\sigma_B^2 + \sigma_S^2 + 2\theta\sigma_B\sigma_S)^{1/2}}{(S+B)}$	This expression shows how the relative standard deviation of the sum of the analyte and background signals is related to the individual standard deviations and the correlation coefficient.	T4.4
$(RSD)_{sum} = \left[\frac{\sigma_P^2}{P^2} + \frac{\sigma_{P_{is}}^2}{P_{is}^2} - 2\theta\left(\frac{1}{PP_{is}}\right)\sigma_P\sigma_{P_{is}}\right]^{1/2}$	This expression is relevant when an internal standard is used to normalize the signal fluctuations. P and Pis refer to the signal peaks measured for the analytical line and that of the internal standard chosen.	T4.5

The relation related to the shape of the analytical calibration curves, usually known as the curves of growth. It is written as equations I-4 to I-7, this is the classical form of the emission and the analyte atomic number density in plasma.

$$B_{thermal} = (B)_{\lambda_0}^{Planck}(T_p) \int_{line} \{1 - exp[-k_\lambda^*(\lambda)l]\} \tag{I-4}$$

$$B_{thermal} = (B)_{\lambda_0}^{Wien}(T_p) \int_{line} \{1 - exp[-k_\lambda(\lambda)l]\} \tag{I-5}$$

$$k_\lambda(\lambda)l = \tau_\lambda(\lambda) \tag{I-6}$$

$$\int_{line} \{1 - exp[-k_\lambda(\lambda)l]\} \equiv A_t \tag{I-7}$$

In the equations above, the spectral radiance of the blackbody radiation given by either Planck or Wien laws at the given temperature is $(B)_{\lambda_0}(T_p)$(Wcm^{-2}sr^{-1}nm^{-1}). T_p and $k_\lambda^*(\lambda)$ are the wavelength dependent absorption coefficient with stimulated emission, while $k_\lambda(\lambda)$ is the wavelength dependent absorption coefficient without stimulated emission. $k(\lambda) = \sigma(\lambda)n$, and $\sigma(\lambda)$ is the wavelength dependent absorption cross section (cm^2) of the transition and n (cm^{-3}) is the atom number density. $\tau_\lambda(\lambda)$ stands for the optical thickness, l is the length of plasma in the direction of observation. The last equation above is called the total absorption factor, A_t.

When the self-absorption is ignored, such as in the situation where the optical thickness is more than the whole wavelength range of the line profile is $\ll 1$, then there will be the equation I-8

$$B_{thermal} = (B)_{\lambda_0}(T_p) \int_{line} k_\lambda (\lambda)l \tag{I-8}$$

When the optical thickness is thin, $B_{thermal}$ will be a linearly growth to the wavelength integrated absorption coefficient, and directly related to the atom number density. This is the linear part of the curves of growth. When the number density becomes bigger, the Doppler core of the line saturates, but the (Lorentzian) wings of the line are still optically thin[94]. The different values of parameter will result in the shape of the curves showing a plateau for some range of number density. In the end, the pressure broadening will effect on the wings, and $B_{thermal}$ grows with concentration with a slower rate, and this is the square root part of the curves[94].

When the condition is extreme, for instance, the optically condition is thicker than the unity, the blackbody value will be calculated in equation I-9, where the analytical dependence of the emission on analyte number density is lost.

$$B_{thernal} = (B)_{\lambda_0}(T_p) \tag{I-9}$$

The self-absorption parameter is an important parameter in deciding the shape of the curves of growth, and it is defined as follows (equation I-10),

$$K_\lambda \equiv \frac{k_\lambda(\lambda)l}{\{1 - exp[-k_\lambda(\lambda)l]\}} \equiv \frac{\tau_\lambda(\lambda)}{1 - exp[-\tau_\lambda(\lambda)]} \tag{I-10}$$

Error! Reference source not found. is one example of the curves of growth, this figure is s imulated by Jorg Hermann (Aix-Marseille Université, provided by professor Vincent Motto-Ros, Université Claude Bernard Lyon 1*)*.

The effect of self-absorption can be found in literatures[62][99][100][101]. The detailed calibration curves part can be found in paper[102].

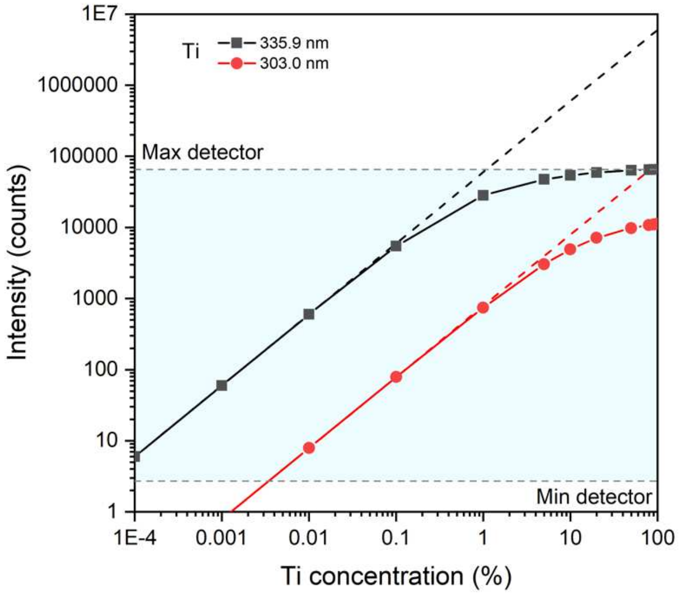

Fig. I-2 Curves of Growth

I.1.7.3. Analytical sensitivity and detection limits

The definition of detection limit is a subject of many theoretical and standardization processes. Being an emission spectroscopy, LIBS could benefit from the already existed many literatures. The most useful way for define the detection limits in LIBS would be signal-to -noise ratio(S/N) and signal-to-background ratio(S/B). The reasons for choosing these two parameters as the indicator are these are the most measured and reported during the optimization of LIBS measurements. In the LIBS spectrum, the response observed at the given wavelength is the sum of all the emissions of the sample(analyte). In a simple version, the average response of analyte after the subtraction of background would be taken as the signal. With the consideration of noise being present in both signal of target and background, the follow equations (I-11 to I-13) can be written:

$$\overline{X_S} = \overline{X_{S+B}} - \overline{X_B} \tag{I-11}$$

$$N_S = X_s - \overline{X_s} \tag{I-12}$$

$$N_B = X_B - \overline{X_B} \tag{I-13}$$

X_s and X_B are the responses for each spectrum, while $\overline{X_s}$ and $\overline{X_B}$ are the average responses related to signal and background. N_S and N_B represent their noises. S/N ratio is used to evaluate the quality of measurement. It is defined as the equation I-14 follows,

$$\frac{S}{B} = \frac{\bar{X}}{\sqrt{\bar{N}^2}} = \frac{\bar{X}}{\sqrt{\frac{(X-\bar{X})^2}{n}}} \tag{I-14}$$

This equation shows that the ratio of the signal amplitude to the noise amplitude is the S/N ratio, and the noise amplitude is defined as the root mean square value.

As for LOD, the classical definition[103] defines it as the concentration that results in a signal-to-background noise ratio of k(and in most cases, $k = 3$ is used). LOD can be written in the following equations I-15 to I-17,

$$X_L = \overline{X_B} + ks_B \tag{I-15}$$

$$X_L - \overline{X_B} = ks_B \tag{I-16}$$

$$c_L = LOD = \frac{ks_B}{b} \tag{I-17}$$

X_L is the smallest dissemble signal, s_B stands for the standard deviation of the background, b is the magnitude of the slope associated with the linear part of the calibration curve[94]. The signal-to-background and signal-to-background noise can also fit for detection limit as equation I-18 to I-20,

$$c_L = k(\frac{s_B}{\overline{X_B}})(\frac{\overline{X_B}}{b}) \qquad \textbf{I-18}$$

$$c_L = kc_0(RSD)_B\left(\frac{1}{\overline{X_s}/\overline{X_B}}\right) \qquad \textbf{I-19}$$

$$c_L = k(\frac{s_B}{\overline{X_B}})(BEC) \qquad \textbf{I-20}$$

$(RSD)_B$ is the relative standard deviation of the background, $k = 3$, BEC stands for the background equivalent concentration. For LIBS, equation I-19 is recommended for LOD.

I.1.8 Matrix effects and normalization approaches

I.1.8.1. Definition of matrix effects

As a spectroscopy with so many advantages, the only possible withdraw of LIBS could be the quantitative analysis, and that usually caused by matrix effects. Matrix effect is a common phenomenon observed in several analytical spectroscopies, which is usually the significant change in the observed signal at a given spectroscopic transition of the same element in two different samples with the same concentration. This difference can be categorized into the laser sample interactions difference that comes from differences in laser ablation mechanism and efficiency, or the changes in the plasma parameters (mainly the difference from temperature and electron number density), or a combination of both. In one sentence, this response can be affected by chemical, physical, spectral and instrumental reasons.

Different strategies to try to correct this matrix effects can be found in literature[94]. A short summary will be given here. Firstly, for any emission spectroscopy, the intermediate physical processes are the keys that lead to the understanding of the analytical signals, so is for LIBS. A relationship between the intensity of the spectral line and the number of atoms could be established if the constant excitation conditions can exist. However, the nature of the sample has huge influence on excitation conditions that leads to the famous matrix effects. There are two types of matrix effects: one is related to the entry of the sample into the plasma and the other one is what happened in the plasma[104]. These two types of effects are in the area of laser ablation and plasma modeling and diagnostics, respectively. Secondly, we can use a spectrochemical buffer, which means a substance that is added to sample in the effort of trying to reduce the influence of the composition and characteristics for the spectral line intensity. This method can be seen as an extension of the internal standard, and the adding part has a conflict with the general concept that LIBS requires little of no sample preparations. Thirdly, one can manage the measurement of spectral intensities with two methods: total energy and stead-state can be linked to LIBS from dc arc emission. Total energy requires a complete volatilization of the sample, and integration of spectral line over the entire evaporation time. "Stead-state" means that a constant feeding of the sample into the plasma. One paper[105] talked about the matrix effects with special reference to uncertainty and offered three groups of ways to reduce the effects: these strategies are matrix matching, internal calibration(or internal standard) and correction of the effect by either measuring the effects directly or some property of the matrix to have a correction function or a joint analyte calibration.

I.1.8.1.1. Consideration of the concentration units

When the matrix effects are only related to the entry material into the plasma, but not from what started inside the plasma, it can be assumed that the identical plasma conditions are reached, in this one the temperature of the plasma and the electron number density are the same and there is no chemical reaction in the plasma. At the same time, the same condition should also happen for the same detection parameters, which includes the same bandwidth, gain and integration time and many more. When the above-mentioned conditions are met, the concentration of a certain element in the matrix can be expressed in weight fraction or in mole fraction both in percent. Weight fraction carries the direct information of the sample, while the mole fraction requires the knowledge of the constitute of the sample to supply the information. For an emission spectral line, the intensity is now linked to the number of atoms in the sample. Fig. I-3 shows examples of two metal alloys samples with different concentrations, and equation I-21 can be used to express this plot. w_X and χ_X are the concentration of element X in the matrix in weight and mole fraction in percentage, respectively. R_{AX} stands for the ratio of atomic masses of M_A and M_X.

$$\chi_X = \frac{w_X R_{AX}}{1 + w_X(R_{AX} - 1)} \qquad \textbf{I-21}$$

For a single matrix that made up of element A and B with different concentrations, the plot should be look like the one at the up part of Fig. I-3. The dotted vertical line shows the results for different χ_A with the same w_A. The small inset figure shows the calibration curves of the same two elements with the choice of either the same χ_A or w_A. The left bottom plot shows the same weight fraction of Cu in Ag and Au will result in different signal intensities and calibration sensitivities. This same weight fraction is different with respect to the mole fractions, while the mole fraction plot simply just shows a single calibration sensitivity. The right bottom plot shows that with the same mole fraction of Cu, we have the same line intensity but only for two specific values of weight fractions. This figure shows that when we talk about the difference of examples as simple as two metal alloys, one should always keep in mind that the differences may not simply come from matrix effects, but also from the unit of the concentration with plays an important role.

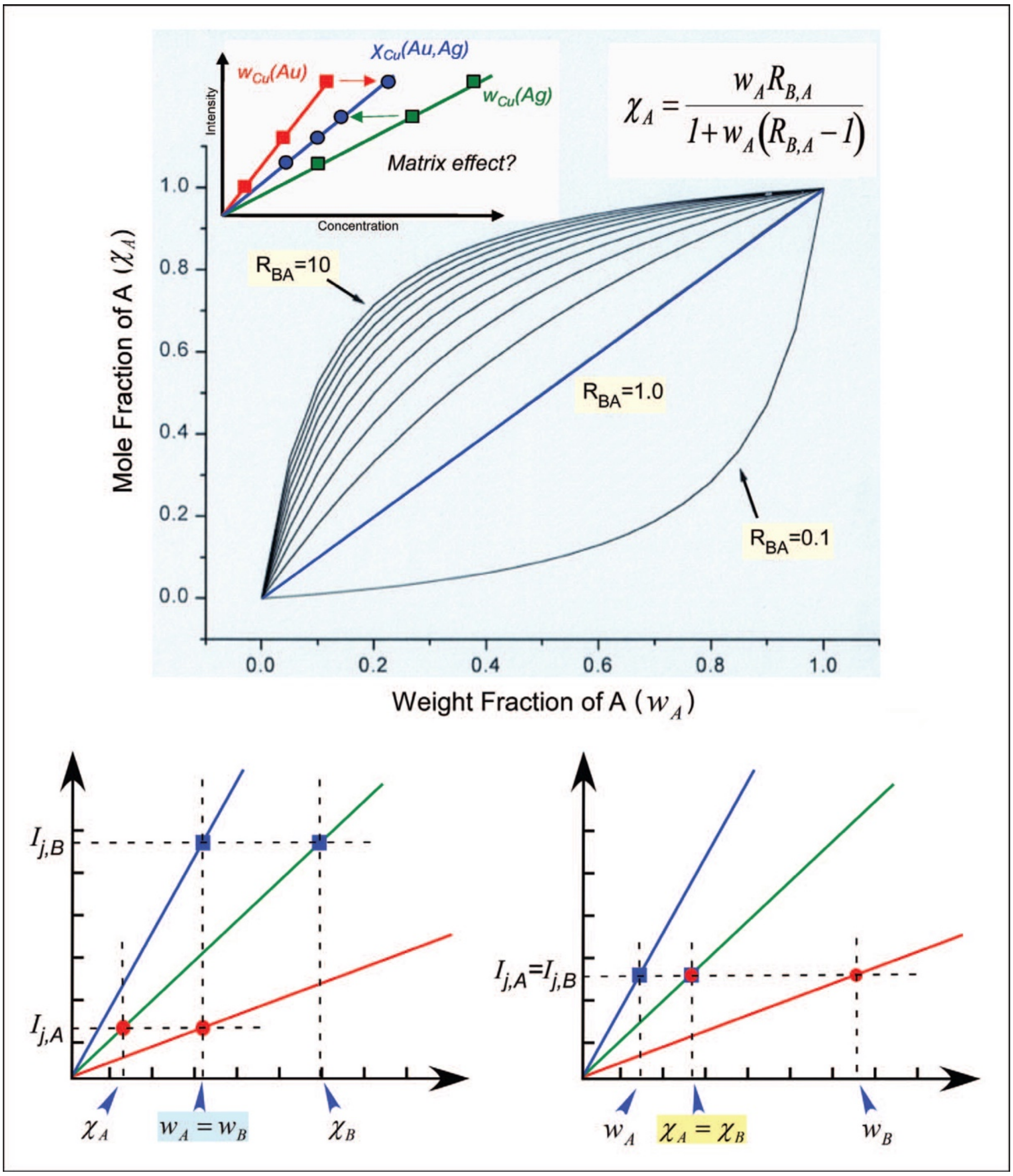

Fig. I-3 Illustration of the different outcomes resulting from choosing the concentration units in weight fraction or mole fraction[94].

I.1.8.2. Normalization approaches

Based on the discussions above, the normalization parameters for LIBS would be the mass ablated, the plasma temperature and electron number density. The general normalization of spectra usually takes the intensity of the spectral line of the analyte in the sample to that of another suitable element present in the sample, or the spectral continuum. There are criteria for selection of spectral lines in LIBS made by Barnett[106]. There are nine criteria in total, five being related to the element choice and four from the choice of internal standard line. They require that the analyte and the ones that used as the internal standard should fit the following conditions. First, they should have similar volatilization rate, second, they should have comparable ionization energies, and last, they should have similar atomic weights. The choice of the spectral lines should be driven by certain rules：They should have first the same excitation energies. They should not have self-absorption and they should have similar intensity. The detailed discussions can be found in the paper[106]. Finally, another paper[107] studied acoustic waves, plasma emission, the electrical current and Mie scattering as the reference signal for LIBS in the normalization approaches. And there are detailed discussions about the considerations of each different reference. Paper[108] which is dedicated to the normalization procedure for certain type of samples, such as the stainless steel samples, can also be found. Besides the plasma temperature and electron number density, one paper[109] also mentioned that the volume of the plasma region can be detected along with some other parameter proportional to the total number of atoms present in the former volume should also be considered. Otherwise, when the only line intensity was used for the comparison, matrix effects can be hidden because of the compensation of plasma parameters.

I.1.8.3. An approach to evaluate matrix effects

Based on the nature of the matrix effects, the reason behind this “problem” can be found maybe through complex theoretical models and repeated accurate experiments. However, this is not the optimal way. In a review[94], the authors introduced a possible way to evaluate matrix effect. For certain selected elements which has the same concentration or in a very narrow range of concentrations, the observed signals of those elements in different matrices can be described as a function of the energy of the excited state from the transitions studied. Two matrices will be used to construct calibration curves for each element separately. From the results they have by then, the existence of matrix effects can be found with the plot of the log of the intensity ratio for the two matrices versus the excitation energy. From this plot, the parameters (ablation mass, temperature) that caused matrix changing can also be found.

I.1.9 Absolute analysis and Calibration Free Laser-Induced Breakdown Spectroscopy (CF-LIBS)

The definition of absolute analysis is very strict, that is only when the theory can describing a single measurement and is reliable to calculate the concentration directly in absolute unit of a physical parameter[110][111], it also means providing quantitative results without any other standard reference materials. Some other chemical analysis methods only use the standard reference infrequently to reach a stage where this method is steady both for time and repetition. It is then called standardless analysis[110], there are chemical analysis methods where absolute analysis were discussed, for instance AAS[112][113], AFS(atomic fluorescence spectroscopy)[114], X-ray analysis[115][116], and laser ionization orthogonal time-of-flight mass spectrometry(TOFMS)[117]. These experiments are close enough to an absolute analysis, however, the difficult of reproduction the same results cannot be neglected. "Progress in this field can result from a better knowledge and more precise description of the theoretical fundamental phenomena responsible for generation of the analytical signal, and from the development of instrumentation with perfectly reproducible and/or theoretically described characteristics.'' quote from IUPAC Technical Report[118]. The pure pursuit of absolute analysis may seem not that practical.

Since the absolute analysis is in some way "beyond reach", attention should be focus on the standardless approaches. In the area of LIBS, Calibration-Free (CF) LIBS can be referred as one of such approaches. It means a procedure which is capable of giving results without calibration standards. Based on the original definition, this approach does not model the plasma, it is not part of LIBS modeling. CF uses the relation between emission intensity and concentration of samples in the plasma. When CF being considered as a model procedure, it would be categorized as a post-breakdown modeling approach. Another thing that worth mentioning is that for CF, matrix is not an interference but being analyzed together with the sample. This method can be considered as quantitative, semi-quantitative or qualitative depending on the analyte being a major, minor or trace components in the relatively error in percentage[119]. To conclude, the importance of just infrequent use of reference standards means that the reproducibility of LIBS has been improved, and the matrix effects being in an acceptable level. The role of CF-LIBS is vital for some cases and that is a guarantee this method will continue in application and improvements. With the development of the modeling, CF-LIBS is excepted to be a much more mature method in the coming years. Further detailed discussions about CF-LIBS can be found in these reviews[120][97].

I.1.10 Signal enhancement

When the advantages of LIBS being mentioned, sensitivity usually is not among them. It is not a surprise that a lot of efforts has been made into improving the sensitivity of LIBS as long with the detection power. The detection powers the reciprocal of the limit of detection[121], by doing so the confusion results could be avoided (a decrease for the LOD value is actually an increase for the performance of the method). An approach is that keep the noise at the same and trying to increasing the analyte signal, since the larger signal-to-noise ratio will have lower detection limits. Many ways can improve the signal level in LIBS, double-pulse and multi-pulse approaches are perhaps two of the most popular ones. Double-pulse LIBS is a solution for the problem that during the ablation and excitation of the plume cannot be controlled separately with single-pulse[122]. From the observation, a large proportion of atoms in the neutral state is present even 40 ls after the plasma formation, a second laser fired at this time could reheat the plasma, thus causing further atom excitation and emission, as proposed by Uebbings[123]. There are increasing number of publications on the double-pulse LIBS in solid samples in recent years, apart from for the liquid samples where this method is originated. Many experimental parameters are involved in this approach, detailed information can be found in a paper by De Giacomo[124]. Like the double-pulse LIBS, multi-pulse LIBS was based on similar consideration: optimize the ablation and excitation independently. A single flash lamp pumped Q-switched Nd: YAG laser was used in order to obtain a sequence of laser emission bursts at a given (low) repetition rate, each burst consisting of several (up to 6) Q-switched short laser pulses emitted during a single flash lamp pulse[125][126]. Applications can be found with steel samples[125][127], alloys[128][129], metallic elements in air[130] and tin sample[129]. Apart from these two approaches, there are other methods for improving the signal, such as magnetic field enhancement, resonant laser ablation, and resonantly enhanced laser ablation.

I.1.11 Comparison of LIBS and other spectroscopic methods

I.1.11.1. Atomic absorption spectroscopy (AAS)

Atomic absorption spectroscopy (AAS) is a spectroscopy used for detection of chemical compositions by absorption of lights of atoms. This technique is based on the fact that when an atom is excited, the electrons will only absorb definite amount of energy (light) to reach higher energy states.

Then in the de-excitation process the electron emits photons with specific wavelength related to the elements, which can thus be delivered and qualified. AAS uses dilute solutions as samples, and the quantification is done though calibration curves. The limit of detection (LOD) of AAS is from 0.003 ppm to 20 ppm, the precision is within 1-2 %, and sensitivity can be enhanced with graphite furnace AAS[131]. AAS can achieve quite high precision but require complex sample preparation, it is not portable, and requires larger quantity of sample.

I.1.11.2. Inductively coupled atomic emission spectroscopy (ICP-AES)

Inductively coupled atomic emission spectroscopy (ICP-AES), or inductively coupled plasma optical emission spectrometry (ICP-OES), is a type of emission spectroscopy for detection of chemical elements. This technique uses inductively coupled plasma to generate excited atoms and ions, which emit electromagnetic radiation which can be used for distinguishing specific element. The concentration can be measured by the use of specific radiation. The samples are analyzed in solution, and multiple elemental detection is available. ICP-AES has negligible self-absorption and auto-reversal effects, the LOD being 10 ppb and accuracy of 1-5%. It is really better than AAS, and can detect some elements that are difficult for AAS. However, this technique like AAS, also requires complex sample preparation and cannot be used in remote analysis or spectroscopic imaging. It needs several minutes to hours for analysis. In addition, the vital drawback of this method is the lack of enough authenticated methods for impurities detection and calculation[132].

I.1.11.3. X-ray fluorescence (XRF)

X-ray florescence is a non-destructive technique that can be used to detect the elemental composition of material. This technique analyzes the secondary (fluorescent) emission of the sample that were triggered by the primary X-ray. When an atom in sample is excited by the primary X-ray, the electrons on the inner shell of the atom are ejected, the electrons on the outer shell would fill in the vacancy on the inner shell. This filling process will release the energy in the form of fluorescence, and the energy is equal to the specific difference in energy between two quantum states of the electron. Each element has unique florescence peaks and the intensities can be used to estimate the concentration, and that is the fundamental basis of the XRF analysis. XRF has been applied in many fields like oil and gas industry[133], metal fabricating[134], art and archaeology[135], and so on. This method requires no sample preparation and provides fast detection, but just for heavy elements. The LOD is in the level of ppm and the accuracy is between 3-23%. The quantitative analysis involves using of calibration curves, and XRF is non-portable and quite expensive.

I.1.11.4. Energy-dispersive X-ray spectroscopy (EDX)

Energy-dispersive X-ray spectroscopy, short for EDX, EDX, EDXS or XEDS, is an analytical technique for elemental analysis or chemical characterization. This method is similar to XRF, when the atom in the sample is focused under an electron beam, the inner electron will be excited and ejected, the electron in the outer shell will fill the hole left. The filling process will release the energy in the form of X-ray, the number and energy of the X-ray will be measured by an energy-dispersive spectrometer. Since the X-rays are characteristic to different element and also to the energy difference between two shells of an atom, this method can be used as a way to analyses the composition of the sample. The difference between XRF and EDX is the source used for excitation, XRF uses X-rays while EDX an electron beam. The LOD of EDX is between 1000 to 3000 ppm[136], the precision is around ±0.1%. EDX does not require complex sample preparation and the experiment itself is not difficult to be carried. Coupled with SEM (Scanning Electron Microscopy), EDX can provide resolved image of sample for spatial information and matrix effects.

EDX requires a high voltage for the electron beam, and when coupled with SEM, EDX-SEM cannot undertake in-situ analysis. And the secondary fluorescence and secondary electron may appear, causing additional spectral lines in the spectrum. Overlap of spectral lines may happen due to the additional rays by secondary emissions.

I.1.11.5. Conclusion of the comparison

Compared with other techniques, LIBS has several advantages:

1. LIBS requires small amount of sample and basically no sample preparations.
2. Multi-element detection is possible, sample can be in gas, liquid and solid form.
3. LIBS is a fast method for analysis, it can be done within a minute. Today, we have a high acquisition, for instance, acquisition of 1000 spectra per second.
4. LIBS in theory can detect all the elements, which is not possible for a technique like AAS.
5. Can be coupled with other techniques, such as MS (Mass Spectroscopy), Raman and etc. for multimethod experiment.
6. LIBS can be used remotely and is portable.

7. Possible for have spectroscopic imaging experiment at the micro-scale spatial resolution.

However, there are also some disadvantages:

1. Compared with AAS, the LOD of which could fall in the range of ppb, LIBS only has LOD of ppm.
2. Self-absorption of LIBS affects the precision of quantitative analysis.
3. The common existence of matrix effects in LIBS reduces the accuracy of quantitative analysis.

As stated above, LIBS is a simple, fast, free of sample preparations, portable method for analysis of chemical composition of specimen, it has some merits and also a few drawbacks. Combined together, as an important analytical method, LIBS has a wide application in material analysis in many areas.

I.1.11.6. Algorithms for chemometric explanation of LIBS spectra

As mentioned before, accuracy of quantitative analysis is not the advantage of LIBS, however, with the help of chemometrics, the situation could change. Chemometrics is using mathematics, statistic and computer science to better understand the chemical information, the use of which in the area of LIBS can be categorized into 2 major branches, qualitative (also classification and clustering) and quantitative (calibration) analysis. The application of chemometrics can help to improve the stability and reliability of LIBS online analysis[137].

I.1.12 Qualitative analysis

The chemometrics methods used here are mainly two types: supervised and unsupervised approaches.

I.1.12.1. Supervised classification methods

By definition, supervised classification requires training a model with known dataset, and then use the model to predict the unknown sample. Common supervised methods include Partial Least Squares Discriminate Analysis(PLS-DA)[138][139][140], Soft Independent Modeling of Class Analog (SIMCA)[141][142][143], K-nearest neighbor (KNN)[144][145], Supporter Vector Machine (SVM)[146][147], Artificial Neural Networks (ANN)[148], Random Forest (RF)[149]and etc., and they will be discussed in the next parts.

I.1.12.1.1. Partial least squares discriminant analysis (PLS-DA)

PLS-DA is a widely applied method in chemometrics based on partial least squares regression (PLS). It uses a matrix X with independent variables and a matrix Y for the categorical variables to construct the model for training. Then the unknown sample is being introduced, the model will give the class of the unknown sample by the predicted PLS values.

In the food quality control area, PLS-DA[139] was used to build a classification model for distinguish the real honey from honey added with sugar cane syrup, along with other chemometrics methods like variables selection and some data preprocessing methods, the author showed their model performed 100% accuracy in adulterant detection for honey. Combined with PLS, LIBS showed the possibility of a fast, simple, sample preparation free authenticity certification of honey samples.

Another example[138] is the application of PLS-DA in LIBS for detection of the usage of pesticide in spinach and rice. Though similar elements exist in both pesticide contaminated sample and pesticide free sample, the relation between the LIBS intensity and concentrations of each element can be established. With the confirmation of inductively coupled plasma optical emission spectroscopy (ICP-OES), LIBS combined with PLS-DA can be a rapid way to detect pesticide achieving a misclassification rate lower than 2% for spinach samples.

In the field of recycling plastic bottles, LIBS was used combined with SW-PLS-DA (partial least squares discrimination analysis based on spectral windows) to build classification able to classify 20 different types plastic bottles commonly used in supermarket chain in China[140]. In their work, a basic PLS-DA model was also built for classification with the highest accuracy of 67.50%. In order to improve the results, methods for selecting input variables were applied, including CWT (continuous wavelet transform) and SW (spectral windows) based on CWT, different parameters of CWT were tuned and the best results showed an accuracy of 93.93%. There were other chemometric methods has been applied for comparisons, including a basic PLS-DA, supporter vector machine (SVM) and random forest (RF). SW-PLS-DA showed the best result and also showed the potential of online analysis for plastic recycling.

I.1.12.1.2. Soft independent modeling of class analog (SIMCA)

Soft independent modeling of class analogy (SIMCA) is a pattern recognition method based on PCA. A PCA is calculated on each class of the training set separately. Then statically criteria are used to define the volume containing all the samples of a class. Next, these criteria are used in order to classify unknown samples.

The classification result is better when the differences are larger between the classes than the differences within a class itself. As a consequence, when the differences are not significant enough among different classes, the model built is not optimized good enough to have good results. In an example[142] of using LIBS/SIMCA to classify grains from Wahiba Sand Sea, Oman, the methodology of combining LIBS with SIMCA showed good results of classification carbonated sand grains from different areas in the sand sea, and showed the potential sources of the sand grains to better understand the formation of the dune. This example showed the promise of applying this method in complex mixing patterns in sample. In the area of recycling polymer, LIBS was applied to 6 types of polymers, acrylonitrile-butadiene-styrene(ABS), polystyrene (PS), polyethylene(PE), polycarbonate(PC), polypropylene(PP), and polyamide(PA)[143]. Emission lines were selected for some elements and used for classification. SIMCA and (k-nearest neighbors) KNN were utilized to build classification models, and satisfactory results were achieved with 98% accuracy for KNN and 92% for SIMCA. It showed promising analytical capabilities of LIBS with chemometrics methods in identification and classification of plastics.

I.1.12.1.3. Artificial neural network (ANN)

Artificial neural network (ANN) is a modulization tool containing groups of nodes that was inspired by the biological neurons in animal brains. It is a typical non-linear method, the basic unit called neuron imitates the function of its own original type, a biological neuron, transmitting the signal to the next ones. Briefly, an artificial neuron receives signals and processes them, the output of the neurons is computed by specific non-linear algorithms. The detailed discussion will be in the later part. Since ANN can learn from known pairs of inputs and outputs to predict unknow input after training. It has lots of applications in many different areas, such as image recognition[150], voice conversion[151], machine translation[152], medical diagnosis[153], finance fraud[154], and etc.

In LIBS, ANN was applied to the classification of wood samples[21]. In this case, loadings of PCA were used to compress data, after the normalization. Two different methods were applied in ANN, multilayer perceptron network and Broyden–Fletcher–Goldfarb–Shanno iterative algorithm, and achieved 100% for the correct classification rate (CCR). This work has also been compared with PLS-DA, KNN and SIMCA, with the CCRs of 82.5%, 95.83% and 51.67%, respectively. The results demonstrated that the combination of ANN and LIBS could be used for analyzing and cataloged different wood samples.

In an example[148] of apply ANN in LIBS, both LDA and ANN were applied in fast identification of archeological materials in situ. 18 samples in 7 types (include shell, bricks, soil pellets, ceramic, teeth, bones and mortars.) were used to train the ANN, input of the network in this case are the PCA scores of the data, in the consideration of reduce the size of the data. ANN showed a better result than LDA, only one out of eight samples are not correct for ANN, and for LDA 2 samples were not correct.

In the area of chemistry, one[155] of the early attempts of applying ANN into LIBS data utilize eight spectral regions of interest of polymers as the input into a feedforward network for classification. The network was modularized into two sub-networks, one to distinguish PVC (polyvinyl chloride) with one neuron as output layer and three neurons for the hidden layer, the other one has three neurons as output and eight neurons for the hidden layer for PE (polyethylene), PP (polypropylene) and PET (polyethylene terephthalate). The results should be considered as very good when the accuracy is all above 93%. Another application[156] of ANN in LIBS applied the similar network into the spectra of eight polymers, 13 spectral lines were used as the inputs after normalization. In this article, a three-layer network was built, the number of neurons of each layer has been modified to give the best results. The application of this ANN has successfully overcome the influence of the matrix effects from the samples, and achieved a satisfactory accurate classification.

In archaeological area, LIBS was combined with ANN to classify archaeological ceramics samples[157]. Two strategies were used, one using the whole spectra of LIBS, and another one using spectral sub-domains. In both the methods, ANN showed more than 95% of correct classification rate.

LIBS's ability to identify material is useful in the area of extraterrestrial exploration, such as the study of Mars. And in one similar example[158] of classification of different metal alloys, LIBS was coupled with ANN to identify different types of aluminum alloys. ANN gained 96% correct classification rate with 19 references set if only the classified mineral were considered, and 78% success rate when unidentified samples were included. And real-time rough material identification were also carried out among materials like metal alloys, marble, granite, soil, clay, rock, sediments and silicon oxide[158]. The results within the set of aluminum alloys showed that this method has high sensitivity. This article[158] demonstrated the possibility of LIBS with ANN for analysis of material on the surface of Mars.

I.1.12.1.4. Support vector machine (SVM)

Support vector machine is an original binary supervised learning model, it has a learning algorithm based on kernel function, and it is suitable for small dataset. In SVM, a data is regarded as a p-dimensional vector (as the same number of the list), and the algorithm will try to find a hyperplane with a dimension of (p-1) to separate them. And it is called a linear classifier, according to the theory, the hyperplane is more than one, and the one with largest separation between the two classes is the most reasonable choice. If the hyperplane being chosen is the one that the distances from one data point to the nearest one on each side of the plane is maximized, then it is called a maximum-margin hyperplane. As mentioned above, SVM is original binary method, however, by reducing the single multiclass problem into multiple binary problems, multiclass SVM also exists within finite groups.

In pharmaceutical area, LSSVM(least squares support vector machine), PLS-DA and SIMCA were applied for discrimination in LIBS measurements[146], and the results showed that LSSVM (96% in average accuracy) improved the sensitivity in classification compared with PLS-DA (95.67%) and SIMCA (94.03%), and for the robustness test, LSSVM also showed a good result with 92.47% in accuracy compared with SIMCA of 83.53% and PLS-DA of 83.95%. This example showed that combined with SVM, LIBS can provide a sensitive and robust results in classification of pharmaceutical samples.

In an example[147] of soil analysis using LIBS, PCA was first applied to select 7 emission lines and then SIMCA and LSSVM were both used to classify 6 types of soils. The correct discrimination rates were 90% for SIMCA and 100% for LSSVM. The LSSVM model was further applied to discriminate 8 types of soils for verification. This research indicated that coupled with LSSVM, LIBS could conduct classification for soil samples.

I.1.12.1.5. K-nearest neighbor (KNN)

K-nearest neighbor is a multiclass method for samples that are difficult to classify in linear method. KNN calculates the nearest distance of a given sample to K number of known samples, and the given unknown sample will be categorized according to the distances of different known classes. In an example[145] of leather quality evaluation, KNN, SIMCA and PLS-DA were applied into analysis of LIBS data from both sheep and cattle leather samples. The results showed that models achieved satisfactory classification rate for SIMCA: 75.2%, PLS-DA: 80.5% for calibration data, and for validation data, the classification for KNN: 80.9% and for SIMCA: 71.6%. These results confirmed that LIBS combined with chemometrics can be used in quality classification in leather.

In the medical area, KNN was also used to distinguish fresh soft tissues based on LIBS spectra[159]. Chemometrics methods were applied to discriminate fat, skin and muscle tissues, and also among highly similar tissues like ham, loin and tenderloin muscle. The methods included PCA, KNN and SVM. For fat, skin and muscle tissues, KNN and SVM were applied and achieved accuracy more than 99.83% with sensitivity over 99.5% and specificity over 99.8%. For the discrimination of 3 highly similar tissues, SVM gave the best results with an accuracy of 76.84%, a sensitivity over 0.742

and a specificity over 0.869, which is an acceptable performance considering the molecular complexity of such sample. The results showed that assisted with chemometrics LIBS could be a powerful tool for discrimination of soft tissues, even for highly similar samples.

I.1.12.2. Unsupervised methods

I.1.12.2.1. Principal component analysis (PCA)

Unsupervised pattern recognition is based on the distances between samples, similar samples would have shorter distances in multidimensional space and for unknown samples the distances would be longer. One of such common method is PCA. In an example[160] of classification of four types of plastics with LIBS, PCA was applied with success. The results were further confirmed with statistical parameters, Mahalanobis distance and spectral residuals. Another example[161] of discrimination by PCA was done with oyster samples. PCA was applied with factor analysis together with the elemental composition from LIBS, and managed to classify samples from different sites with a result of 91.3% unselected cases correctly discriminated.

I.1.13 Quantitative analysis

The quantitative analysis in LIBS is managed in two ways, calibration methods and calibration free methods[39]. Within the calibration methods, it can be further categorized into univariate and multivariate approaches. The conventional quantitative analysis in spectroscopy usually establishes the relationship between concentration of either an element or a component and the intensity of the spectra line. This univariate method is accurate and widely used in particular spectroscopies, however with LIBS, it often failed to obtain the better results. The complexity of LIBS data makes the traditional regression method no longer available in some cases, so it is interesting to take advantage of the abundant information that LIBS data can provide with the use of multivariate methods.

I.1.13.1. Calibration curve method

I.1.13.1.1. Univariate calibration

The univariate calibration is one of the most widespread and simplest quantitative analysis methods. It establishes the relationship between the intensity of an emission line of an element in the sample and its concentration. In the area of LIBS, the group of Andrade[162] used this method to determine the concentration of 12 elements in solid fertilizers. Correlation between the predicted values and the reference ones was right. Other examples can also be found in literature, for instance, 11 elements in fingernails were determined by LIBS with the help of calibration curves[163]. LIBS was used in inline analysis of liquid slag in steel works, and the major components were in the good agreement of the reference samples from the laboratory[164]. Univariate method has the advantage of being simple and has good agreement in many cases, however, it may not be able to meet the requirements for heterogeneous samples due to the fluctuation of the laser energy. A common method here is to use an internal standard added for the samples. In a quantitative study[165] of rare-earth elements(La and Nd) in phosphors by LIBS, a standardization method was applied. Another case[166] used argon environment to reduce the influence of the air at atmospheric pressure for quantitative analysis of oxides in minerals. The results showed a real improvement of the signal quality and better linearity of the calibration curves. The addition of the internal standard also improves the accuracy of the univariate calibration. Still this method is not universal and cannot meet the standard of the high-accuracy analysis.

I.1.13.1.2. Multivariate calibration

Commonly used multivariate calibration methods in the quantitative analysis in LIBS are PLS regression[167][168][169][170][171], multiple linear regression (MLR)[172] [81][174], ANN[148][175], SVM regression[176][177] and RF[178].

Partial least squares (PLS)

PLS is perhaps one of the most commonly used multivariate statistical analysis methods in many areas of analytical chemistry. The number of latent variables is an important parameter in this method PLS is particularly suitable for tasks where the number of independent variables is bigger than the number of samples. In PLS, considering the samples as a matrix X, the orthogonal decomposition of the X and the response matrix Y will be used to build a regression model based on feature variables. Because of the mathematical theory of PLS, it is an accurate and fast method. In an analysis[167] of wheat ash samples via LIBS, PLS was built and showed good results. The ash contents were between 0.48% and 1.39% with a R^2 of 0.992. In another use[168] of PLS in LIBS is a case with detection of adulterated milk powder. The calibration curves from PLS showed that the R^2 and LOD for sweet whey powder, one of the adulterations in this case, was 0.981 and 1.55%, respectively. The R^2 and LOD value for acid whey powder, another material used for adulteration, is 0.985 and 0.55%, respectively. There are also some other PLS based methods, such as GA-PLS in the quantitative analysis of soil samples in LIBS[169], a hybrid model that combined PLS with spectrum standardization in coal analysis[170], a combination of WT(wavelet transform) and PLS in the analysis of Carbon in coal[171].

Multiple linear regression (MLR)

MLR is a regression model for quantitative analysis, using simultaneously several selected wavelengths in the spectral. MLR and simple linear regression were both applied to soil samples for determination of C[173]. The results showed that MLR has better result than simple linear regression. In another example[174] of Pb determine in navel oranges, MLR was built and the feasibility of the MLR model was verified with variance analysis and regression statistics. The results showed that MLR had better results. In this article, authors said that MLR method used here can take full information from the LIBS data for quantitative analysis and reduce the influence of the matrix effect.

Artificial neural network(ANN)

In the previous part, we showed that ANN is capable of solving classification problems in LIBS. In this part, examples showed that ANN is also be able to solve the prediction problems in LIBS due to its self-learning ability. In another example, ANN was used to improve the accuracy and precision of Cr and Ni concentration prediction in steels[175]. ANN showed better results than the conventional internal calibration method, RMSE of CV for Cr and Ni decreased to 0.010 and 0.023 wt% from 0.018 and 0.067 wt%, respectively. Besides, the relative standard deviation for these two elements also decreased from 11.3% to 6.4% for Cr and from 19.5% to 12.9% for Ni. An on-site analysis[179] of soil samples illustrated that combined with ANN, LIBS can be used for quantitative analysis. The ANN showed results of less than 20% of errors for target elements (such as Al, Ca, Cu and Fe), and which means a good efficiency for on-site soil analysis with LIBS.

Support vector machine regression

SVM is one of the machine learning methods based on statistical learning theory. Besides it's would not for classification, SVM can also be used for regression purposes. SVM regression model is based on structural risk minimization, and is capable of manage the balance between complexity and the learning ability according to the sample information. SVM regression is suitable for small size datasets. Combined with advanced kernel functions and prior knowledge, it has many applications in many areas. In an experiment[180] of quantitative analysis of Ni in water, 3 different regression methods(MLR, ANN and SVM) were applied, and for this case, SVM performed best. There are also other methods such as LSSVM and relevance vector machine (RVM) applied in LIBS. In another analysis[176] of major components in slag samples, LSSVM was used to build the model with full spectra as the input. This model decreased the effect of nonlinear factors from self-absorption in plasma and can provide an ideal result. RVM regression method is a sparse probabilistic model for limited samples, it has good fitting and generalization ability, and also can provide the probability distribution of the prediction result, and this method is capable of dealing with noisy samples. In the area of LIBS, a RVM model[177] was built for Cr in steels samples with the analytical lines who was selected based on the spectrum intensity, wavelength, the widths of half-height. The results showed that in this example, SVM has better performance than SVM, ANN, PLSR.

Random forest (RF)

RF is a regression method based on a decision tree. It contains more than on decision trees generated by bagging integrated learning technology. The final results will be the averaged vote from multiple decision trees. This method can solve the problem of overfitting and has a good balance of noise and outliers. In an analysis[181] of 5 elements in steel samples, PLS, SVM and random forest were adopted simultaneously, and RF had the best results than the other two. The existence of S and P in steel samples may have some matrix effect that are difficult to manage quantitative analysis. In a case[178] of LIBS, quantitative analysis of S and P in steel samples, RF showed good prediction compared with PLSR, which showed that this method had a promising potential in the area of steel quality control.

I.1.13.2. Calibration free method

Contrary to the methods based on calibration curves, methods without calibration are called calibration-free method, short as CF. CF-LIBS[39] appeared for quantifying elements within unknown samples. This method using plasma emission lines with mathematical models to determine the content of elements of interest from the single spectrum to be considered. It does not require calibration curves or reference samples. Therefore, CF-LIBS can solve the matrix effects that is caused by the different matrices between the unknown sample and the reference sample. Even if the CF method has some improvement mentioned above, it still cannot compensate the variation caused by plasma temperature nor the influence from self-absorption. The importance of plasma temperature has been addressed enough from [], and many different methods has been invented for different cases. A modified version of CF method[182] was invented to analyze copper-based alloy samples in archeology, the plasma temperature was determined by a mathematical method related to known samples, and results were compared with the classical LIBS method. There are also CF-LIBS that combines with different methods, such as CF/ANN[183], CF-LIBS combined with a binary search algorithm[184], CF-LIBS combined with GA to determine the plasma temperature[185] and etc..

I.1.14 Conclusion and prospects

The short summary of chemometric methods in LIBS showed the great potential in the data pretreatment and qualitative and quantitative analysis. It proved to be an effective tool for LIBS and improve the accuracy of quantitative analysis in many different areas. LIBS technology has promising application in complex material analysis, combined with chemometrics. The future of this technology without any doubts would further extent its area with better performance. The improvement of instrument brings bigger and bigger datasets, which is exactly the stage for chemometrics. Some theoretical issues of LIBS, like matrix effects and self-absorption has been solved for certain cases, yet still a general solution is on the way, but chemometrics showed a very promising way towards it. This is what we will show in this thesis.

I.2. A special focus on Artificial Neural Network (ANN)

I.2.1 Introduction

Artificial neural network (ANN) was born with the concept of building a network which imitates the behavior of neurons in animal brains to solve problems. Artificial neural networks can learn from dataset to classify, to predict, in a way almost like how a human brain works, learning from experience of means. A typical simple network has an input layer, a hidden layer and an output layer, as shown in Fig. I-4.

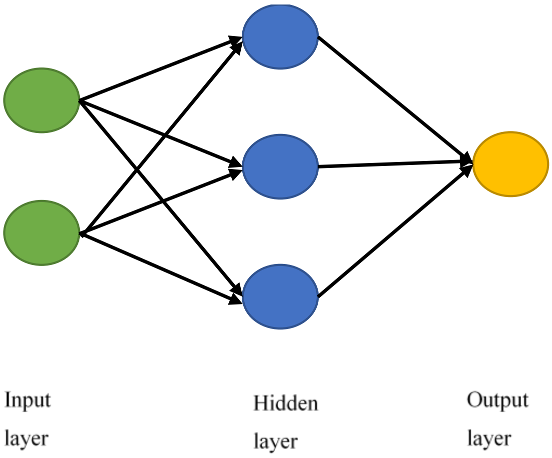

Fig. I-4 The structure of ANN

I.2.2 History

One[186] of the earliest attempts of building ANN was in 1943. Then several years later, D.O.Hebb created a hypothesis, later known as Hebbian learning, based on the plasticity of neurons. Hebbian learning is considered as a classical unsupervised learning. The following years, a lot of different networks have been created and improved. But not until 1975, Werbos's backpropagation[187] algorithm came out, leading to artificial neural network to achieve a crucial development. Due to the limit of computer back then, the development of ANN was slow. In the meantime, support vector machine and other linear classifiers were much more popular until around 2000, the emerge of deep learning brought ANN back into the game again with even more complex ANN structure.

I.2.3 Basic theory

ANN is built with sets of artificial neurons, also called nodes, to simulate the function of biological neurons in animal brains. The illustration of an artificial neuron is in Fig. I-5 x1 to xn are the input signals; w1 to wn are weights of the neurons; b stands for bias; y is output; the transfer function usually is non-linear. These neurons, like their prototype, can transmit signal to others after processing. Normally, these signals are real numbers, connected with weights which form the structure of the network and aggregated into layers. Each neuron has its own set of weights, transfer function and output, sometime also a bias. Based on the chosen learning rule, the weights will be adjusted during the learning process, the sum of which will be the activation of the neuron. Then the activation will go through the transfer function to generate one single output. This output will be an input of next neuron, until the output of the neural network. The non-linearity behavior will be introduced into the system through transfer function. The sigmoid function is the most used transfer function. The network will stop training when the output meets the chosen criterion, for example, a certain level of accuracy or error. At this point, the network is well-trained and can be feed new dataset for test.

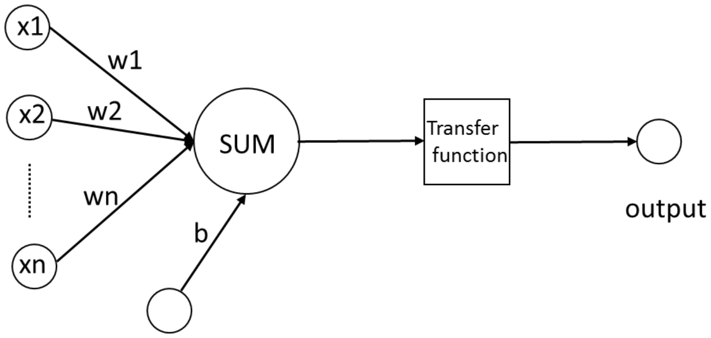

Fig. I-5 The scheme of neuron

I.2.3.1. Constitution and basic structure

A typical artificial neural network has three parts to be optimized, architecture, activation rule and learning rule. Architecture sets the topology of variables within; the variables are weights who connect the neurons or the activities of neurons. The majority of networks have a way for neurons to change themselves based on the effects from other neurons, this is usually considered as a short-time dynamic rule. Learning rule is a long-time dynamic rule about how the weights being adjusted.

I.2.3.2. Training

The learning of an ANN is an important part, during the process, the network compares the differences between output of the network and the known target, then adjust the parameters (weights of neurons, biases, parameters related to the chosen algorithm, etc.) according to the chosen learning rule to make the output more and more close to target. These adjustments are also known as tuning of parameters. After tuning, the output should be as “real” as the target. Then the already trained network will be tested for accuracy, on with new data not used during the training.

One of such examples is image recognition. Loads of manually labeled pictures of “cat” or “not cat” were used as input, then the network will analyze them and generate characteristics from which. Later, the well-learned network will be used to classify new pictures whether they are cats or not. This type of ANN is considered as supervised learning.

I.2.3.3. Types of ANN

One[186] of the earliest attempts talked about the theories about building the network with and without circles in the structure. Nowadays, there has been a lot of different networks built many ways. Among them all, they can be categorized into two basic types based on architecture, feedback (recurrent) (Fig. I-6) and feedforward (Fig. I-4).

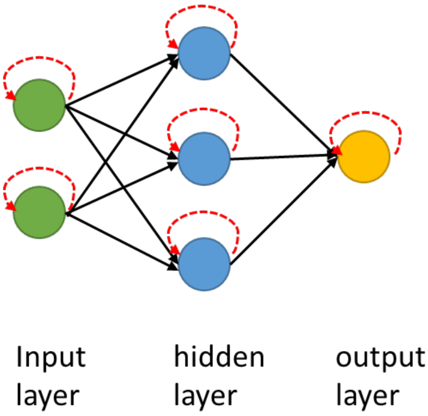

Fig. I-6 Feedback network

I.2.3.4. Theoretical features, criticism

The non-linearity behavior is the biggest feature of ANN, and perhaps also the biggest flaw. Since the exact theory about how a network gain the result through learning is not yet available, artificial neural network sometimes is described as a black box. You know the input, you know the output, but you don’t know how the output came out from the input. In the training of ANN, the previous knowledge about the dataset is not necessary, answers have been found themselves as if by magic, almost. However, ANN requires a lot of training, and the size of the dataset could be huge, which would result in enormous computing resources.

Back-propagation (BP) neural network(Fig. I-7)[188] is perhaps the most known and used. Besides, Self-organizing feature mapping (SOM) network [189], the Hopfield neural network[190] , the radial basis function (RBF) neural network[191] and the recurrent neural network[192] are the other commonly used networks.

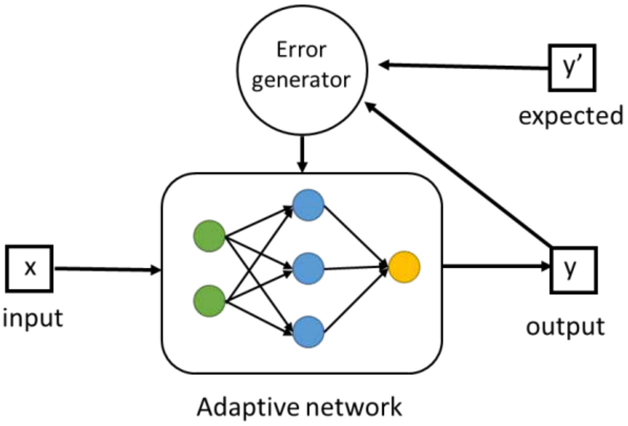

Fig. I-7 The scheme of backpropagation

I.2.3.5. Theory of back-propagation (BP)

The popularity of ANN rises with its application in voice recognition and visual recognition, where the traditional logical linear methods failed. These applications in ANN introduced a new area later known as deep learning. Its immense capability of dealing with complex models, ANN was applied in many areas in recent years and achieved some promising results. As for chemistry, there are more and more applications these days, but due to the difficulty of having right size of dataset, the lack of straight mechanism, ANN still cannot be considered as a main approach.

I.2.4 ANN in LIBS

The abundant applications of ANN in LIBS has been discussed previously in the previous sections (1.11.1.3 and 1.12.1.2), for both qualitative and quantitative analysis. Many ANNs in LIBS aimed in quantity, or classification, sorting. The other large part of the application of chemometrics in LIBS is calibration, as stated in one review, the calibration in LIBS is an empirical process, the existence of universally good solutions are precluded[94]. As mentioned above, lack of enough data is one of the problems for ANN, luckily, we still have simulated data. Then came the idea that why not using the simulated datasets to train ANN, then apply the real data as the test set for the neural network. When the simulation of training dataset is close enough to real data, the problem of lack of data no longer exists. In the following chapters, this idea has been used. Simulated datasets were generated for training ANN in the next chapter, the details of generation and of the ANNs were discussed in details, also the evaluation of results. In chapter 2, the real data was applied as test set to the neural networks that have been trained with simulated data, the results and the problem will also be discussed.

Chapter II

Robust quantitative analysis of complex samples using LIBS imaging and ANN independent of plasma temperature and electron density

II. ROBUST QUANTITATIVE ANALYSIS OF COMPLEX SAMPLES USING LIBS IMAGING ANF ANN INDEPENDENT OF PLASMA TEMPERATURE AND ELECTRON DENSITY

II.1. Development of an ANN with simulated datasets

II.1.1 Introduction

In the previous chapter, we were able to observe the full potential of LIBS spectroscopy for the characterization of complex materials. We have also seen the different chemometric approaches that allow us today to propose a valorization of the acquired spectral data at both qualitative and quantitative levels. From a fundamental point of view, we explained the importance of the main characteristics of the plasma, such as its temperature and electron density, as they have a significant impact on the intensities of the emission lines and even on the presence of some of them over a wide range of wavelengths. Of course, theoretical models could allow us, in some way and under very strict conditions, to correct the emission line intensities but this would remain a complex and very time-consuming task. In fact, we could only consider this strategy for a few spectra but not for hundreds of thousands or even millions of spectra of a LIBS hyperspectral imaging dataset available today. This is the problem we have been working on in this chapter. In LIBS imaging, we first acquire spectra systematically over a region of the sample. In a second step, we integrate the emission signal at a wavelength characteristic of the compound of interest in order to generate a spatial distribution map of the latter. This is a basic principle used for many spectroscopic imaging techniques well beyond LIBS spectroscopy. This integration methodology makes sense in LIBS because we often have the possibility to find an isolated emission line, i.e. without interference. Nevertheless, spectroscopic imaging is primarily implemented when one wants to investigate a heterogeneous sample with many variations in matrices and chemical structures, and it is naturally in these conditions that variations in plasma temperature and electron density can vary. These potential variations in plasma parameters between the different spectra of the imaging dataset thus influence the intensity of the selected emission line and ultimately lead to under- or over-estimations of the element concentration and thus a biased chemical image. Researchers using this LIBS imaging technique are for the most part well aware of the problem but are ultimately at a loss.

The aim of this chapter is therefore to develop a predictive model of the quantity of an element in a spectrum independently of the plasma temperature and electron density. In the classical development of such a quantitative model, the calibration or training step requires the availability of experimental data and more precisely a large number of "spectrum/quantity of the element obtained by a reference analytical method" pairs. It is obvious that this is not feasible in LIBS imaging because firstly it is impossible to estimate the concentration of an element by an analytical method on each pixel but secondly, we cannot have the plasma parameters for each of them. The originality of the work in this chapter is therefore to generate synthetic LIBS spectra with varying concentrations of the elements of interest but also including variations in plasma temperatures and electron density. Due to the complexity of the phenomena to be modelled and the potential non-linearities between the inputs and outputs of the model, we have focused on artificial neural networks. The following sections will introduce the spectroscopic data generation, the construction of the ANN models and their optimization. For your information, this chapter accounts for 90% of my research time during the thesis with more than 200 neural networks built.

II.1.2 Generation of a big LIBS synthetic dataset

The originality of our strategy lies in the generation of synthetic spectral data allowing us to control the temperature and electron density variations of the plasma. It is true that this is a risky bet because it is very rare in chemometrics, but the near impossibility of really evaluating these two parameters on real spectra forced us to proceed in this way. We thus started from the Kurucz database [193] which is well known to the LIBS community. It proposes effectively for each element of the periodic table all the emission lines and the associated Einstein coefficients. Based on the equations of Boltzmann and Saha, we were able to simulate the LIBS spectrum of an element for a given temperature and electron density. In order to get closer to the reality of the LIBS spectral data, we also applied to each of the emission lines a Lorentzian profile with a bandwidth of 0.15 nm [194]. It should be noted that the Stark effect and self-absorption have been neglected in this work, which is above all a first feasibility study and a proof of concept. Table II-1 shows all the elements used in this study as well as the different temperatures and electron densities. At first it might be surprising to see that only 22 elements have been selected in the periodic table but also why these elements in particular. Our goal was first of all to limit our calculation time and the consideration of all the elements of the periodic classification would have undoubtedly made the construction and optimization phases of our predictive models more difficult. However, we have to put this into perspective as it is not trivial to propose a quantification on 22 elements.

Table II-1 Elements, temperature and electron density used in the spectral data generation

Elements	Temperature (K)	Electron density number (cm^{-3})
Ag, Al, As, Au, Ca, Cr, Cu, Fe, Ga, La, Mg, Mn, Mo, Na, Ni, Pb, Si, Sr, Ti, U, Zn, Zr.	6000,7000, 8000, 9000, 10 000, 11 000,12000.	5×10^{16}, 1×10^{17}, 5×10^{17}

We must not forget either that all the elements of the periodic table will not be detected in a complex sample because of certain elemental concentrations that are too low but also because of their detection limits in LIBS. For these 22 items in particular, they were chosen because they are potentially contained in a real sample that we will explore later in this chapter, once our models are trained for these quantitative predictions. As we can also see in Fig. II-1, we have considered in our study 8 levels of temperature and 3 levels of electron density in accordance with experimental conditions likely to be encountered in classical LIBS experiments. For a given plasma temperature and a given electron density, a simulated LIBS spectrum of an element will be referred as a pure spectrum in this work. Fig. II-1 shows the simulated pure spectra of element Ca at varying temperatures and plasma densities.

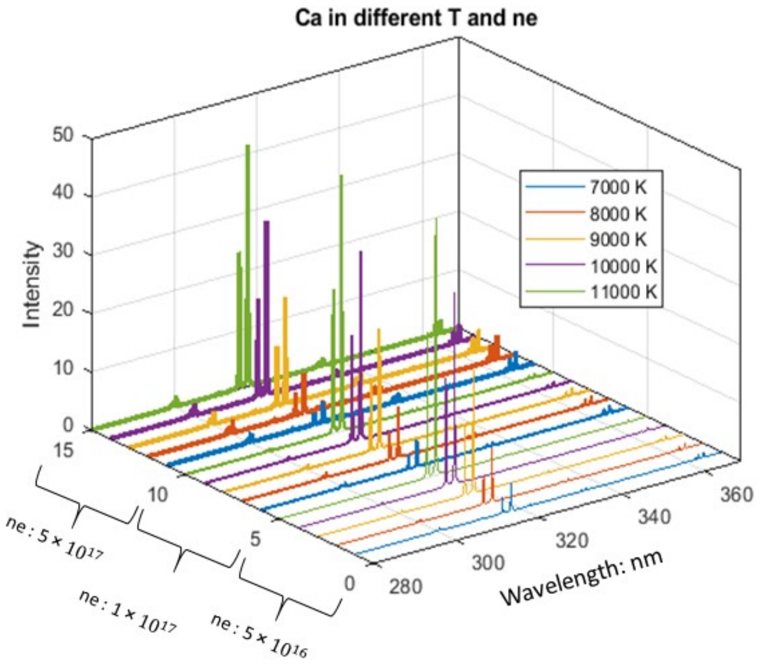

Fig. II-1 Influence of the temperature and electron density on the pure elemental spectrum Ca

We see here, by this simple case, that the intensities of the lines are particularly impacted by the variations of these two parameters describing the plasma. This gives us a real understanding of the problem, as the intensity of the lines is usually used to obtain a quantification of an element. So if we do not take into account the plasma parameters we could, for example the decrease in intensity of a line between two spectra linked to different plasmas were observed, but in the incapacity to detect this situation we could interpret it as a decrease in the concentration of this element whereas it could be unchanged. It is obvious that such a situation would lead to the generation of LIBS chemical maps with estimated under- or over-concentrations if we use the usual strategies to generate them. Since real spectra are of course not made up of a single element, we simulated mixture spectra using a linear combination of the pure spectra of the elements with randomly selected concentration ratios for each of them. An in-house Matlab code then allowed us to generate several hundred thousand mixture spectra by varying, if necessary, the plasma temperature, the electron density or even both with the constraint of having the sum of the elementary concentrations equal to 1. We have also taken care to ensure that each element can be considered as a major, minor or even trace element in all generated combinations. Moreover, we also had the possibility to add a more or less important noise on these mixture spectra but also why not to use only some elements from the 22 mentioned above. This strategy gave us the freedom to choose different levels of complexity to better understand our problem. To summarize the procedure of generation of a spectrum, a plasma temperature and an electron density were randomly drawn from the values previously mentioned. With these two parameters being fixed, we considered the pure spectra of the elements associated with these conditions. Then a random set of concentrations of the considered elements were generated, which linked to the previous pure spectra by linear combination. At this point, we obtained a synthetic mixture spectrum to which we could finally add an experimental noise or any other perturbation. This strategy allowed us to generate training and test sets naturally composed of “spectra” / “concentrations” pairs.

II.1.3 General consideration about the development of our artificial neural networks

From the numerous examples in the literature from different scientific domains, it is obvious that neural networks have a strong potential for modeling potentially non-linear phenomena, even without any prior knowledge of the relationship that could link the inputs to the outputs of such a model. Thus, in our case these inputs would correspond to LIBS spectral data and the outputs to the concentrations of the elements of interest. Unfortunately, this methodology is by no means push-button and the predictive potential of a neural network can only be realized after a long optimization phase, which is even longer as the link between inputs and outputs is complex, which is our case in this work. The first thing to optimize in a network is its structure. It is often by default composed of an input layer of neurons (which accepts LIBS data), a layer of hidden neurons and a layer of output neurons which will predict our concentrations. We can then ask ourselves questions about each of the layers. To begin with, we will have to see if we can use as many input neurons as wavelengths in the spectrum or if we will have to transform our spectral data to limit the input data and thus the number of neurons. We will also have to think about the possibility of using raw data or rather applying pre-processing methods to ease the predictions. We will also have to study the influence of the number of neurons in the hidden layer and also the number of layers themselves. Indeed, too few neurons on the hidden layer would not fulfill the prediction objective, while too many would most likely lead to over-fitting problems[195]. The balance between the prediction performance of a network and the complexity of its structure is at the stage where the network is just large enough to provide sufficient accuracy and reasonable time in the learning phase. In this work, hidden neurons varied from one to 200. Regarding the number of hidden neuron layers, it is obvious that a single layer should be preferred to limit the total number of parameters to be optimized on the whole network. Nevertheless, we consider sometimes networks with several hidden layers in the framework of complex modelling. It will thus be necessary to remain pragmatic and look at this possibility in our case. As far as the output neuron layer is concerned, we will also have to ask ourselves the right questions. Ideally, it is true that training a single network to simultaneously predict all 22 concentrations and why not the temperature and the electron density would be the ideal situation. We would then have a network with 24 output neurons. This option would undoubtedly be the fastest to develop and then apply to real data. However, it is not clear that such a model is possible and we may have to build several separate networks capable of predicting a limited number of elements, or even just one if the overall network is not predictive enough. In addition to the influence of the neural network structure that we have just seen, we will also have to consider the optimization of parameters intrinsic to the neural network concept. Thus, the weights of a neural network are its memory and thus contain its ability to predict output values based on the input values provided to the input layer of the network. During the training phase, a so-called learning function is used to optimize these weights to best match the input and output data we have provided in our training set. Unfortunately, there are a large number of learning functions that have been developed with highly variable capabilities depending on the problem to be addressed. It is therefore inevitably something that has to be optimized, just like the transfer functions that often transform non-linearly the signals that pass through each neuron of the network. For information purposes, Table II-2 shows all the functions that have been evaluated in this work.

Table II-2 All the learning function used in this work

Function name in Matlab	Description	Note
trainbfg	BFGS quasi-Newton backpropagation.	Backpropagation training functions that use gradient derivatives. Supported on GPU.
traincgb	Conjugate gradient backpropagation with Powell-Beale restarts.	
traincgf	Conjugate gradient backpropagation with Fletcher-Reeves updates.	
traincgp	Conjugate gradient backpropagation with Polak-Ribiere updates.	
traingd	Gradient descent backpropagation.	
traingda	Gradient descent with adaptive lr backpropagation.	
traingdm	Gradient descent with momentum.	
traingdx	Gradient descent with momentum & adaptive lr backpropagation.	
trainoss	One step secant backpropagation.	
trainrp	RPROP backpropagation.	
trainscg	Scaled conjugate gradient backpropagation.	Default (GPU)
trainb	Batch training with weight & bias learning rules.	Supervised weight/bias training functions
trainc	Cyclical order weight/bias training.	
trainr	Random order weight/bias training.	
trains	Sequential order weight/bias training.	
trainbu	Unsupervised batch training with weight & bias learning rules.	Unsupervised weight/bias training functions
trainru	Unsupervised random order weight/bias training.	
trainlm	Levenberg-Marquardt backpropagation.	Default (CPU)
trainbr	Bayesian Regulation backpropagation	

It would be naive to think that a simultaneous optimization of all the above-mentioned parameters could be done because it would then correspond to a kind of combinatorial explosion as regards the total number of networks to be optimized. It would not be justified to find the best neural network either, our objective for this thesis being to demonstrate the feasibility of such an approach and therefore a good model could perfectly suffice. The reverting to the impossibility of setting up a systematic study of the parameters will certainly give the reader an impression of linear optimization based on trials and errors but it is difficult to envisage anything else in this particular context. In this work, we will develop more than 15 types of neural network architecture in order to try to predict the concentration of elements. The Table II-3 given as an illustration shows the extent of the work done. It is not necessary to go into it now as we will develop all these networks in detail in the following sections while trying to justify our choices concerning them.

Table II-3 Details about all the ANNs built during the thesis considering the 22 elements to be predicted

No.	Input layer		Hidden layer		Output layer		Learning methods	Data size	Validation checks
	Pre-processing	Number	Number of neurons	Transfer functions	Number of neurons	Transfer functions			
1	spectra/sum(spectra)	2048	10	tansig	22	linear	trainlm	1000	6
2	spectra/sum(spectra)	2048	10	tansig	22		trainbr	1000	6
3	spectra/sum(spectra)	2048	10	tansig	22		trainlm	2000, 5000	6
4	spectra/sum(spectra)	2048	10	tansig	24		trainscg	5000	6
5	spectra/sum(spectra)	2048	10	logsig	2,3		12: trainscg, traincgb, traincgf, traincgp, traingd, traingda, traingdm, traingdx, trainoss, trainrp, trainlm, trainbr	1000, 5000, 10000, 20000,200000	6
6	spectra/sum(spectra)	2048	10	tansig	2,3		10: trainscg, traincgb, traincgf, traincgp, traingd, traingda, traingdm, traingdx, trainoss, trainrp	5000	6
7	spectra/sum(spectra)	2048	20	tansig	2,3		traincgf, traincgb, trainscg	5000, 200000	6
8	spectra/sum(spectra)	2048	10,20,25,30	logsig	2,3		Trainscg (different T and Ne), traincgb (different Ne)	5000, 200000	6
9	spectra/sum(spectra)	2048	10+10	logsig+logsig	2,3		trainscg	20000	6
10	spectra/max(spectra)	2048	10,20,30	logsig	3		trainscg	20000	6
11	spectra/max(spectra)	2048	10+10	logsig+logsig	3		trainscg	20000	6
12	spectra/max(spectra)	2048	10,15,20,30, 40,50	logsig	3,5,10		trainscg	20000	6
13	PCA	24,50,80,100	25,30,35,40, 50,60,80,100	logsig	3,5,8,10,15,20,22		trainscg	20000	6
14	PCA	100	50	logsig	22		trainscg	20000	20
15	PCA	100	50	logsig	24		trainscg	20000, 50000	20

No.	Maximum epochs	CPU/GPU	T (K)		Ne		Elements used in the dataset	Noise	Baseline
			Train	Validation	Train	Validation			
1	1000	CPU	varied for dataset[1]	-	varied for dataset	-	22	0.001	none
2	1000	CPU	varied for dataset	-	varied for dataset	-	22	0.001	none
3	1000	CPU	varied for dataset	-	varied for dataset	-	22	0.001	none
4	1000	GPU	varied for dataset	-	varied for dataset	-	22	0.001	none
5	1000	GPU/CPU	10000	-	1.00E+17	-	2,3(fixed)	0.001	none
6	5000, 20000	GPU	10000	-	1.00E+17	-	2,3(fixed)	0.001	none
7	1000	GPU	10000	-	1.00E+17	-	2,3(fixed)	0.001	none
8	1000	GPU	varied for datasets[2]				2,3(fixed)	0.001	none
9	1000	GPU	varied for datasets				2,3(fixed)	0.001	none
10	1000, 5000	GPU	varied for datasets				3	0.001	none
11	1000, 5000	GPU	varied for datasets				3	0.001	none
12	5000, 10000	GPU	varied for datasets				3,5,10	0.001	none
13	10000	CPU PARA	varied for datasets				3,5,8,10,15,20,22	0.001	none
14	10000	CPU PARA	varied for spectra[3]				22	0.001,0.005,0.01, 0.02,0.05,0.08,0.1, 0.2	none
15	10000	CPU PARA	varied for spectra				22	0.001,0.005,0.01, 0.02,0.05,0.08,0.1, 0.2	linear, quadratic curves, mix of both

---

[1] Varied for dataset means that within the datasets, T or Ne are the same for each spectrum.

[2] For *trainscg*, both T and Ne are varied for spectra, for *traincgb*, Ne is varied for spectra, T is 10000K.

[3] Varied for spectra means that T and Ne are different within one dataset.

The development of our ANN approach will thus follow the steps shown in figure Fig. II-2.

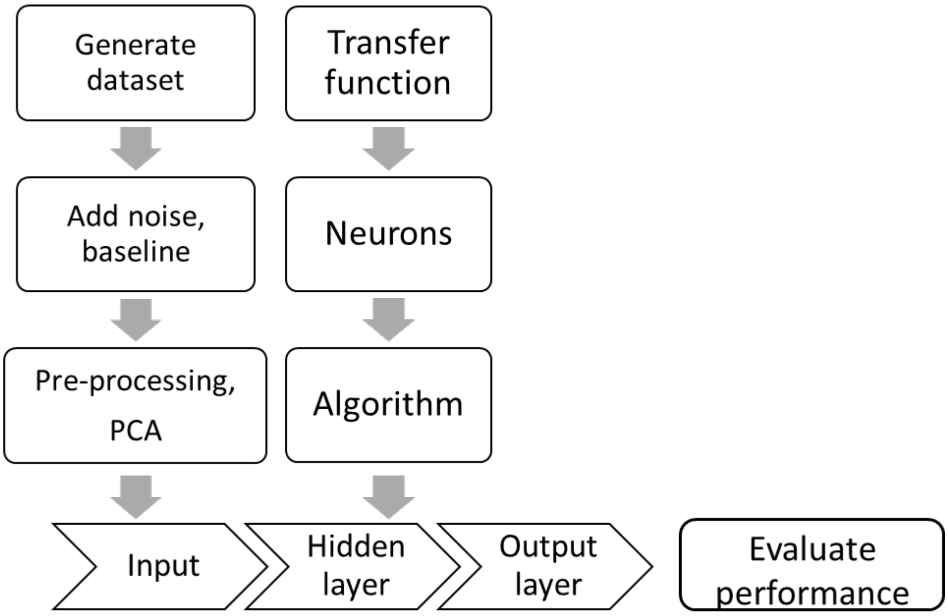

Fig. II-2 The scheme of the training

In a first step, we will generate our training and test sets by varying the temperature and electron density. Each of the two sets will then consist of several thousand spectra/concentration pairs. We will then choose the different perturbations to be applied to the spectra as well as the architecture of the network and the parameters intrinsic to the learning. This data will then be used for the learning phase of the network. Finally, the predictive potential of the constructed network will be evaluated using the spectra contained in the test set that did not participate in the training. Four different figures of merit will then be used to estimate the performance of the models and thus compare them:

The Root Mean Square Error (RMSE)

It is defined by equation II-1 and can be used on the training set and on the test set (i.e. RMSEC and RMSEP respectively).

$$RMSE = \sqrt{\frac{\sum_{i=1}^{n}(\hat{y_i} - y_i)^2}{n}} \qquad \text{II-1}$$

with n being the number of sample in the considered set, $\hat{y_i}$ the predicted value of the neural network for the sample , and y_i the reference value (in our case the real concentration of element)

The Mean Square Error (MSE)

It is given in in the equation II-2. It is by definition the square of the RMSE value.

$$MSE = \frac{1}{n}\sum_{i=1}^{n}(y_i - \hat{y}_i)^2 \tag{II-2}$$

The coefficient of determination (R²)

It is one of the most commonly used parameters in many areas. Its definition is given in equation II-3 with n the number of sample in the dataset, y_i the reference value of sample i, $\bar{y}$ the mean value of the all y_i, and $\widehat{y_i}$ the predicted value by the network for the sample i. R^2 is also the proportion of the variance in the dependent variable which is predictable from the independent variable(s).

$$R^2 = 1 - \frac{\sum_{i=1}^{n}(y_i - \bar{y})^2}{\sum_{i=1}^{n}(y_i - \widehat{y_i})^2} \tag{II-3}$$

The calculation time

The calculation time will also be a parameter to be taken into account. Indeed, some networks will take a long time to train and even if they give the best errors on paper, you will have to ask yourself the question of the real added value compared to others which will be slightly less efficient but which will be undeniably faster to train. We will also have to look at the different learning methods that can support GPU computing versus others that can only run on CPU. It will be all the more important to do this study because the most efficient learning algorithms will not necessarily be those that take advantage of parallel computing on GPUs. Before going into the details of this neural network optimization, which will be detailed in the following sections, we thought it would be interesting to show in table 3.4 a synthesis of the 15 types of neural networks that have been developed in this thesis. The objective here is to better reflect the importance of the work that may have been a bit thankless in the face of some disappointing results, but which are after all an integral part of scientific research

II.1.4 The first ANN

In the very beginning of this project, a simple neural network (ANN No.1) was built based on the example from Matlab neural network tutorial. It has 2048 neurons (corresponding to the 2048 in the spectral domain) as input, one hidden layer with 10 neurons. The transfer function was a sigmoid and the output layer had a linear transfer function. 22 output neurons were also considered (all the concentrations of 22 elements used for the dataset). Raw data was also considered in this first attempt. The training method was the well-known Levenburg-Marquardt backpropagation (trainlm in Matlab).

It is one of the fastest methods in the Matlab toolbox but takes more memory and only runs on CPU. The training phase was then force to stop once the network matches one of the following conditions:

1. reaching maximum epoch (1000 by default),
2. reaching the minimum gradient (1.00×10^{-7}),
3. the performance (mean square error, MSE) reaches zero,
4. reaching the maximum validation checks (6 is the default number, which means the differences in MSE from the last two epochs no longer decreases 6 times in a row, the training no longer improves the MSE),
5. reaching the maximum *mu* (a parameter of Levenburg-Marquardt backpropagation).

The dataset used for training contained 1 000 simulated spectra. It was randomly divided into a training set (75%), a validation set (15%) and a test set (15%) by the toolbox. Fig. II-3 shows an example of the window displayed by our ANN Matlab toolbox at the end of the network learning process. It first recalls the structure of the network we trained, the algorithms used but also proposes a set of information related to the end of the learning phase. Thus, the training of this network stopped after 75 iterations (i.e. epochs) for a total calculation time of 12 hours which is enormous. It should be noted that the learning algorithm chosen here only runs on a CPU, which explains this slowness. We should also not forget that our network is made of 2048 input neurons and 10 hidden layer neurons which makes more than 20000 weights to be optimized during the training. We will observe MSE value of 33.2 at the end of the learning process. Moreover, the green rectangle indicates that the learning process has been stopped because it has reached the maximum validation checks which is 6. This type of representation will be used regularly for the other networks built for comparison.

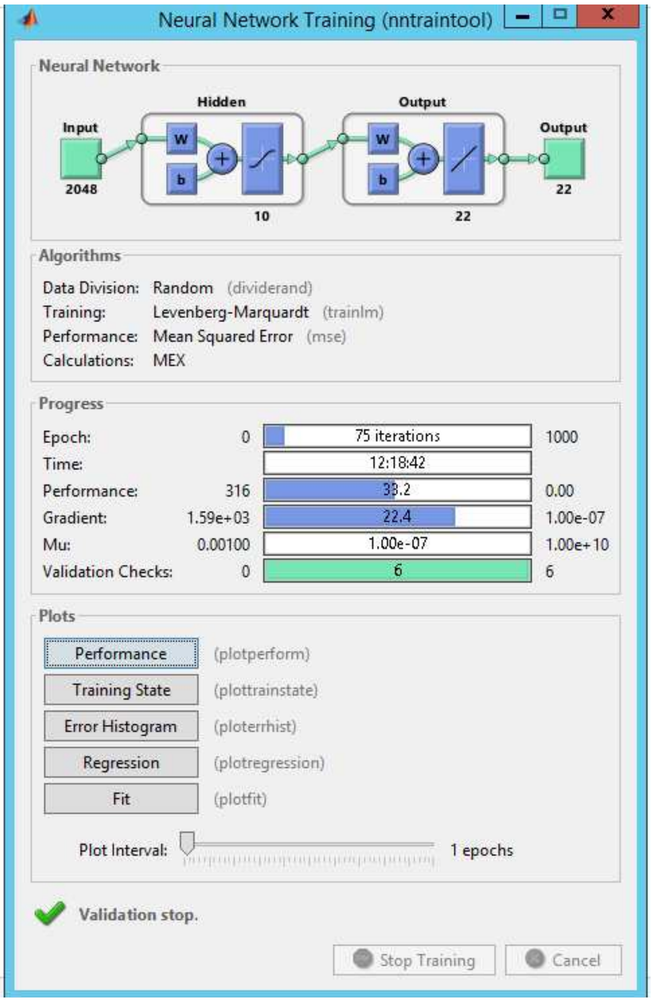

Algorithms

Data Division: Random (dividerand)
Training: Levenberg-Marquardt (trainlm)
Performance: Mean Squared Error (mse)
Calculations: MEX

Progress

Epoch:	0	75 iterations	1000
Time:		12:18:42	
Performance:	316	33.2	0.00
Gradient:	1.59e+03	22.4	1.00e-07
Mu:	0.00100	1.00e-07	1.00e+10
Validation Checks:	0	6	6

Plot Interval: 1 epochs

✓ Validation stop.

Fig. II-3 Neural network No.1

Fig. II-4 also gives very interesting information about the learning phase and the predictive potential of the constructed network. We will also use this type of representation throughout this chapter. More precisely Fig. II-4(a) gives information on the evolution of the MSE values over the iterations on the three datasets (training in blue, validation in green and test in red). The black vertical dash line and the green circle indicate the best performance for the validation set, i.e. a MSE value of 37.8937 obtained at the 69th epoch. Fig. II-4(c) allows to follow the evolution of the parameters of the learning function (gradient and mu in this case) during the training of the network as well as the validation check count. Fig. II-4(b) and (d) give more details on the values predicted by the network. Fig. II-4(d) is a classical representation of the reference values according (target) to the values predicted by the network (output). The dotted line is the first bisector which represents the ideal line where the predictions would be exactly equal to the reference values. We will therefore try to have the points of this figure as close as possible to this line during this work. The colored lines represent the regression lines calculated from the black points of each graph. In other words, they should be as close as possible to the first bisector if the prediction model was perfect. Note that this same figure shows different dials to reflect the prediction results on the three sets of spectra (training in blue, validation in green and test in red). Finally, Fig. II-4 (b) shows the distribution of the prediction error (predicted values – reference ones) for the three datasets. From these first results, we see that such a network is unable to predict concentrations with an excessively high error and a more than moderate correlation and all this for a training time of 12h.

In this case, MSE is 37.8937, R is 0.7273 for the whole dataset (on average), the training stopped at the 75th iteration after 12 hours. These results should be considered poor, since the concentration of one element is between 0 and 1, the MSE is more than 100 times bigger. The possible solutions are: bigger datasets, less output, more neurons, more hidden layers, different learning method and so on.

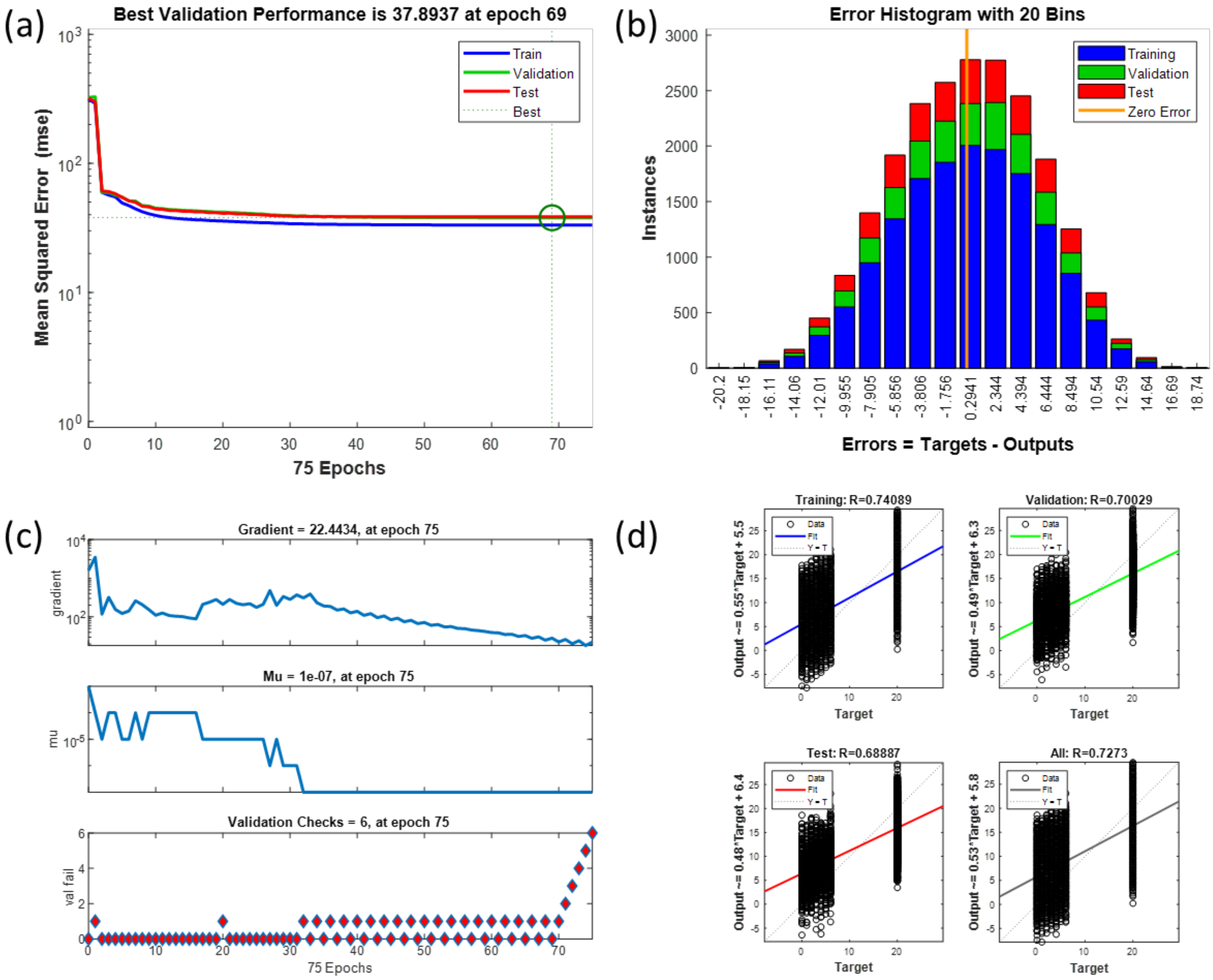

Fig. II-4 Results of ANN No.1

II.1.5 In search of a solution of our learning problem: a different learning method?

Based on these first disappointing results, we first thought that this could be due to the learning function used during the training of the network. So, we decided to use this time the Bayesian Regularization function but keeping the same previous network structure and datasets (ANN No.2). The results are presented in Fig. II-5 and Fig. II-6. As we can see the training was much longer since the training stopped after 1000 iterations for a total computing time of 96 hours! The worst thing was certainly to see that on top of that the level of error had not evolved and therefore still unacceptable. Only the error distribution seemed to improve as we can see on the histogram.

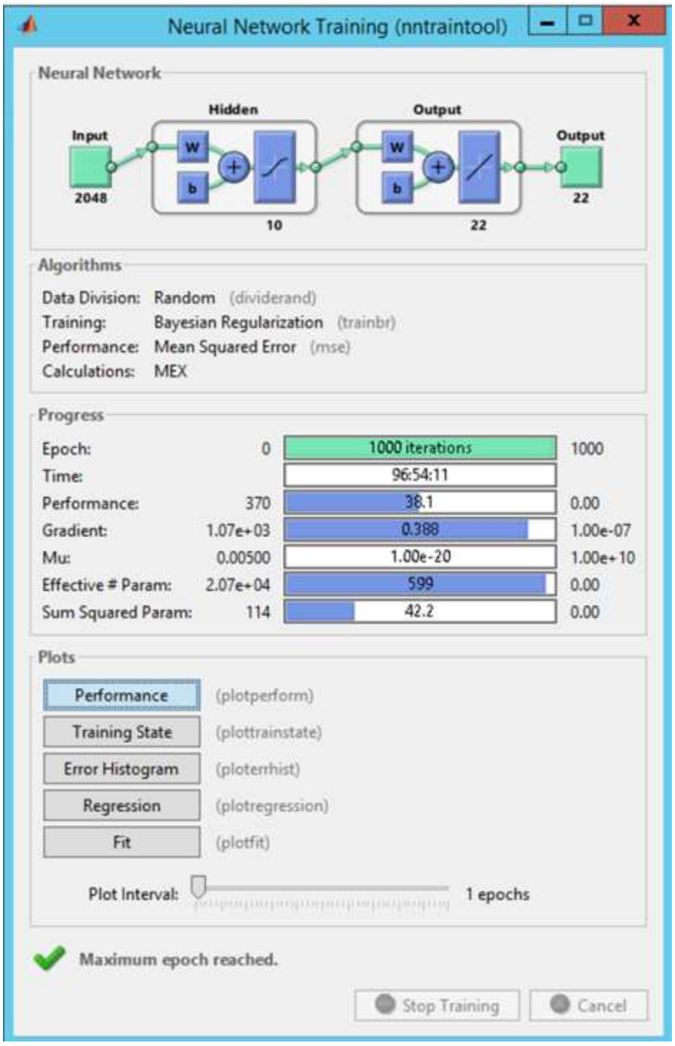

Algorithms

Data Division: Random (dividerand)
Training: Bayesian Regularization (trainbr)
Performance: Mean Squared Error (mse)
Calculations: MEX

Progress

Epoch:	0	1000 iterations	1000
Time:		96:54:11	
Performance:	370	38.1	0.00
Gradient:	1.07e+03	0.388	1.00e-07
Mu:	0.00500	1.00e-20	1.00e+10
Effective # Param:	2.07e+04	599	0.00
Sum Squared Param:	114	42.2	0.00

✓ Maximum epoch reached.

Fig. II-5 ANN No.2

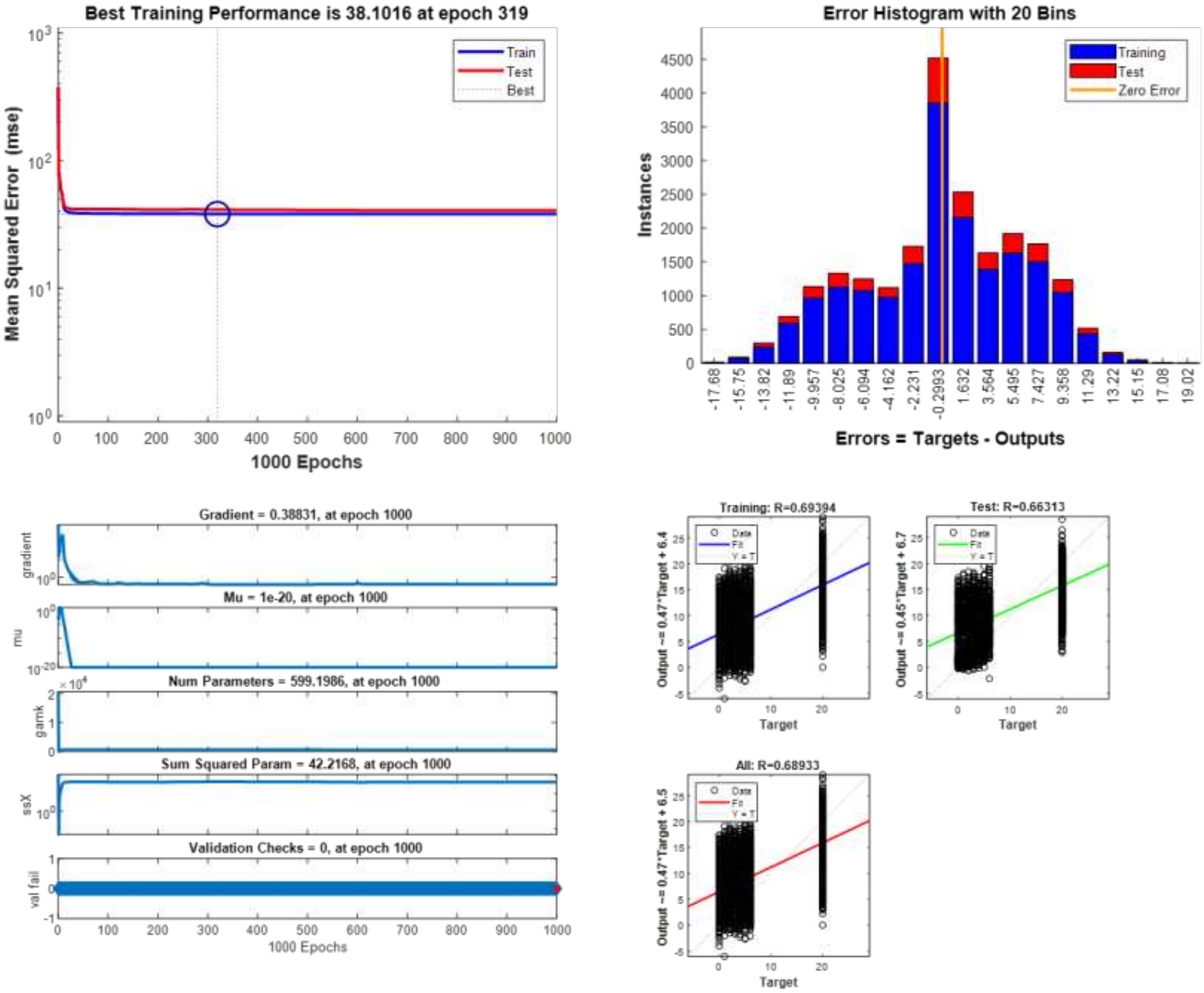

Fig. II-6 Results of ANN No.2

This second network was therefore no more acceptable than the previous one and it was necessary to do something completely different. We assumed that neural networks were very sensitive to the range of values used as input. This is indeed all the more important as the transfer functions tend to accentuate this sensitivity. Thus, we decided to work on the normalization of the input data of the network presented in the following network.

II.1.6 Pre-processing for the input, a normalization?

The two networks mentioned above both used raw data, and the results were bad. Hence the pre-processing of data was considered. In the following trials, normalization was applied. Each spectrum was divided by the sum of all the values along the 2048 spectral variables. Details about this new network No.3 are given in Fig. II-7. The analysis of the result in Fig. II-8 shows that the data normalization allows to go in the right direction with a MSE significantly smaller (0.00204) although R is merely 0.71.

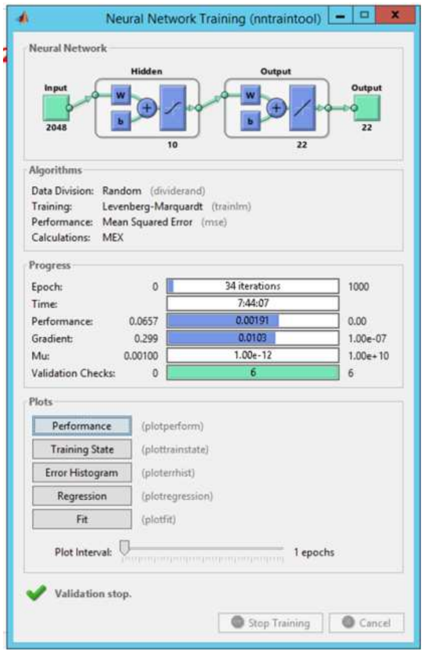

Algorithms
Data Division: Random (dividerand)
Training: Levenberg-Marquardt (trainlm)
Performance: Mean Squared Error (mse)
Calculations: MEX

Progress
Epoch: 0 34 iterations 1000
Time: 7:44:07
Performance: 0.0657 0.00191 0.00
Gradient: 0.299 0.0103 1.00e-07
Mu: 0.00100 1.00e-12 1.00e+10
Validation Checks: 0 6 6

Plots
(plotperform)
(plottrainstate)
(ploterrhist)
(plotregression)
(plotfit)
Plot Interval: 1 epochs

Validation stop.

Fig. II-7 ANN No.3

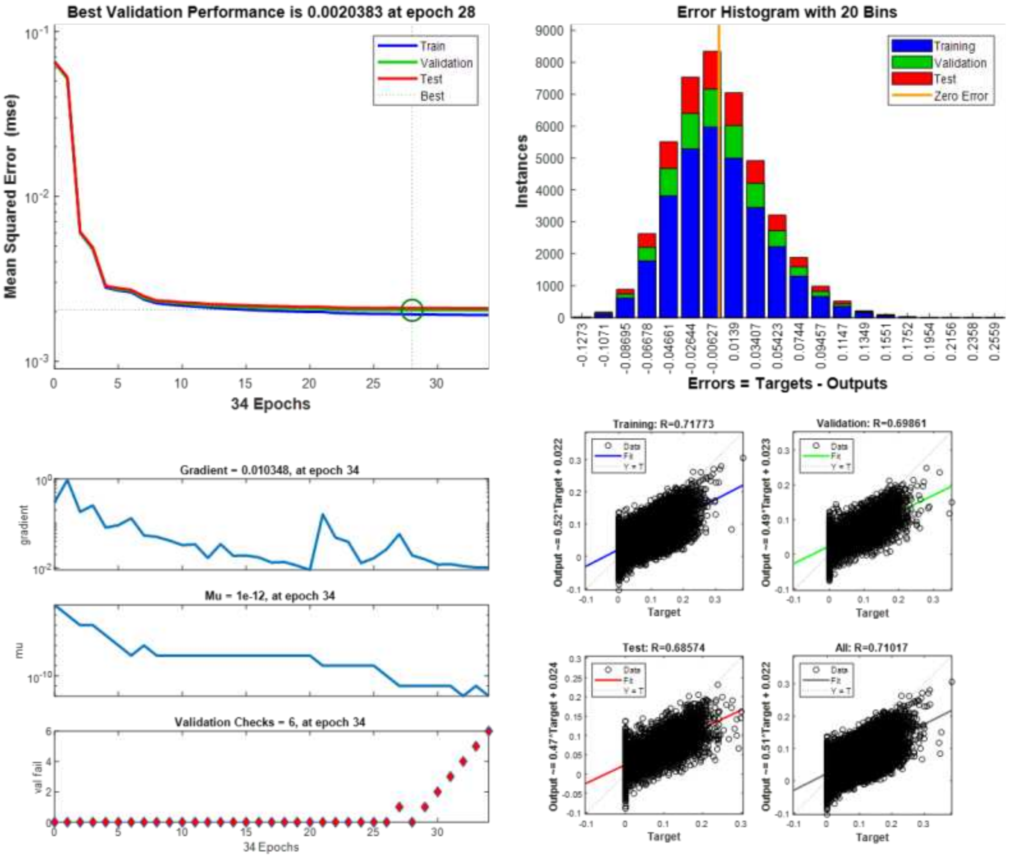

Fig. II-8 Results of ANN No.3

These results were encouraging and showed the importance of normalizing the input data of the neural network. At this point in the work, we also wondered if it would be possible to predict the plasma temperature and electron density in addition to the 22 concentrations through the same network. The results of this network are presented in Fig. II-9. Note that we have kept the parameters of the previous network, only the number of neurons of the output layer is increased to 24 to take into account the prediction of these two new parameters. The results were no more satisfactory than the previous network.

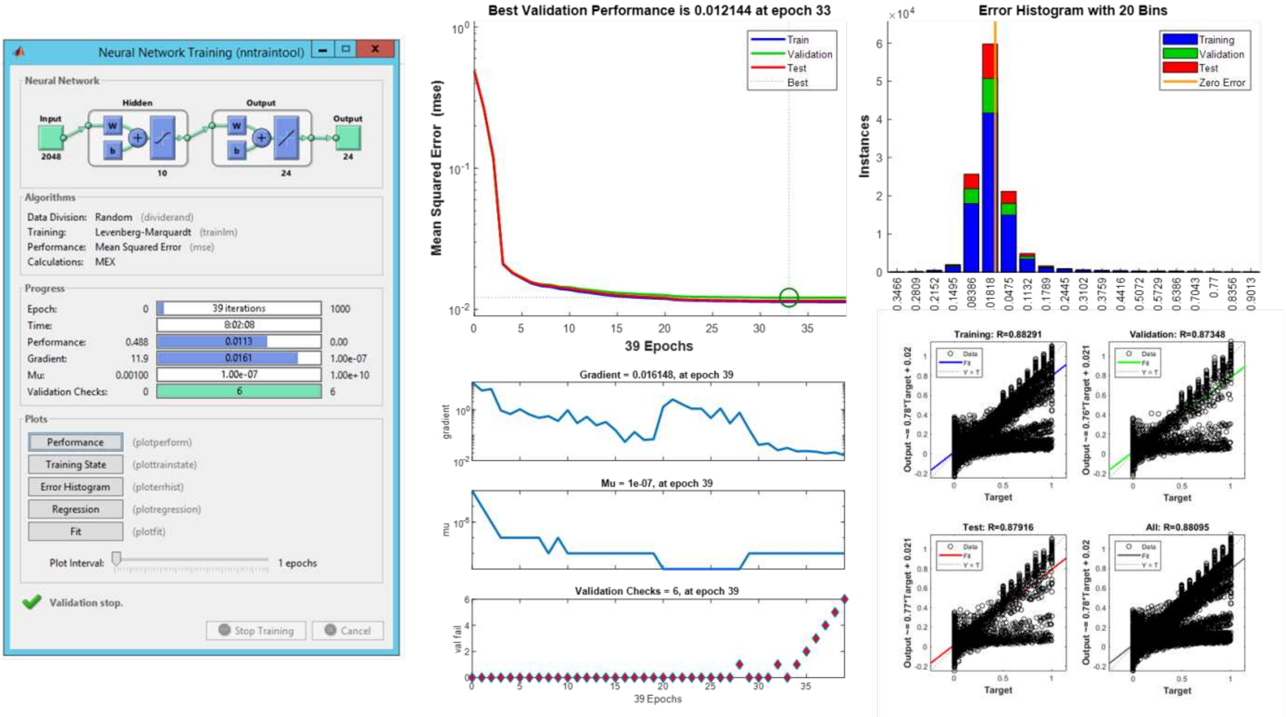
Neural Network Training (nntraintool)

Neural Network

Algorithms
Data Division: Random (dividerand)
Training: Levenberg-Marquardt (trainlm)
Performance: Mean Squared Error (mse)
Calculations: MEX

Progress

Epoch:	0	39 iterations	1000
Time:		8:02:08	
Performance:	0.488	0.0113	0.00
Gradient:	11.9	0.0161	1.00e-07
Mu:	0.00100	1.00e-07	1.00e+10
Validation Checks:	0	6	6

Plot Interval: 1 epochs

Validation stop.

Fig. II-9 Another results of ANN No.3

So far, a few different networks have been built and trained on CPU considering some sets of parameters, but the results were far from good. It was therefore necessary to test more combinations of parameters, but as we saw earlier, the calculation times were far too prohibitive. We therefore decided to prefer learning functions compatible with GPU computing in order to take advantage of parallelization. ANN (No.4) was then built to train on GPU and the default Matlab learning method was chosen (scaled conjugate gradient backpropagation, called *trainscg* in Matlab). This network was built as the previous one. With this GPU implementation, training time was significant shortened into several seconds. However, this ANN had similar results. Since we now had the ability to train networks very quickly we had the opportunity to test many combinations of parameters but this could not improve the performance of the network for predicting concentrations. We then assumed that a single network might not be able to predict all the concentrations of the elements of interest. The time was therefore to build networks with fewer output neurons, i.e. predicting only a few elements. This inevitably led to the need to train different networks to predict the 22 elements, but we needed to know whether the difficulty of the network to predict was due to its output structure.

II.1.7 Considering less output neurons?

The objective of this part was to simplify the neural networks in order to understand whether the modelling problem concerned this point. As far as the datasets used are concerned we have not changed anything as each spectrum is always a linked combination of the 22 elements. However, this time the network only predicts 2 or 3 elements that have been chosen by chance, namely Ag and Al or Ag, Al and As respectively. A series of networks (No.5) were built with data size varied from 1 000 to 200 000 spectra. It was also important to consider the number of spectra in the training set as it must be large enough in relation to the total number of weights in the network to be optimized. Unfortunately, there is no real criterion for choosing this parameter, hence the need to study the influence of the number of spectra. We then studied 12 different learning methods and the sigmoid and linear transfer function for the hidden and output layers respectively. A 0.1% noise were also added to the spectral data. The prediction performances of all these networks are listed in the Table II-4 and Table II-5

Table II-4 Results of ANN No.5 with 2 elements

Learning methods	Datasize	Iterations	MSE	R	Noise	Layer1 FCN	Layer2 FCN	No. elements
trainscg	1000	28	3.37E-04	0.9845	0.001	logsig	purelin	2
	5000	42	6.60E-04	0.98899				
	10000	189	2.07E-05	0.9983				
	20000	735	3.27E-06	0.99966				
traincgb	1000	31	2.04E-04	0.97557	0.001	logsig	purelin	2
	5000	66	1.34E-04	0.99435				
	10000	186	1.92E-05	0.99821				
	20000	362	1.52E-05	0.99952				
	200000	982	5.20E-06	0.99997				
traincgf	1000	30	1.69E-04	0.98521	0.001	logsig	purelin	2
	5000	33	9.98E-04	0.98639				
	10000	199	2.00E-05	0.99728				
	20000	203	6.69E-05	0.99887				
	200000	1000	1.18E-05	0.99993				
traincgf	1000	17	4.82E-04	0.97804	0.001	logsig	purelin	2
	5000	47	4.19E-04	0.99228				
	10000	203	4.79E-05	0.99826				
	20000	607	2.08E-05	0.9994				
	200000	1000	1.91E-05	0.99988				
traincgp	1000	22	9.92E-04	0.98196	0.001	logsig	purelin	2
	5000	50	3.83E-04	0.99175				
	10000	177	2.69E-05	0.99783				
	20000	204	6.71E-05	0.99885				

	200000	878	6.87E-06	0.99995				
traingd	1000	1000	2.07E-02	0.86266	0.001	logsig	purelin	2
	5000	1000	3.45E-02	0.83138				
	10000	1000	2.90E-02	0.86151				
	20000	1000	3.36E-02	0.83963				
	200000	1000	2.82E-02	0.83602				
traingda	1000	284	4.68E-04	0.96756	0.001	logsig	purelin	2
	5000	146	5.43E-03	0.96321				
	10000	149	7.28E-03	0.95239				
	20000	145	7.14E-03	0.95529				
	200000	139	8.96E-03	0.94544				
traingdm	1000	1000	1.91E-02	0.88809	0.001	logsig	purelin	2
	5000	1000	2.46E-02	0.84907				
	10000	1000	2.01E-02	0.8751				
	20000	1000	2.31E-02	0.85995				
	200000	1000	3.43E-02	0.81994				
traingdx	1000	182	1.70E-04	0.97871	0.001	logsig	purelin	2
	5000	194	1.05E-03	0.98848				
	10000	180	1.79E-03	0.98677				
	20000	184	2.30E-03	0.98461				
	200000	185	2.31E-03	0.986				
trainoss	1000	50	4.29E-04	0.97008	0.001	logsig	purelin	2
	5000	44	1.77E-03	0.98418				
	10000	102	6.24E-04	0.99337				
	20000	277	1.19E-04	0.99879				
	200000	1000	5.02E-05	0.99968				
trainrp	1000	41	2.19E-03	0.91551	0.001	logsig	purelin	2
	5000	18	4.64E-03	0.91588				
	10000	46	1.10E-03	0.96642				
	20000	104	5.80E-04	0.97373				
	200000	1000	3.44E-05	0.99978				
trainlm	1000	8	1.31E-17	0.98299	0.001	logsig	purelin	2
	5000	8	2.10E-15	0.99131				
trainbr	5000	30	5.90E-16	0.99967	0.001	logsig	purelin	2
	20000	55	3.25E-06	0.99998				

Table II-5 Results of ANN No.5 with 3 elements

Learning methods	Datasize	Iterations	MSE	R	Noise	Layer1 FCN	Layer2 FCN	No. elements
trainscg	1000	31	5.27E-04	0.98077	0.001	logsig	purelin	3
	5000	78	6.23E-04	0.99144				
	10000	89	5.84E-04	0.99231				
	20000	1000	4.30E-06	0.99985				
	100000	1000	4.46E-06	0.99997				
	200000	1000	6.97E-06	0.99995				
traincgb	1000	48	1.72E-04	0.98735	0.001	logsig	purelin	3
	5000	63	6.39E-04	0.98943				
	10000	765	4.14E-06	0.99777				
	20000	1000	4.36E-06	0.9999				
	200000	1000	4.35E-06	0.99997				
traincgf	1000	42	2.57E-04	0.98461	0.001	logsig	purelin	3
	5000	57	9.46E-04	0.98684				
	10000	91	5.45E-04	0.99369				
	20000	1000	1.46E-05	0.99965				
	200000	1000	2.89E-05	0.9998				

traincgf	1000	57	1.26E-04	0.9837	0.001	logsig	purelin	3
	5000	70	6.60E-04	0.99046				
	10000	65	7.83E-04	0.99153				
	20000	1000	3.52E-05	0.99954				
	200000	1000	3.85E-05	0.99973				
traincgp	1000	75	8.06E-05	0.98522	0.001	logsig	purelin	3
	5000	80	5.21E-04	0.99163				
	10000	96	6.67E-04	0.99204				
	20000	446	3.99E-05	0.9992				
	200000	1000	9.04E-06	0.99994				
traingd	1000	1000	2.85E-02	0.78923	0.001	logsig	purelin	3
	5000	1000	3.13E-02	0.79981				
	10000	1000	2.95E-02	0.81447				
	20000	1000	2.99E-02	0.78611				
	200000	1000	3.16E-02	0.76625				
traingda	1000	147	3.29E-03	0.96113	0.001	logsig	purelin	3
	5000	148	7.65E-03	0.94544				
	10000	150	7.44E-03	0.94711				
	20000	147	7.47E-03	0.94727				
	200000	154	7.19E-03	0.95048				
traingdm	1000	1000	2.50E-02	0.81436	0.001	logsig	purelin	3
	5000	1000	2.53E-02	0.83677				
	10000	1000	3.21E-02	0.77941				
	20000	1000	2.35E-02	0.84205				
	200000	1000	2.92E-02	0.81904				
traingdx	1000	156	1.43E-03	0.9665	0.001	logsig	purelin	3
	5000	193	1.71E-03	0.98363				
	10000	191	2.58E-03	0.98055				
	20000	188	3.13E-03	0.97749				
	200000	199	3.18E-03	0.97808				
trainoss	1000	54	4.52E-04	0.97965	0.001	logsig	purelin	3
	5000	79	1.12E-03	0.98753				
	10000	99	1.30E-03	0.98933				
	20000	476	2.26E-04	0.99735				
	200000	1000	2.22E-05	0.99984				
trainrp	1000	64	4.63E-03	0.9416	0.001	logsig	purelin	3
	5000	37	4.21E-03	0.95323				
	10000	151	2.54E-03	0.95362				
	20000	114	1.74E-03	0.97699				
	200000	1000	1.41E-04	0.99901				
trainlm	1000	7	1.18E-21	0.9782	0.001	logsig	purelin	3
	5000	22	2.82E-06	0.99991				
	20000	19	1.28E-05	0.99981				
trainbr	5000	17	4.31E-04	0.99681	0.001	logsig	purelin	3
	20000	65	8.37E-07	0.99998				

From a general point of view, we can already see that the networks have a very different prediction behavior with now much more acceptable MSE and R values. If we first look at the learning functions, we can see that some are worse than others, for example gradient descent backpropagation (*traingd*) and gradient descent with momentum (*traindm*). Additionally, the Levenberg-Marquardt backpropagation (*trainlm*) and Bayesian Regularization (*trainbr*) can only run with CPU. Therefore, they need much more time to train and make them difficult to use on big datasets. The scaled conjugate gradient backpropagation has then been considered as the learning function to keep in this part.

Regarding the size of the training dataset, we could test values from 1000 to 200000 LIBS spectra In all these networks, the maximum epoch chosen was 1000 and it was not enough for a dataset of 200 000, since most of these ANNs (No.5) stopped by reaching this limit i.e. without reaching the end of the training step. Of course, we could have increased this limit, but such a training already lasted more than 10 minutes. This time obviously seemed much shorter than before, but it was still too long for the many tests we had to do afterwards. In view of these results, it appeared to us that training the networks on a training set of 20,000 spectra allowed the networks to be trained for a time ranging from a few seconds to a few minutes while ensuring acceptable MSE and R values.

II.1.8 Considering different transfer function and/or different number of hidden neurons?

The transfer function of a neuron has a very important place in a network because it transforms the weighted sum of its inputs into a new output value which is then passed on to the next neuron in another layer. Sigmoid (*logsig* in Matlab) and tan-sigmoid (*tansig* in Matlab) are the most common transfer functions used in the hidden layers of a network. Their difference is illustrated in Fig. II-10.

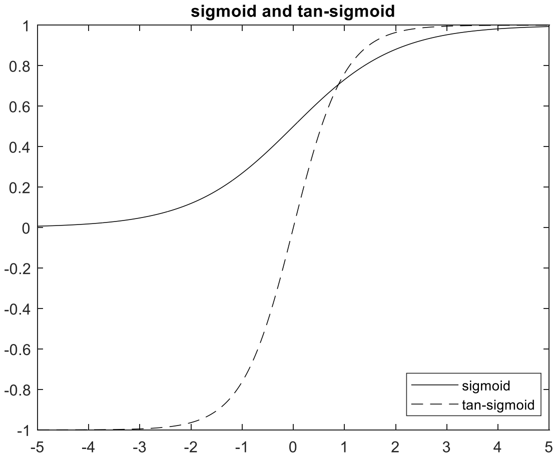

Fig. II-10 The Sigmoid and tan-sigmoid transfer functions

Although this may seem trivial, these two functions are quite different because the first will present outputs bounded between 0 and 1 while the second will also propose negative values on a domain from -1 to +1. The transfer function of the output layer is a linear one called *purelin* in Matlab. Table II-6 and Table II-7 give the results of ANN(No.6) trained with tan-sigmoid as transfer function in the hidden layer. We still consider networks built to predict 2 or 3 elements but this time limiting the total number of spectra in the dataset to 20,000.

Table II-6 Results of ANN No.6 with 2 elements

Learning methods	Datasize	Iterations	MSE	R	Noise	Layer1 FCN	Layer2 FCN	No. elements
trainscg	5000	73	2.59E-05	0.98984	0.001	tansig	purelin	2
	20000	1000	2.87E-06	0.99992				
traincgb	5000	172	2.08E-07	0.97693	0.001	tansig	purelin	2
	20000	356	7.11E-06	0.9999				
traincgf	5000	59	2.07E-04	0.99309	0.001	tansig	purelin	2
	20000	423	4.13E-06	0.99942				
traincgp	5000	63	1.44E-04	0.98851	0.001	tansig	purelin	2
	20000	270	1.35E-05	0.99941				
traingd	5000	1000	2.70E-02	0.81495	0.001	tansig	purelin	2
	20000	1000	3.21E-02	0.81868				
traingda	5000	358	8.35E-04	0.97229	0.001	tansig	purelin	2
	20000	209	3.64E-03	0.97332				
traingdm	5000	1000	2.51E-02	0.83636	0.001	tansig	purelin	2
	20000	14	1.80E-01	0.67192				
traingdx	5000	182	3.21E-04	0.98592	0.001	tansig	purelin	2
	20000	184	1.29E-03	0.98981				
trainoss	5000	63	3.82E-04	0.98249	0.001	tansig	purelin	2
	20000	171	2.26E-04	0.99712				
trainrp	5000	74	3.96E-03	0.93708	0.001	tansig	purelin	2
	20000	115	2.12E-03	0.96161				

Table II-7 Results of ANN No.6 with 3 elements

Learning methods	Datasize	Iterations	MSE	R	Noise	Layer1 FCN	Layer2 FCN	No. elements
trainscg	5000	82	3.04E-04	0.98663	0.001	tansig	purelin	3
	20000	1000	4.83E-06	0.99994				
traincgb	5000	126	1.17E-04	0.98768	0.001	tansig	purelin	3
	20000	470	2.34E-05	0.99963				
traincgf	5000	92	2.48E-04	0.99096	0.001	tansig	purelin	3
	20000	505	1.54E-04	0.99872				
traincgp	5000	42	1.20E-03	0.98052	0.001	tansig	purelin	3
	20000	139	1.66E-04	0.99717				
traingd	5000	1000	1.92E-02	0.87499	0.001	tansig	purelin	3
	20000	1000	1.92E-02	0.86751				
traingda	5000	137	6.07E-03	0.94274	0.001	tansig	purelin	3
	20000	138	6.26E-03	0.95335				
traingdm	5000	1000	2.71E-02	0.82758	0.001	tansig	purelin	3
	20000	1000	3.71E-02	0.77697				
traingdx	5000	177	1.22E-03	0.97709	0.001	tansig	purelin	3
	20000	192	1.45E-03	0.98844				
trainoss	5000	68	1.78E-03	0.97685	0.001	tansig	purelin	3
	20000	453	5.68E-05	0.99928				
trainrp	5000	90	1.24E-02	0.89319	0.001	tansig	purelin	3

20000	153	1.54E-02	0.85621

These results show that we are still able to propose satisfactory predictive models. The best learning functions are still the same as previously and the change of transfer function does not allow to obtain a significant improvement in the prediction. Since it is not always clear what lies behind an MSE value or an R, Fig. II-11 shows graphically the results obtained for one of these networks.

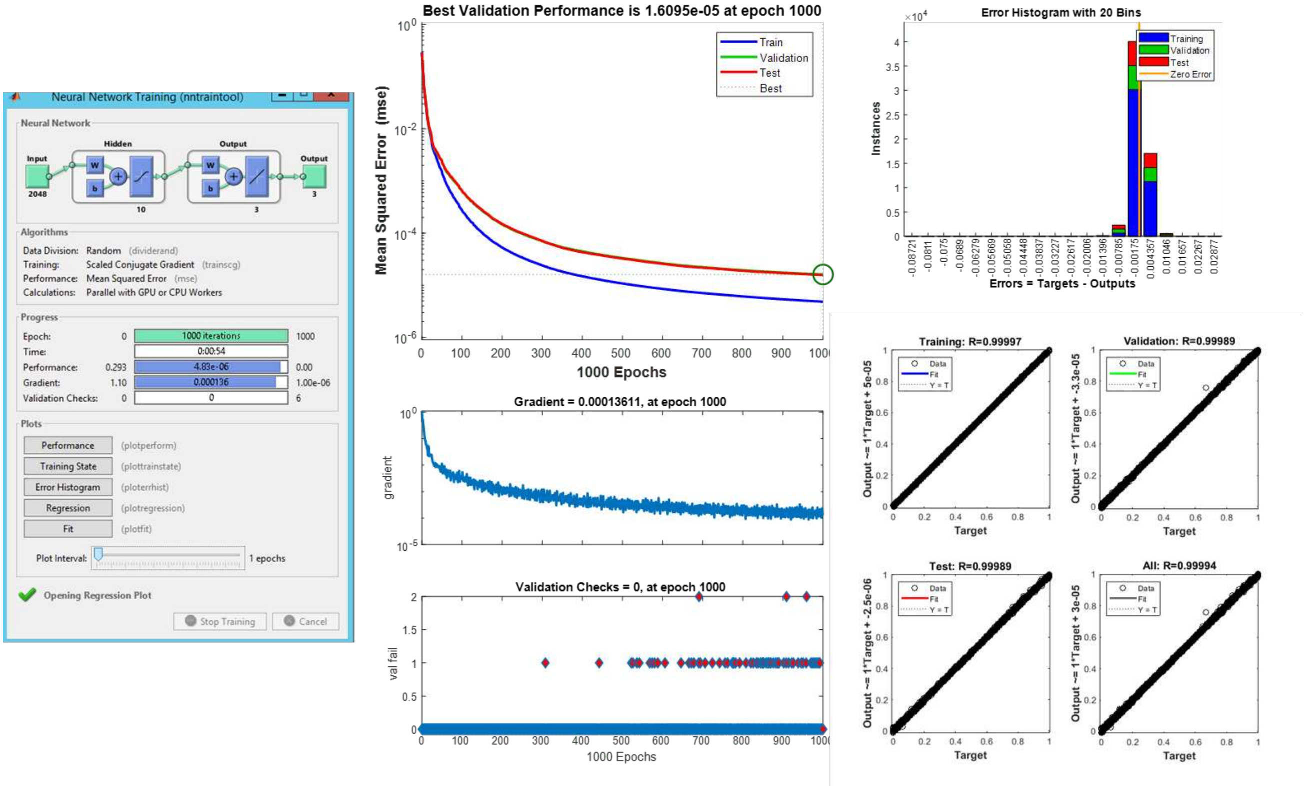

Neural Network Training (nntraintool)

Neural Network

Algorithms

Data Division: Random (dividerand)
Training: Scaled Conjugate Gradient (trainscg)
Performance: Mean Squared Error (mse)
Calculations: Parallel with GPU or CPU Workers

Progress

Epoch: 0 1000 iterations 1000
Time: 0:00:54
Performance: 0.293 4.83e-06 0.00
Gradient: 1.10 0.000136 1.00e-06
Validation Checks: 0 0 6

Plots

Plot Interval: 1 epochs

Opening Regression Plot

Fig. II-11 One example of ANN No.6

In spite of our discourse, which may seem a little negative at times, the graphs on the right-hand side of the figure show that we have a good quality of prediction with a set of points very close to the first bisector and residues close together in the histogram. So, there is no doubt that we are moving in the right direction. It then appeared interesting to see if we could increase the level of prediction by increasing the number of hidden neurons to 20 while keeping the previous conditions of ANNs N°6. So Table II-8 provides the prediction results of this new structure (ANN N°7).

Table II-8 Results of ANN No.7

Method	Datasize	Iterations	MSE	R	Noise	Layer1 FCN	Layer2 FCN	No. elements

trainscg	5000	79	1.17E-04	0.9948	0.001	tansig	purelin	2
	20000	385	3.47E-05	0.9934				
traincgb	5000	101	1.79E-05	0.99645	0.001	tansig	purelin	2
	20000	173	5.82E-05	0.99885				
traincgf	5000	141	2.11E-05	0.99514	0.001	tansig	purelin	2
	20000	319	2.65E-05	0.99926				
trainscg	5000	91	4.92E-04	0.99328	0.001	tansig	purelin	3
	20000	372	1.17E-04	0.99818				
traincgb	5000	64	6.79E-04	0.99177	0.001	tansig	purelin	3
	20000	395	4.75E-05	0.99897				
traincgf	5000	127	1.27E-04	0.99447	0.001	tansig	purelin	3
	20000	485	5.13E-05	0.99885				

As we can quickly see, we cannot observe a real improvement and we can therefore say that we have reached a certain limit in the predictive capacity of the neural network. Nevertheless, we should not lose sight of the fact that ANNs N°6 and N°7 were built on the basis of LIBS spectral data for fixed plasma temperatures and electron densities. Although this strategy might have seemed simplistic at first, it ultimately paid off because we discovered that it was not so simple to build a network capable of simultaneously predicting multiple concentrations even under these conditions. The observations we made will certainly help us to understand conditions that are even closer to the reality of the experimental data.

II.1.9 Could we manage different temperature and electron density of the plasma?

As said before, the purpose of the series of networks we constructed (ANN N°8) was first to see if it was possible to predict the concentrations of the elements as the temperature and electron density varied. Table II-9 shows the prediction results of ANNs considering a fixed temperature but different electron densities. In general, we could see that the results were quite acceptable and that temperature variations could be taken into account for a given electron density. Nevertheless, we note a difficulty of prediction when the electron densities are different between the training and test sets, which is quite natural (penultimate line of the table).

Table II-9 ANN No.8 with fixed T

Learning methods	Datasize	Iterations	MSE	R	Ne for calibration	Validation R	Ne for validation	Validation datasize	Noise	Layer1 FCN	Layer2 FCN	No. elements
trainscg	5000	65	1.36E-04	0.9943	5.00E+17				0.001	logsig	purelin	2
	20000	791	1.65E-05	0.9996	5.00E+17							
trainscg	5000	72	2.84E-04	0.99367	5.00E+16				0.001	logsig	purelin	3
	20000	1000	5.56E-06	0.9999	5.00E+17	0.93195		5000				

	20000	1000	5.44E-06	0.99996	5.00E+16	0.99996	5.00E+16	5000				
traincgb	5000	105	1.75E-06	0.99602	5.00E+17	0.97862	1.00E+17	5000	0.001	logsig	purelin	2
	20000	135	9.56E-05	0.99865	5.00E+17	0.9969	5.00E+17	5000				
traincgb	5000	92	1.80E-04	0.9924	5.00E+16	0.97684	1.00E+17	5000	0.001	logsig	purelin	3
	20000	856	5.61E-05	0.99983	1.00E+17	0.99953	1.00E+17	5000				

Table II-10 shows the prediction results when we fix the electron density but consider different plasma temperatures between the training and test sets. These results are not really different and are therefore quite acceptable. We can even add that the network has a certain robustness to temperature variations since these networks predict the concentrations quite well while they have never seen spectra with another temperature than the one chosen for the training batch.

Table II-10 ANN No.8 with fixed Ne

Learning methods	Datasize	Iterations	MSE	R	T for calibration	Validation R	T for Validation	Validation datasize	Noise	Layer1 FCN	Layer2 FCN	No. elements
trainscg	5000	51	2.37E-04	0.99322	11000	0.97166	12000	5000	0.001	logsig	purelin	2
	20000	423	5.21E-06	0.99941	6000	0.97273	10000	5000				
trainscg	5000	46	7.39E-04	0.98946	9000	0.98074	9000	5000	0.001	logsig	purelin	3
	20000	1000	4.32E-06	0.99981	11000	0.58782	6000	5000				
	200000	743	6.71E-06	0.99983	9000	0.63743	6000	5000				

In order to improve the predictive power of our models, we wanted to see if increasing the number of neurons on the hidden layer could improve things. Table II-11 shows the result of the predictions considering different temperatures and electron density with an increasing number of neurons ranging from 20 to 30. This variation seems limited, but it should not be forgotten that this number undeniably multiplies the number of weights to be optimized in the network during its training.

Table II-11 Three different hidden neurons values with different T and Ne

	20 neurons	25 neurons	30 neurons
R Train (T: 11 000, Ne: 5e17)	0.99968	0.99949	0.99907
R Validation (T: 9 000, Ne: 1e17)	0.9692	0.97049	0.9648
R Train (T: 9 000, Ne: 5e16)	0.99797	0.99792	0.99863
R Validation (T: 8 000, Ne: 5e16)	0.93946	0.93865	0.9399

We quickly see that this increase does not bring much in terms of predictive power and we can therefore stay with this minimum number of 20 neurons on the hidden layer. At this level of optimization, we again asked ourselves whether or not to add a second layer of hidden neurons. This only made the task of training the network more complex, with the loss of predictive potential as we can see on Fig. II-12 and Fig. II-13 and the observation of non-linear effects on the reference values vs. predicted values graphs.

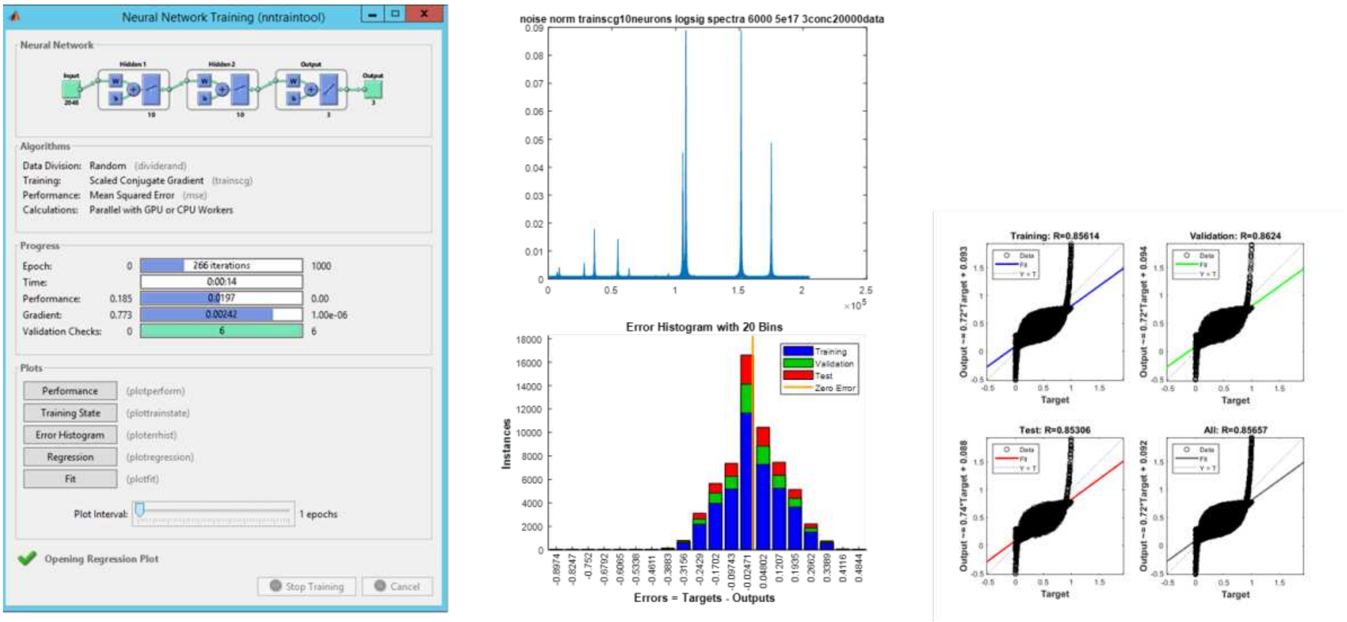

Neural Network Training (nntraintool)

Algorithms
Data Division: Random (dividerand)
Training: Scaled Conjugate Gradient (trainscg)
Performance: Mean Squared Error (mse)
Calculations: Parallel with GPU or CPU Workers

Progress
Epoch: 0 266 iterations 1000
Time: 0:00:14
Performance: 0.185 0.0197 0.00
Gradient: 0.773 0.00242 1.00e-06
Validation Checks: 0 6 6

Opening Regression Plot

Fig. II-12 One example of ANN with extra hidden layer

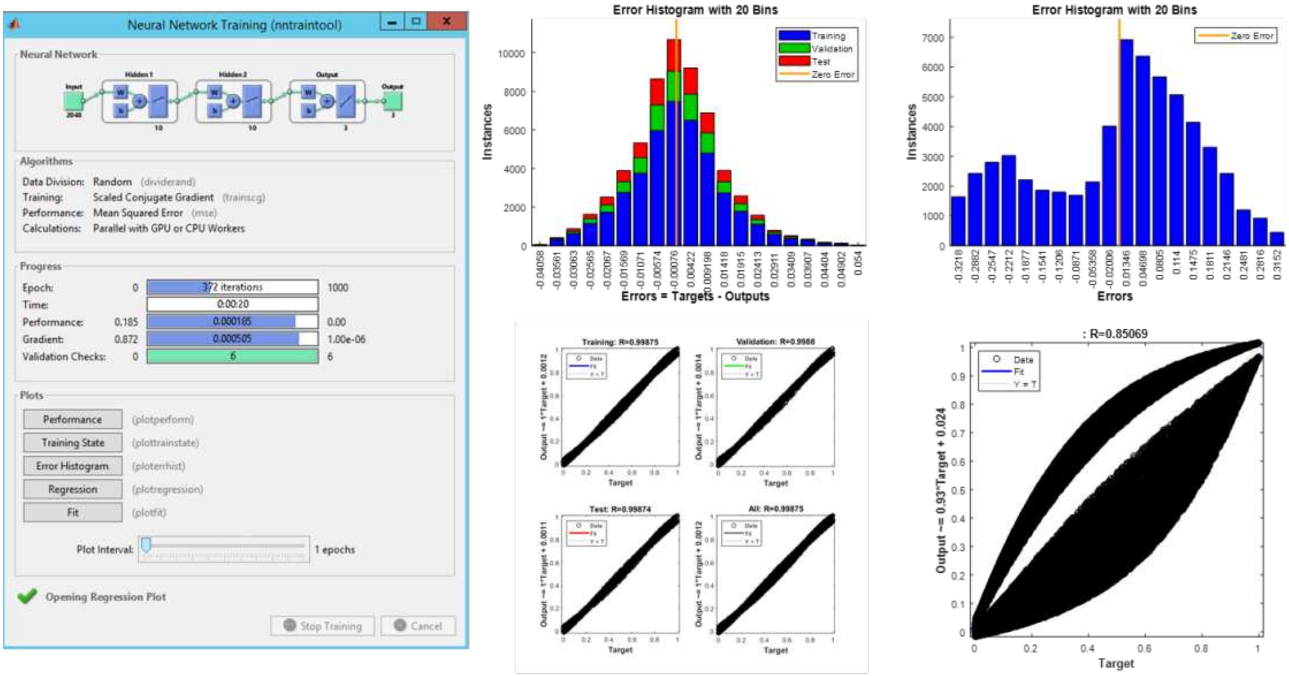

Neural Network Training (nntraintool)

Algorithms
Data Division: Random (dividerand)
Training: Scaled Conjugate Gradient (trainscg)
Performance: Mean Squared Error (mse)
Calculations: Parallel with GPU or CPU Workers

Progress
Epoch: 0 372 iterations 1000
Time: 0:00:20
Performance: 0.185 0.000185 0.00
Gradient: 0.872 0.000505 1.00e-06
Validation Checks: 0 6 6

Opening Regression Plot

Fig. II-13 Another example of ANN with extra hidden layer

II.1.10 A time of reflexion

At this point in the thesis, we had already tested a number of networks and two main questions were added. The first was the normalization used for the input data and the second was the representativeness of the 2 or 3 elements we had chosen by default to be predicted. As far as the first point is concerned, we have seen how important normalization is in order to obtain satisfactory predictions. On the other hand, the normalization by the sum did not allow to cover the whole range of output values of the transfer function which is not optimal in the learning process. With this in mind, we decided to normalize the spectra by dividing them by their maximum value, so that the transformed spectral data would be between 0 and 1. Regarding the second point raised, we had decided in the first part of the thesis to work by default on Ag, Al, and As. We could then ask ourselves whether our difficulties might stem from this particular choice of elements to be predicted or whether modelling in general remained difficult. It was therefore decided to develop neural networks with different combinations of 3 elements from the list of 22 considering different temperatures and electron densities but also considering the new normalization procedure. Scaled conjugate gradient backpropagation (*trainscg*) was the only learning method applied and 10, 20 or 30 hidden neurons were considered in a single layer. The results of these ANNs No.9 are presented in the Table II-12.

Table II-12 Results of ANN No.9

Iterations	Training set plasma parameters	Validation set plasma parameters	MSE training	MSE validation	R training	R validation	Nbr. hydden neurons	Elements considered in the output layer			Epochs
161	11000, 5e17	9000, 1e17	1.90E-03	8.75E-01	0.98693	0.01840	10	As	Pb	Ga	1000
1000	8000, 5e17	10000, 5e17	1.41E-04	2.80E-02	0.99905	0.88610	10	Ti	As	Si	1000
2000	9000, 5e16	6000, 1e17	4.76E-05	1.89E-01	0.99968	0.17017	10	Mn	Ti	Ag	2000
3597	10000, 1e17	7000, 5e17	1.50E-05	1.27E-01	0.99990	0.79216	10	Ti	Si	Al	5000
639	6000, 1e17	7000, 5e16	2.20E-04	1.00E-01	0.99852	0.17039	20	Ca	As	Ti	5000
243	11000, 5e17	6000, 5e16	3.50E-03	2.44E-01	0.97621	0.10943	20	Na	As	Sr	5000
353	11000, 1e17	6000, 5e16	2.90E-03	1.70E-01	0.97996	0.23552	20	Al	Na	As	5000
1376	11000, 1e17	9000, 1e17	3.08E-05	5.40E-02	0.99979	0.71034	20	Mo	Al	U	5000
154	11000, 5e17	9000, 5e16	4.95E-02	1.32E-01	**0.57972**	0.14083	20	Mg	Na	La	5000
1005	11000, 1e17	9000, 1e17	7.91E-05	5.21E-02	0.99946	0.73123	20	Mo	La	Cu	5000
942	11000, 5e16	9000, 5e16	1.59E-04	8.60E-03	0.99892	**0.94074**	20	Si	Al	Cu	5000
1306	11000, 1e17	9000, 5e17	3.23E-05	4.74E-02	0.99978	0.61175	20	Fe	La	Si	5000
884	11000, 5e16	9000, 1e17	6.10E-05	4.56E-02	0.99959	0.66066	20	Ga	La	Fe	5000
713	11000, 5e16	9000, 5e17	4.89E-04	1.01E-01	0.99667	0.60337	20	Ni	Ag	Ti	5000
2842	11000, 5e16	9000, 5e16	1.72E-05	8.18E-02	0.99988	0.78043	20	As	Mo	Ag	5000
649	11000, 5e16	9000, 1e17	8.30E-05	7.12E-02	0.99944	0.52649	20	La	Au	Fe	5000
182	11000, 5e17	9000, 1e17	6.40E-03	1.74E-01	0.95604	0.53477	20	Mg	Au	Ag	5000
3854	11000, 5e16	9000, 5e17	5.01E-06	1.87E-01	0.99997	0.21059	20	Cr	Cu	Ca	5000
387	11000, 5e17	9000, 1e17	1.60E-03	5.21E-02	0.98935	0.83669	20	Na	Ga	Pb	5000
227	11000, 1e17	9000, 5e16	2.20E-03	2.87E-02	0.98502	0.79473	20	Cu	Pb	Ga	5000
260	11000, 1e17	9000, 5e17	1.25E-02	2.04E-01	0.91328	0.05646	20	As	Mg	Sr	5000
575	11000, 1e17	9000, 5e17	2.02E-02	5.86E-01	**0.85282**	-0.02432	20	La	Mo	Mg	5000
130	11000, 1e17	9000, 5e17	4.64E-02	5.16E-01	**0.61053**	0.32034	30	Na	Fe	Mg	5000

447	11000, 5e17	9000, 5e17	2.69E-04	1.40E-02	0.99820	**0.91703**	30	Au	Al	Sr	5000
413	11000, 1e17	9000, 1e17	1.86E-02	1.05E-01	**0.86662**	0.42461	30	Mg	Ag	Mo	5000
2121	11000, 5e16	9000, 1e17	1.89E-05	2.87E-02	0.99987	0.79994	30	As	Fe	Al	5000
993	11000, 5e17	9000, 1e17	2.77E-02	1.16E-01	**0.79173**	0.53309	30	Mg	Na	Fe	5000

This table shows that apart from 5 cases (in bold), the R values for training set are all over 0.9, while only three cases (in bold) have R over 0.9 for validation. We thus observe that some networks perform poorly for particular combinations of elements to be predicted for the same network. Moreover, increasing the number of hidden neurons and the number of iterations did not bring better performance. In these new conditions it was also interesting to know if we could not improve things by considering two layers of 10 neurons each in a new series of ANN No.10 (results in Table II-12).

Table II-13 Results of ANN No.10

Iterations	Training set	Validation set	MSE training	MSE validation	R training	R validation	Hidden neurons	Elements considered in the output layer			Epochs
1000	7000, 1e17	9000, 5e17	6.88E-06	1.10E-03	0.99995	**0.99575**	10+10	Fe	U	La	1000
385	9000, 5e16	10000, 1e17	1.70E-03	1.90E-03	0.98870	**0.98724**	10+10	La	Mg	Ca	1000
406	9000, 1e17	7000, 5e17	4.80E-03	7.96E-02	0.96679	0.80059	10+10	Sr	Mg	Si	1000
1000	9000, 5e17	11000, 5e16	5.52E-05	8.43E-02	0.99963	0.59888	10+10	La	As	Na	1000
1000	11000, 5e17	7000, 5e16	8.18E-06	6.99E-05	0.99994	**0.99956**	10+10	Ni	Pb	Al	1000
384	8000, 5e17	9000, 5e16	1.76E-04	5.27E-02	0.99881	0.70382	10+10	Ca	Ag	Pb	1000
1000	9000, 5e16	10000, 5e16	2.08E-05	1.14E-02	0.99986	**0.93495**	10+10	Na	Sr	Au	1000
263	7000, 5e17	11000, 5e16	2.62E-04	1.06E-01	0.99823	0.37254	10+10	Mn	U	Ca	1000
1000	6000, 1e17	9000, 5e17	7.91E-06	1.45E-02	0.99995	**0.90759**	10+10	Ga	Au	Al	1000
378	7000, 5e17	7000, 5e16	1.74E-04	2.09E-02	0.99882	0.85614	10+10	Cr	Mn	La	1000
1000	10000, 1e17	7000, 5e16	5.09E-06	2.34E-02	0.99997	0.82909	10+10	U	As	Sr	1000
1000	12000, 5e16	9000, 5e16	7.49E-06	3.29E-02	0.99995	0.79150	10+10	U	La	As	1000
1000	7000, 5e16	12000, 1e17	2.75E-04	4.12E-02	0.99815	0.77235	10+10	Mg	Sr	Ga	1000
1000	7000, 5e16	6000, 5e17	5.56E-06	2.53E-02	0.99996	0.87310	10+10	Au	U	Fe	1000
1000	11000, 5e16	12000, 1e17	1.61E-06	1.02E-04	0.99999	**0.99947**	10+10	Al	La	Si	1000
534	6000, 1e17	6000, 1e17	2.54E-05	2.50E-05	0.99983	**0.99983**	10+10	Ga	Ca	Ti	1000
597	11000, 5e16	12000, 1e17	1.50E-03	2.62E-02	0.98964	**0.91238**	10+10	Mn	Na	La	1000
898	7000, 5e17	6000, 5e17	4.22E-06	1.00E-02	0.99997	**0.93400**	10+10	Cr	Na	Sr	1000

666	8000, 1e17	12000, 1e17	2.34E-06	3.15E-02	0.99998	0.80501	10+10	Au	La	Sr	1000
359	12000, 5e17	11000, 5e17	1.68E-02	1.72E-02	**0.87937**	0.88362	10+10	U	Cr	Na	5000
1663	8000, 5e16	6000, 5e16	1.28E-04	1.61E-01	0.99914	0.49702	10+10	La	Fe	Mg	5000
3601	12000, 5e16	6000, 5e16	1.43E-06	2.53E-01	0.99999	0.12979	10+10	U	Al	Ca	5000
1148	8000, 5e17	8000, 5e17	1.06E-04	1.06E-04	0.99929	**0.99927**	10+10	Mn	Mg	Si	5000
350	9000, 5e16	6000, 5e16	3.97E-04	5.26E-02	0.99730	0.69429	10+10	Sr	Cu	Ni	5000
673	9000, 5e16	10000, 5e17	8.55E-06	1.07E-02	0.99994	**0.92941**	10+10	La	Au	Pb	5000
910	11000, 1e17	9000, 5e16	1.01E-04	1.32E-02	0.99932	**0.96285**	10+10	Ti	Au	Pb	5000

These results are quite different from the previous ones with acceptable performance for almost all element combinations with a few exceptions. As an illustration, the Fig. II-14 provides a visual comparison of the predictive capabilities of three given neural networks (i.e. considered three different combination of elements) when one (b) or two (a) hidden layers are considered in the network.

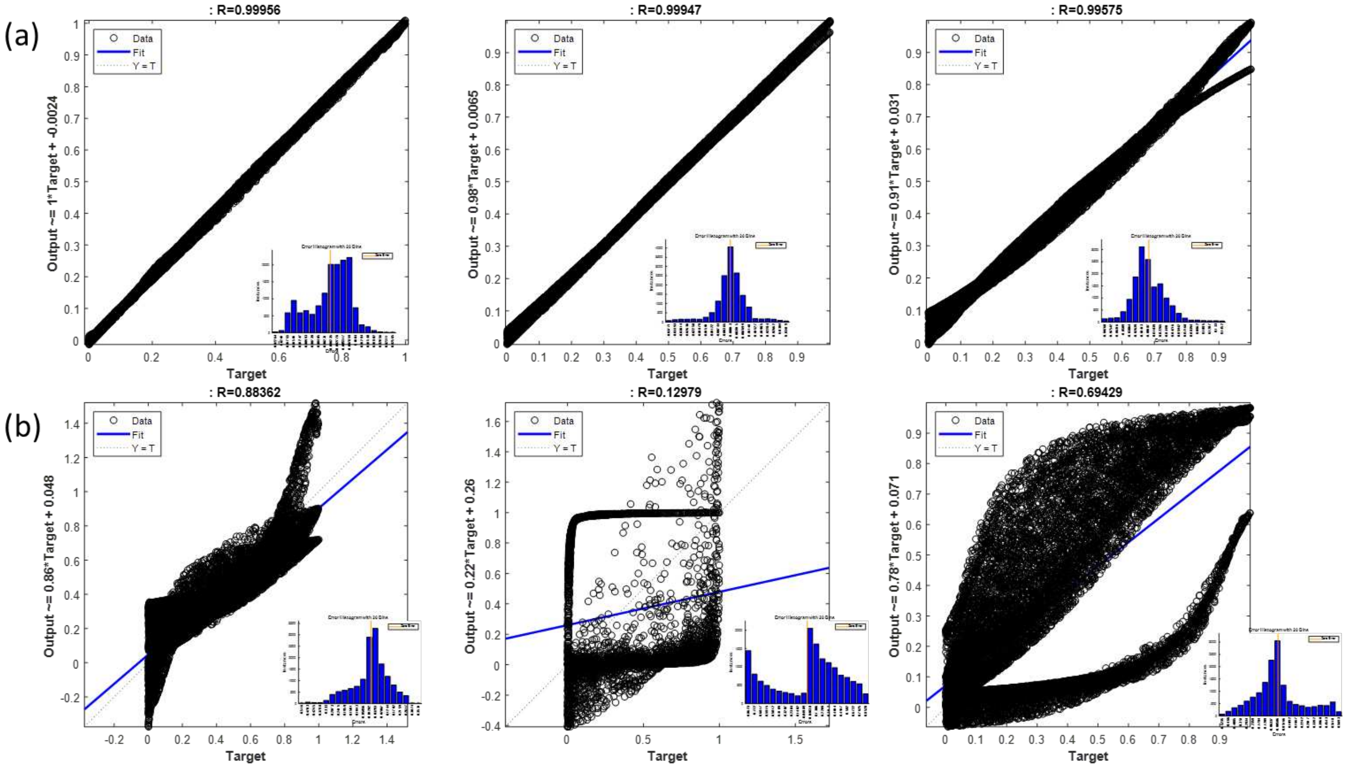

Fig. II-14 Comparison of prediction for ANN No.9 (b) and ANN No.10 (a)

On the one hand, these results were encouraging, but on the other hand the use of two-layer hidden neural networks was not conducive to the robustness of the predictive model or even to the ease of observing the effect of our choices in such networks. It is clear that there was certainly too much weight to optimize in our networks and that we had to find another solution. It was therefore necessary to work on a solution that would limit the number of neurons on the input layer, as the use of spectral data was no longer possible. We did not want to develop a wavelength selection method in the spectral domain and therefore we preferred PCA as a compression method.

II.1.11 Introducing a new spectral representation using PCA

Principal component analysis is the Swiss Army knife of chemometrics. It is applied to a spectral dataset in order to account for all the variances it contains but representing it with a very small number of variables compared to the original. This technique can thus be seen as a filtering method that separates the chemical information in the dataset from the noise. Thus, the transformation of our spectral data and their use for the construction of neural networks will take place as follows:

1. Usual procedure to generate our synthetic spectral dataset (considering different number of elements, different temperatures and electron densities),
2. Splitting of the initial dataset into training (80%) and test (20%) sets,
3. Apply PCA to the training set considering mean-centered data,
4. Selection of a given number of principal component (n_{opt}) to be retained (to be optimized),
5. n_{opt} scores will then be saved for each synthetic sample in the training set. These are the values that will be used as input to the neural network.
6. The spectra of the test set will then be projected onto the n_{opt} principal components n_{opt} giving in turn the n_{opt} scores for each.

We see that such a procedure allows us to drastically reduce the number of input neurons (and thus the total number of weights to be optimized on the network) since we will go from 2048 (i.e. 2048 spectral variables) into n_{opt}. These scores will therefore be used as input to the neural network. On the other hand, we need to optimize the number of principal components. Indeed, a too low number would induce a loss of spectral information from this preprocessing (i.e. compression) step that we would not be able to make up for by learning the network. Too many components would not be welcome either, as only noise could be carried by some of them. As the synthetic spectra consist of 22 elements, it was unlikely that we would be able to build a successful neural network based on less than this number of principal components. We have thus started to build networks that predict only three elements using scaled conjugate gradient backpropagation (*trainscg*), a sigmoid transfer function and a variable number of neurons in the hidden layer from a few to a few dozen. This first experiments showed that the number of components had to be higher than 24 to obtain good prediction results but also that the number of neurons in the hidden layer had to be higher than the number of components (results not shown here). We then extended this research on the basis of these observations while at the same time attempting to increase the number of concentrations to be predicted to 22 by a single network. These results are presented in Table II-14.

Table II-14 Results of using PCA for inputs

Iterations	Input neurons	Hidden neurons	Number of elements to be predicted	MSE	Datasize	R	R for test	R for validation	Noise
4559	24	25	3	6.20E-07	20000	1	1	1	
6960	24	25	8	4.38E-04	20000	0.99532	0.995	0.99504	
6319	24	25	8	1.99E-04	20000	0.99768	0.99778	0.99779	
4754	24	25	10	1.00E-03	20000	0.98727	0.9881	0.98873	
6408	24	30	10	5.22E-04	20000	0.99347	0.99338	0.99355	
10000	24	30	10	3.00E-04	20000	0.99626	0.99818	0.99622	
5570	24	35	10	5.31E-04	20000	0.9934	0.99318	0.9933	
5888	24	35	10	5.43E-04	20000	0.99311	0.99274	0.9927	
5908	24	40	10	4.32E-04	20000	0.99458	0.99434	0.9944	
6137	24	40	10	6.08E-04	20000	0.99237	0.9919	0.9919	
6089	24	50	10	5.93E-04	20000	0.99259	0.99286	0.9921	
9293	24	50	10	2.43E-04	20000	0.99696	0.997	0.9964	
9227	50	50	10	4.75E-05	20000	0.99941	0.9994	0.998	
6394	50	25	10	8.26E-05	20000	0.99896	0.999	0.8329	
4664	50	25	10	1.10E-04	20000	0.99862	0.9986	0.9611(no noise)	0.964
6221	50	50	10	2.14E-04	20000	0.99732	0.99713	0.9972(no noise)	0.9971
1792	80	50	10	6.56E-04	20000	0.99178	0.9909	0.9924	
5519	80	50	10	1.05E-04	20000	0.99868	0.9986	0.9988	
9651	80	50	15	6.18E-05	20000	0.99893	0.9988	0.999	
8626	80	50	15	1.26E-04	20000	0.99783	0.9977	0.9977	
9318	80	50	20	2.56E-04	20000	0.9943	0.9939	0.9946	
10000	80	50	22	2.86E-04	20000	0.99305	0.9926	0.9932	
10000	80	50	22	2.40E-04	20000	0.99417	0.9939	0.9946	
3135	80	30	22	8.70E-04	20000	0.97877	0.9784	0.9795	
6243	80	30	22	6.39E-04	20000	0.98439	0.9837	0.9847	
8902	80	60	22	2.17E-04	20000	0.99475	0.9942	0.9949	
10000	80	60	22	2.42E-04	20000	0.99413	0.9934	0.9941	
8284	80	80	22	2.08E-04	20000	0.99495	0.9941	0.9947	
10000	80	100	22	1.82E-04	20000	0.99563	0.9947	0.9959	
7374	100	60	22	2.31E-04	20000	0.99437	0.9931	0.9943	
10000	100	60	22	1.84E-04	20000	0.99556	0.995	0.9956	

We notice that things change fundamentally with this new concept of compression used before the neural network. We obtain excellent MSE and R values, no matter how many elements are to be predicted. Note that a network consisting of 80 input neurons, i.e. using the scores of the first 80 principal components, and 100 hidden neurons is able to successfully predict the concentrations of the

22 elements. Nevertheless, we wanted to try to restrict the number of hidden neurons to 50 (again to limit the total number of weights to be optimized in the network) while looking at the effect of a larger number of components. The results are presented in the Table II-15.

Table II-15 Results of finding best inputs

Inputs	Neurons	No. elements	MSE	R training	R for test	R for validation
100	50	22	2.67E-04	0.99353	0.99323	0.99371
120			2.04E-04	0.99506	0.99324	0.99513
140			2.31E-04	0.99440	0.99344	0.99488
150			2.30E-04	0.99444	0.99303	0.99504
200			1.48E-04	0.99641	0.99581	0.99753
250			2.69E-04	0.99348	0.99319	0.99500
300			2.34E-04	0.99435	0.99328	0.99656

It is difficult to speak about the significance of the differences observed here and that is why we will favor the lower number of weights in the network, i.e. 100 input neurons and 50 hidden neurons. Under these conditions, we have a very efficient network capable of predicting the concentrations of the 22 elements, independently of the temperature of the plasma and its electron density. However, we should not forget that such a network will have to be applied to real data which will undoubtedly be tainted by a certain level of noise. As a reminder, the previous networks were trained and tested on data with a noise level of 0.1%. It was therefore logical to estimate the influence of the noise level on the performance of the neural network. We then generated synthetic datasets with 8 noise levels ranging from 0.1% to 20%. For each dataset with a given noise level, we developed a principal component analysis to keep only the first 100 principal components. The 100 scores per sample were then used to train 8 different neural networks with 50 hidden neurons to predict the 22 concentrations.

Table II-16 gives the prediction results obtained these three levels of noise. More precisely, all the MSE and R values in this table is an average of three trails per noise level. It is quite natural to see the predictive capabilities of a model decrease with the level of noise. Nevertheless, we must insist here on a certain robustness of the approach since the MSE errors and correlation coefficients remain more than satisfactory with a rather huge noise. This network capability is particularly important for our imaging problem. Indeed, we always want to increase the number of spectra acquired during a hyperspectral imaging experiment and as the total analysis time must be reasonable we often have to limit the acquisition time for each spectrum. In fact, the signal-to-noise ratio of an imaging dataset is quite often limited, hence the importance of a predictive model capable of withstanding lower data quality, which is our case here.

Table II-16 Results of different noise

Inputs	Neurons	Noise	MSE	R	R for test	R for validation
100	50	0.001	2.72E-04	0.99339	0.99280	0.99284
		0.005	3.01E-04	0.99269	0.99185	0.99003
		0.01	4.82E-04	0.98626	0.98661	0.98519
		0.02	5.13E-04	0.98758	0.98150	0.98473
		0.05	5.75E-04	0.98603	0.98415	0.98151
		0.08	8.45E-04	0.97916	0.97869	0.97892
		0.1	8.14E-04	0.98008	0.97570	0.97256
		0.2	1.05E-03	0.97408	0.97003	0.96788

II.1.12 Could we predict the temperature from a spectrum?

Based on the previous good prediction results, we asked ourselves whether we will be able to predict the plasma temperature from a spectrum based on a well-trained neural network. This approach is quite original since such a network, if it exists, could also allow us to generate plasma temperature maps from a hyperspectral dataset. For this purpose, we used our procedure for generating synthetic spectra by mixing 22 elements in random ratios for different temperatures. The usual data spitting has been used in order to obtain the training set, the validation and the test set. Then, different neural networks have been trained to predict this temperature using a variable number of PCA scores (from 100 to 500) or directly from the 2048 initial spectrum values. The prediction results are given in Table II-17.

Table II-17 Predicting only T with 50 hidden neurons

Input neurons	Noise level	Datasize	Hidden neurons	MSE	R
100	0.001	20000	50	0.0026	0.95125
150				0.0016	0.97013
200				0.0021	0.96261
250				0.0018	0.96703
300				0.0034	0.93942
500				0.0026	0.95212
2048				0.0070	0.86241

The first thing that stands out is the fact that a prediction of the temperature seems possible with a certain accuracy. Again, it can be seen that it is better to use the scores coming from PCA than whole the variables in the spectral domain. The best predictions in this case are obtained for a network consisting of 150 input neurons (i.e. using 150 scores of the 150 principal components) and 50 neurons on the hidden layer. Many other attempts were made to reduce the number of hidden neurons and it was finally a network with 10 hidden neurons that allowed us to finalize this task. The results of these last networks are given in Table II-18. Thus, the network containing 100 input neurons and 10 hidden ones gives MSE the value of 9.10^{-4} and a R value around 0.98 which is really efficient.

Table II-18 Predicting only T with 10 hidden neurons

Input neurons	Noise level	Datasize	Hidden neurons	MSE	R
50	0.001	20000	10	0.0043	0.91807
100				0.0009	0.98311
150				0.0024	0.95685
250				0.0024	0.95743

By way of illustration, Fig. II-15 shows the regression plot (i.e. target vs predicted value) of the best network. We note an excellent linearity of the relationship on the three datasets and homogeneous dispersion for the different temperature levels. It may be surprising to see values between 0 and 1 in these representations but it was necessary to normalize the temperatures before training the network in order to be consistent with the range of the network transfer functions. Temperatures that were initially between 6000K and 10000K were then represented by values between 0.1 and 1 after this normalization. This does not, of course, detract from the quality of the predictions presented in this section.

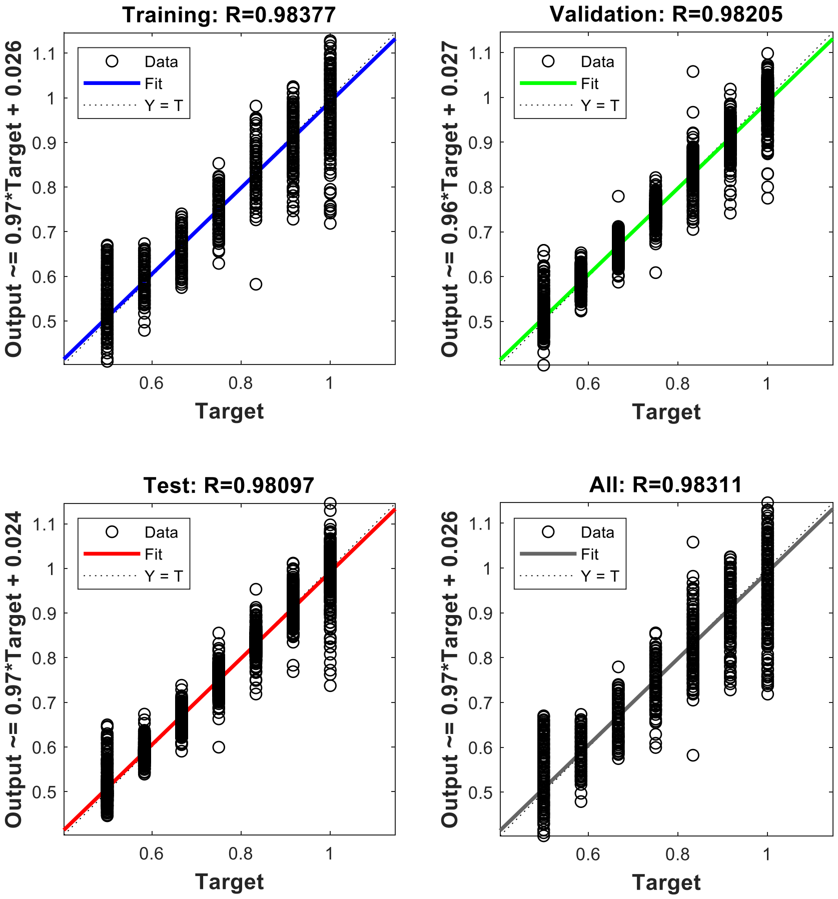

Fig. II-15 Regression plot of the best results of predicting only T

II.1.13 Could we predict the electron density of the plasma from a spectrum?

In view of the good results obtained on the temperature prediction, it was logical to try to do the same with the electron density. As before, we generated our synthetic spectral data by keeping the type of neural network and its learning algorithm. The use of PCA has of course been retained. A preliminary normalization of the densities was also necessary since we considered the values 5×10^{16}, 1×10^{17}, 5×10^{17}, which could not be directly considered during the training of the network. Following this normalization, the lowest electron density was thus associated with the value 0.1 and the highest with 1. We then started with a layer of 100 input neurons for the network, i.e. by considering 100 principal components. As usual, we also studied the influence of the number of neurons on the hidden layer. The prediction results obtained are presented in the Table II-19.

Table II-19 Results of predict only Ne with 100 pcs

Inputs	Neurons	Output	Datasize	MSE	R
100	2	1	20000	0.0325	0.89379
	5			0.0322	0.89603
	10			0.0323	0.89483
	20			0.0378	0.87617
	50			0.0380	0.87530
	80			0.0418	0.86250
	100			0.0376	0.87656

The first remark we can make is that the quality of the prediction is well below that of the temperature with higher MSE values and much lower R values. It thus seems more difficult to predict the electron density but we cannot really be categorical as we have only used three levels of density here, which does not necessarily help. If we now look at the number of neurons on the hidden layer, we see that the errors are all very close but the lowest are nevertheless obtained with less than 10 hidden neurons. Assuming that there is no significant difference between the networks using 2, 5 or 10, it is logical to choose the lowest number of hidden neurons, i.e. 2. As an illustration, Fig. II-16 shows the prediction results for a network using 100 input neurons and 1 output neuron.

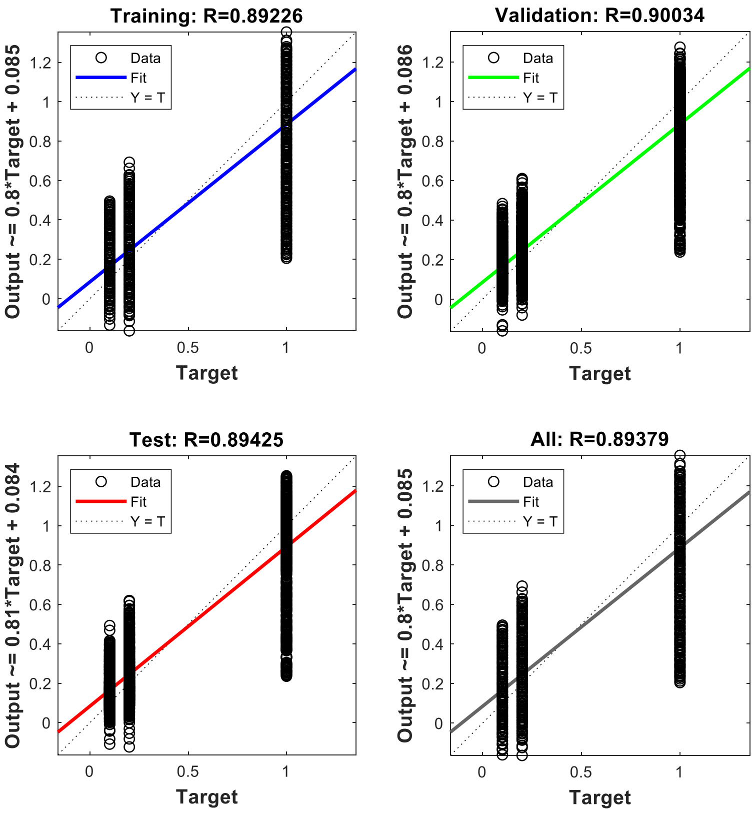

Fig. II-16 Regression plot of the best results of predicting of Ne

II.1.14 Could we finally predict everything?

In the previous sections, we have seen that the use of principal component analysis has been determinant for the training and prediction of neural networks. We were able to predict first the concentrations of the 22 elements with a single network, and then with two other networks to predict separately the temperature of the plasma and its density on the basis of LIBS spectral information. The objective of this new part was therefore to see if we would be able to predict not only the concentrations but also the temperature and the electron density of the plasma by a single neural network. As usual, the number of input neurons (and therefore the number of principal components) and the number of hidden neurons had to be optimized. As it was necessary to start with a first hypothesis, we decided to fix the number of principal components at 100 since we had seen in the previous sections that this allowed to potentially predict all 22 elements. Thus, Table II-20 gives the prediction results considering a variable number of hidden neurons.

Table II-20 Influence of the hidden neurons number on the prediction results

Input neurons	Datasize	Output neurons	Hidden neurons	MSE	R	R for test
100	20000	24 (22 elements, T, Ne)	20	4.50E-03	0.95526	0.95569
			30	1.63E-03	0.98412	0.98344
			40	1.13E-03	0.98922	0.98686
			50	1.03E-03	0.98991	0.98856
			80	2.00E-03	0.98054	0.98029
			100	1.04E-03	0.98984	0.98814
			120	1.11E-03	0.98929	0.98678
			150	1.92E-03	0.98109	0.98008

As we can see we obtain quite satisfactory results whatever the number of hidden neurons. Even if it is difficult to say if all these differences are significant, we have decided to use 50 hidden neurons which has the lowest MSE value of 1.03E-03. We could then go back to optimize the number of input neurons that we had set a priori in the previous step. The prediction results are given in Table II-21 Table II-21. As we can see, a network using the scores of 120 principal components with 50 hidden neurons allows us to have the lowest error. We can therefore say that with our approach, we are able to predict the concentration of the 22 elements as well as the temperature of the plasma or its electronic density by a single predictive model, which is very interesting.

Table II-21 Influence of the number of principal components

Input neurons	Datasize	Output neurons	Hidden neurons	MSE	R	R for test
100	20000	24	50	1.04E-03	0.98984	0.98814
120		24		7.70E-04	0.99254	0.98780
150		24		1.10E-03	0.98912	0.98819
200		24		9.12E-04	0.99115	0.98960

II.1.15 Last but not least, a pitfall but…

Research on a complex subject is never a smooth river and just when we think we have reached our goal, a new problem often arises that we need to address. A discussion with our collaborators first revealed that the list of 22 elements we had been using from the beginning was not 100% compatible with all the elements of interest that would potentially be present in the mineral sample we were to analyze at the end of the modelling part. We therefore removed the elements As, Au and Sr and added the elements Be, Ce, Eu, Ge and Y. So now, we had a list of 24 elements. Of course, this should not have been a problem for the previous method we had optimized, except for the fact that it was necessary to redo a new PCA analysis and then train a new network with these 24 new elements. However, during this same discussion, it appeared that we had not seen a much more significant problem. Indeed, the intensities of a LIBS spectrum are naturally dependent on the laser power used. Thus, the use of two different LIBS instruments or even a single one used to analyze a sample over two different time periods could well present a different overall intensity while from a chemical point of view we still had the same elemental concentrations under these different conditions. This made normalization of the spectra inevitable in order to get rid of the potential global intensity variations in the LIBS spectrum. The only problem was that the good predictive networks we had obtained were based on a neural network using the scores from the PCA that had been done on non-nominalized data. It was therefore necessary to verify that this PCA/ANN approach was still valid on normalized data, which we did by developing a network with 100 input neurons and 50 hidden neurons to finally obtain an RMSE value of 0.0293 for the validation set and a correlation coefficient of 0.9773. It was obvious that we had lost the predictive potential presented in the previous sections from the PCA on raw data. Fig. II-17 shows how the addition of this normalization has completely disrupted the training of the ANN model.

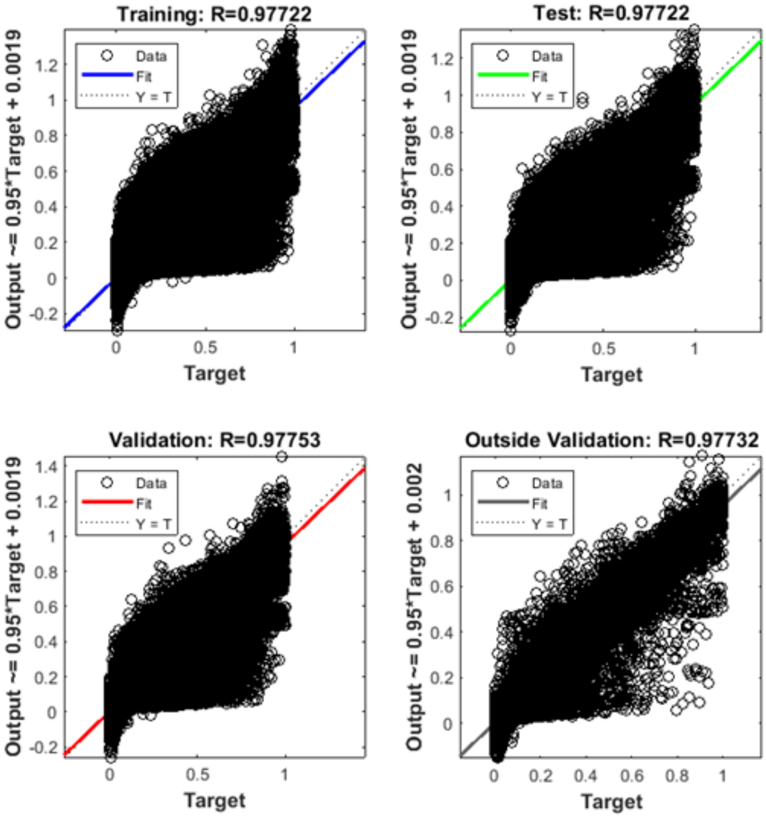

Fig. II-17 Regression plot of the ANN using PCA score with spectral normalization

We have tried to optimize as usual in this work many parameters of the network such as the number of principal components, the global architecture of the network, the transfer functions and the learning function but this did not change anything to the situation (results not presented in the manuscript). Reluctantly we decided to abandon the networks using PCA scores and return to the classical networks exploiting directly the libs spectrum. We had seen before that we could use normalized spectral data to predict the concentrations of some elements even if everything was not perfect. In order to simplify the task of training the neural network as much as possible, we decided to predict only one element at a time. This would undoubtedly require a lot of work as we would have to build 24 different networks for the 24 elements but this option deserves to be tested. As usual, we generated our synthetic dataset based on the pure spectra of the 24 elements considering different temperatures and electron densities. All spectra have been normalized by the maximum value before being used in a network. Of course, we spent a lot of time on the usual optimizations to choose a unique number of hidden neurons equal to 100 for the 24 neural networks. This optimization phase also showed that a much larger number of epochs were needed as well as an increased number of validation checks. Table II-24 gives the predictive capabilities of the 24 neural networks thus optimized.

Table II-22 Results of 24 ANNs using normalized spectral data

Element	RMSE training	R training	RMSE validation	R validation
Ag	0.0213	0.9900	0.0317	0.9770
Al	0.0219	0.9896	0.0274	0.9820
Be	0.0382	0.9625	0.0391	0.9636
Ca	0.0189	0.9944	0.0221	0.9879
Ce	0.0400	0.9593	0.0431	0.9499
Cr	0.0208	0.9910	0.0216	0.9875
Cu	0.0147	0.9958	0.0184	0.9920
Eu	0.0358	0.9714	0.0399	0.9563
Fe	0.0280	0.9819	0.0298	0.9775
Ga	0.0203	0.9903	0.0248	0.9838
Ge	0.0393	0.9626	0.0395	0.9526
La	0.0373	0.9636	0.0411	0.9565
Mg	0.0194	0.9918	0.0215	0.9892
Mn	0.0276	0.9812	0.0289	0.9759
Mo	0.0208	0.9907	0.0255	0.9823
Na	0.3700	0.9655	0.0400	0.9560
Ni	0.0191	0.9939	0.0260	0.9814
Pb	0.0366	0.9727	0.0320	0.9717
Si	0.0225	0.9880	0.0301	0.9774
Ti	0.0288	0.9902	0.0297	0.9769
U	0.0249	0.9860	0.0286	0.9776
Y	0.0204	0.9914	0.0244	0.9850
Zn	0.0301	0.9797	0.0336	0.9670
Zr	0.0168	0.9942	0.0214	0.9889

We quickly see that we have good results on all the elements and that this option of trying to simplify the output layer of the network was a worthwhile option. We have thus shown the feasibility of such an approach for the quantification of elements independently of the plasma temperature and its electron density. It is true that you may rightly ask why this option was not considered earlier in this work. This is because we were focused on providing a single network that would be easier to use for prediction purposes. The time spent optimizing these numerous networks was not wasted as it also allowed us to observe different behaviors of the neural networks when faced with LIBS data in different forms, which is equally valuable.

II.2. Applying our ANN approach for the exploration of a complex mineral sample

II.2.1 Context and description of the considered mineral sample

As explained in the previous section, it is not possible to correct for variations in plasma temperature and electron density for all the spectra in a LIBS imaging dataset, which today often consists of several million spectra. The generation of chemical maps is therefore based on the integration of characteristic emission lines of an element of interest, neglecting these variations so that we cannot know them on each pixel. This is not a fundamental problem if we are studying homogeneous materials, but spectroscopic imaging is primarily used to investigate local heterogeneities in a sample at the micron scale over large areas. The aim of this section is to show how we can use our previous networks trained on synthetic data to predict elemental contributions in a naturally heterogeneous matrix i.e. a mineral for which it is known that variations in plasma parameters are necessarily observed. Since the beginning of the thesis, a rock sample had been selected by our collaborators (Vincent Motto-Ros and Cécile Fabre) and we planned to analyze it with our approach at the end of the modelling phase. Our first aim was to demonstrate the feasibility of the concept and it would have been unreasonable to consider all the elements of the periodic table, hence the short list of 24 elements in line with the supposed presence of these elements in the selected rock. Fig. II-18 provides an optical image of the considered sample. It is approximately 3.4 cm long by 2.8 cm wide and we can easily see the great heterogeneity of the mineral phases. This rock sample was previously embedded in resin and polished prior to LIBS analysis.

Fig. II-18 The optical image of the mineral sample

It took only a few hours to acquire 2.38 million LIBS spectra over a spectral range from 280 to 369 nm (and a total of 2048 wavelengths) with a spatial resolution of 20 microns. The cube of LIBS hyperspectral data that we manipulated had the size 1400 × 1700 × 2048.

In the classical implementation of a LIBS imaging experiment, we usually select a rectangular area around the sample, which is then systematically analyzed along lines during the spectroscopic measurement. Of course, the sample studied here is not rectangular and many of the spectra acquired correspond to the resin and not to the rock sample. It is therefore necessary to localize the spectra in the dataset which only contains information about the rock. This may seem trivial but it has been shown many times in spectroscopic imaging that this pixel selection is necessary at the risk of completely biasing the chemometric exploration. We therefore used a Matlab Toolbox (*imageSegementer*) to generate a so-called mask that allowed us to automatically define which spectra we should keep or which spectra of the resin we should remove from the hyperspectral dataset. This mask is shown inFig. II-19 , the yellow area representing all the pixels associated with the rock and therefore the spectra that we will consider for the rest of the calculations.

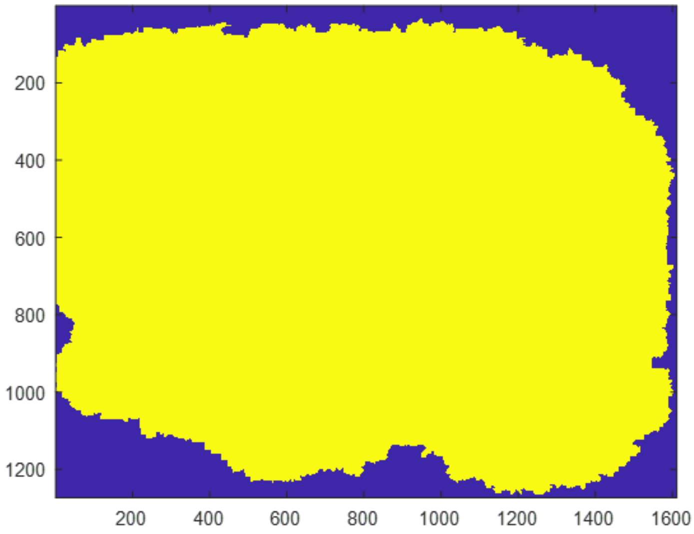

Fig. II-19 Mask generated by the Matlab toolbox, imageSegementer

Comparing this mask with the optical image, it can be seen that the left side of the sample will not be considered because the spectra are in poor quality.

II.2.2 Applying our ANN models to the rock sample

The objective was now to use the latest networks developed in section II-1.15 to generate elemental maps. The latter having been trained on normalized data we had of course to do so for these spectral data. At first glance, it seemed obvious that all that remained was to use each normalized spectrum (included in the mask) as an input to one of the trained networks for a given element to generate the corresponding chemical map. This was a risky bet in the sense that even if our collaborators, experts in LIBS and geology, had proposed a very relevant list of elements, no one could ensure that this list was exhaustive and that the networks had been trained with all the elements likely to be encountered in the sample. In other words, a direct use of the network is not possible at this stage because nobody can say whether each spectrum of the mask contains only elements of this list. So, if we have for example a spectrum that contains an element that is not in the list, its spectrum will be slightly different from the spectra contained in our synthetic spectra database with the consequence of disturbing the prediction of the concentration of the other elements if we force ourselves to use it. We have to find a solution to this problem because we have no choice but to train our network on synthetic spectra with a limited list of elements.

The trick comes from a basic principle in chemometrics. If you have developed a predictive model from a given calibration set of spectra, the future spectra used in the prediction step should be contained within the subspace defined by them. This is exactly the procedure used to detect outliers (i.e. spectra that must be discarded because they are not consistent with the training set). We are going to go even further, because a PCA will be used to filter the rock spectra so that they can be consistent with all the synthetic spectra contained in the training set of the ANNs. In a way, we will remove from the rock spectra all the elemental contributions that are not in the list of 24 elements.

The procedure is therefore as follows:

1) Development of a principal component analysis on the synthetic dataset,
2) Selection of an optimum number of n_{opt} components to best describe the subspace of this first dataset.
3) Projection of the rock sample spectra onto the n_{opt} principal components to obtain n_{opt} scores for each.
4) Reconstruction of each rock spectrum through a linear combination of its n_{opt} scores and the n_{opt} principal components to obtain filtered spectra.
5) Use of the filtered spectra as input of the previously trained ANNs.

An important point was to find the optimum number of principal components n_{opt}. We therefore simply applied this filtering procedure to the entire rock dataset for increasing values of n_{opt} up to 50. For each n_{opt} value, we then compared the corrected spectra to the original rock spectra by simply calculating the difference, which we then squared and summed to obtain sum of squared differences (SSD). The

Fig. II-20 shows the evolution of the SSD value as a function of the number of principal components used during the filtering.

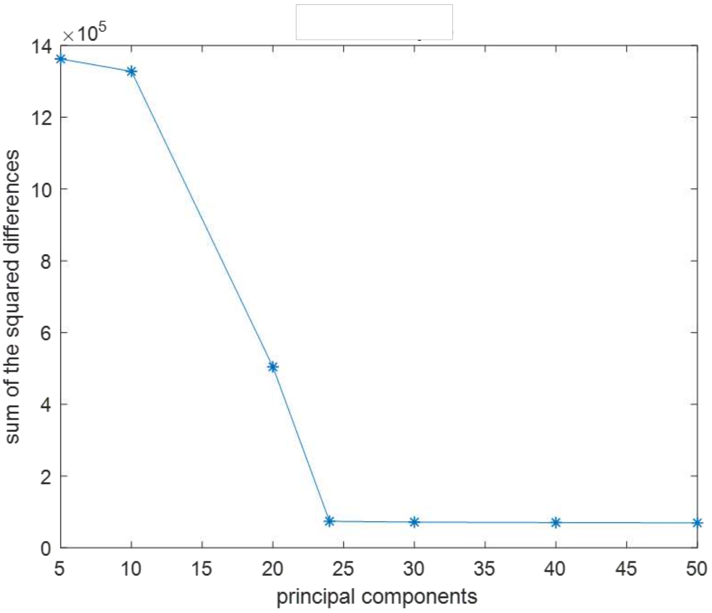

Fig. II-20 Finding the optimal number of components in the filtering process.

In view of this analysis, 24 principal components seemed to be sufficient to filter the spectra of the rock sample. These corrected spectra could now be used as input to our trained neural networks to predict the quantity of all the element of interest. Before generating elementary distribution maps, we thought it was important to take a closer look at the range of values predicted by the neural networks for each of the elements. The minimum and maximum predicted values obtained over the entire sample area for each of the elements are given in Table II-23 Table II-23. The percentage of predicted values in the interval from 0 to 1 is also given for each element. As a reminder, our neural networks have been trained to predict the relative quantities of one element with respect to another. This value must therefore naturally be between 0 and 1. We quickly notice that all these predictions are not perfect because negative values are present. We should not be too harsh either as the minimums in question are often very close to zero. Furthermore, we must not forget that there is an imprecision in our models, particularly for extremely low or even zero concentrations for a given pixel. This is certainly the case for elements such as Ag, Be, Cu, Ga, Mg, Mn, Zn and Zr for this specific sample. Fig. II-21 to Fig. II-27show a comparison of elemental maps obtained through neural networks and the maps of the same elements obtained with the classical method of integration using a specific emission line. It is true that we cannot normally make an absolute comparison of these pairs of maps because we have trained our networks to predict the percentages of an element. Ideally, we would have obtained other concentration maps of each element from a reference method from which we could have obtained relative reference maps.

Table II-23 Range of values predicted by neural networks for each element

Element	Min. predicted value	Max. predicted value	Percentage of predicted values between values 0 and 1
Ag	-0.0128	0.0160	11.95%
Al	-0.0384	0.3034	88.67%
Be	-0.0035	0.0040	40.53%
Ca	-0.0713	0.2594	46.90%
Ce	0.1696	0.5080	100.00%
Cr	0.0058	0.1090	100.00%
Cu	-0.0081	0.0194	52.11%
Eu	0.0088	0.2154	100.00%
Fe	0.0255	0.4856	100.00%
Ga	-0.0100	0.0258	69.48%
Ge	-0.0058	0.0582	99.95%
La	-0.0281	0.4056	99.98%
Mg	-0.0358	0.0228	70.90%
Mn	-0.0085	0.0531	54.66%
Mo	0.0050	0.2302	100.00%
Na	-0.0143	0.0707	99.94%
Ni	-0.0320	0.1636	72.68%
Pb	0.0675	0.2129	100.00%
Si	0.0034	0.6663	100.00%
Ti	-0.0096	0.2143	96.73%
U	-0.0065	0.0698	99.81%
Y	-0.0014	0.1432	99.72%
Zn	-0.1682	0.0575	2.04%
Zr	-0.0277	0.1248	7.21%

Having said that, we will still try to compare maps on these figures with some caution. In order not to be misled by the images, it is first important to understand how the color scale is generated. For example, for a given image, the dark red color corresponds to the highest value and the dark blue color the lowest. As an example, if we look at the Fe map generated from ANN results (Fig. II-22), we can see that there are many green areas which correspond to a predicted value of about 0.25 (i.e. 25%). If the maximum of the color scale is about 0.48, it means that there are pixels with this value effectively present in the map but they are certainly few in number hence the feeling of not seeing any on this map. Even if nothing can prove our claims at this date, the areas where an element is potentially present seem to be more homogeneous when the ANN approach is used compared to the signal integration method as for example for the elements Al, Fe or Mg. Similarly, we obtain very different maps for the elements Ca, Ce, Cr, Cu, La, Y and Zr. So it seems that we see more with our ANN approach, but all this needs to be verified of course.

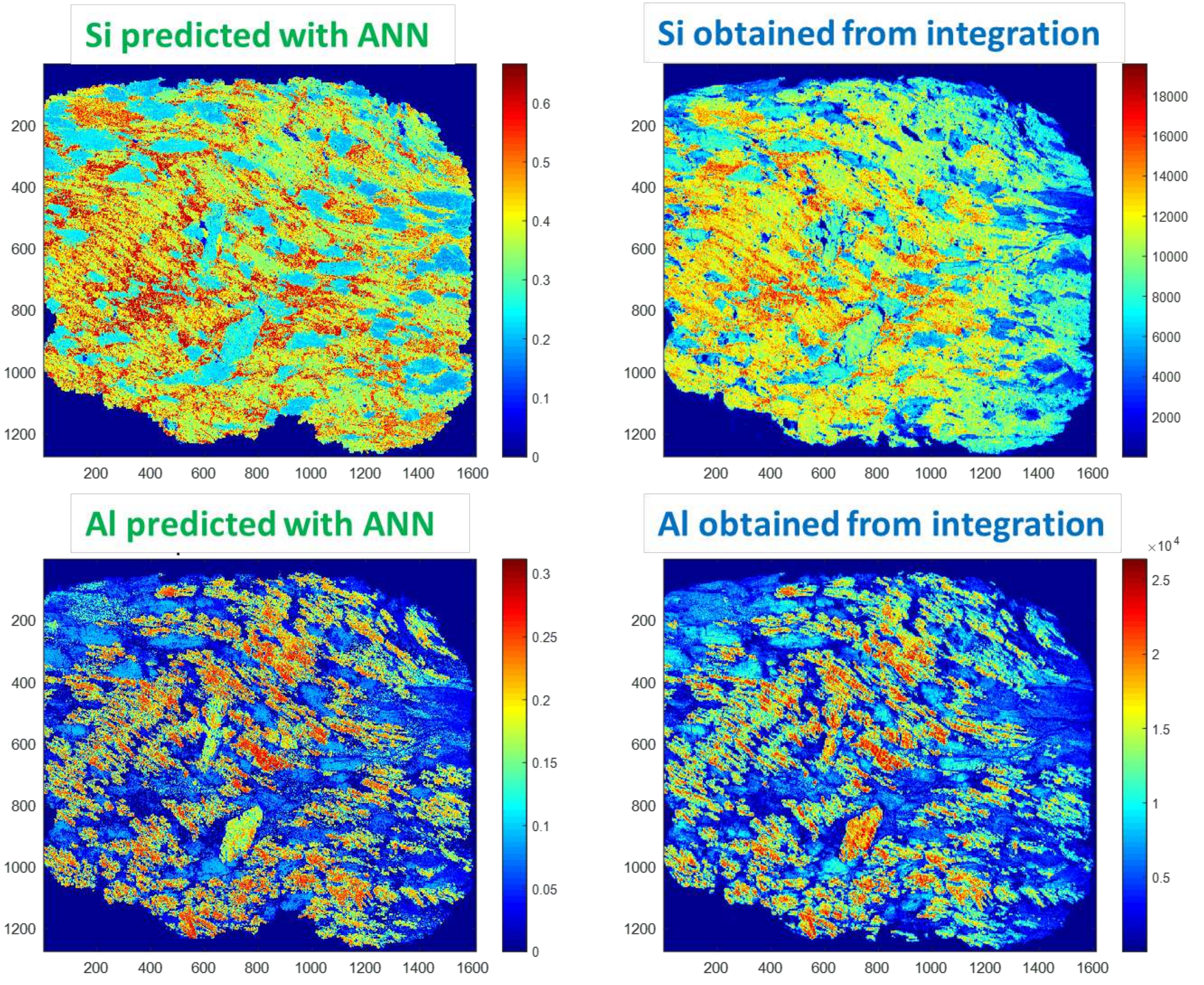

Fig. II-21 Comparison of elemental maps generated with ANN and the classical signal integration method (Si and Al)

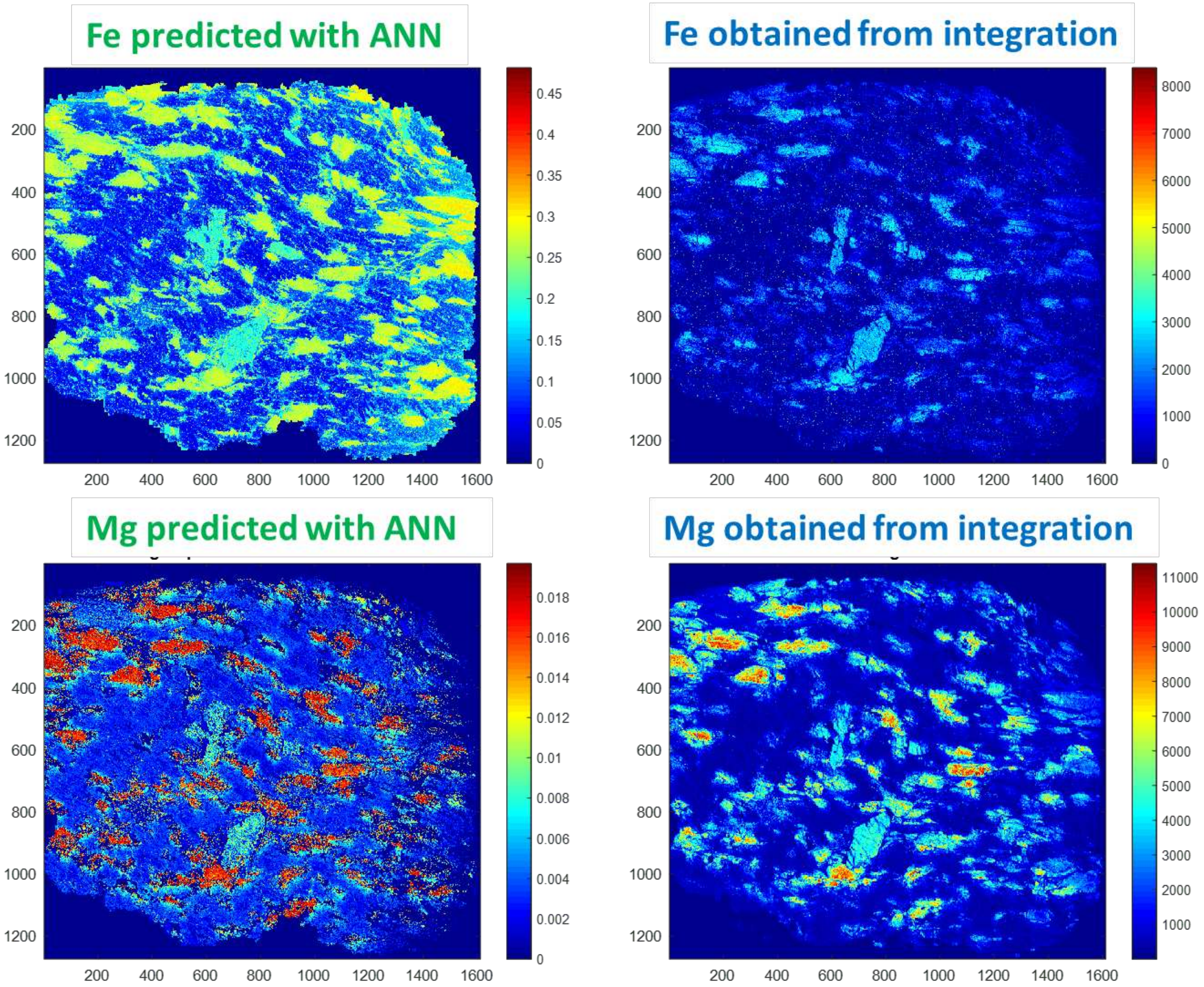

Fe predicted with ANN

Fe obtained from integration

Mg predicted with ANN

Mg obtained from integration

Fig. II-22 Comparison of elemental maps generated with ANN and the classical signal integration method (Fe and Mg)

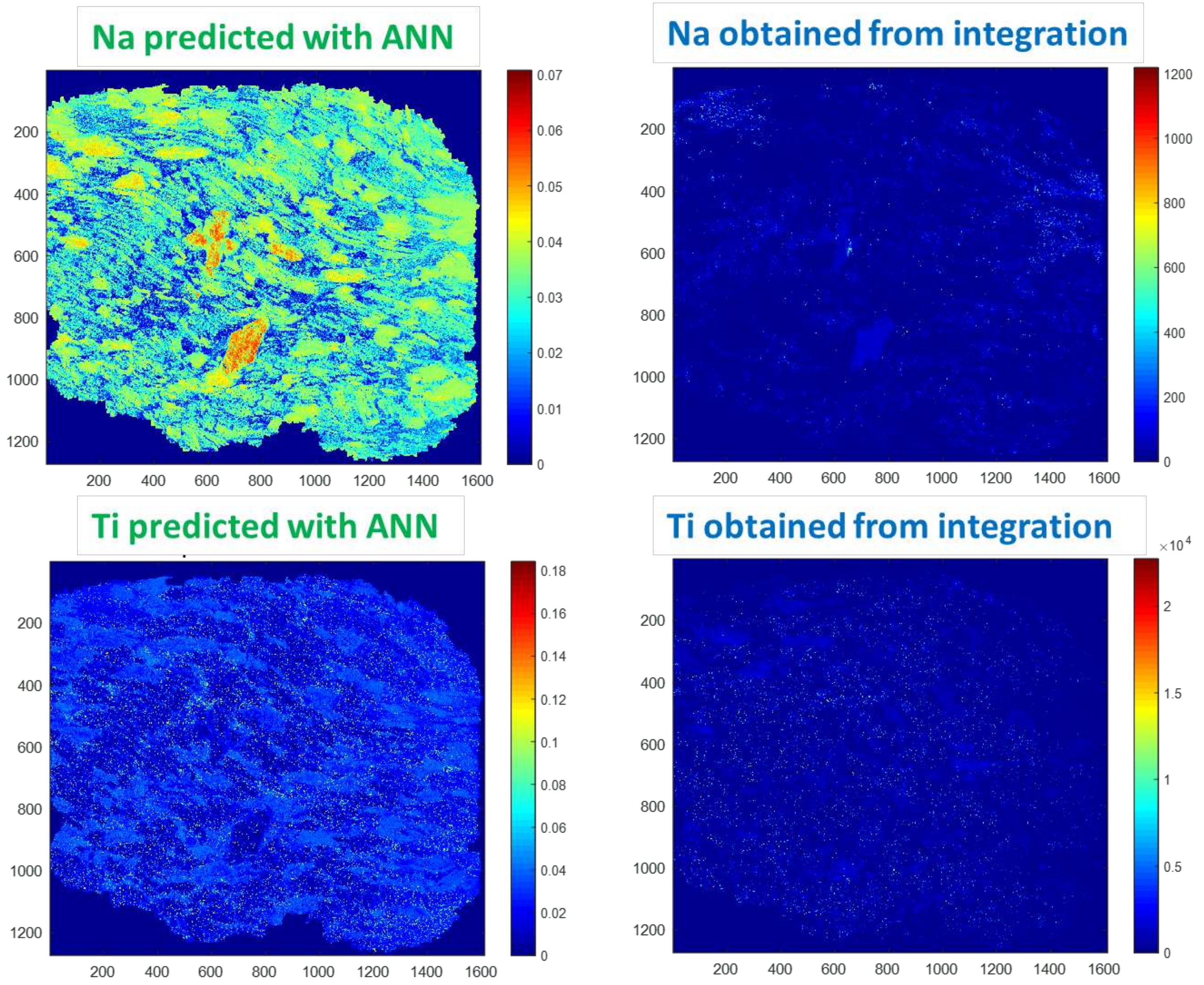

Fig. II-23 Comparison of elemental maps generated with ANN and the classical signal integration method (Na and Ti)

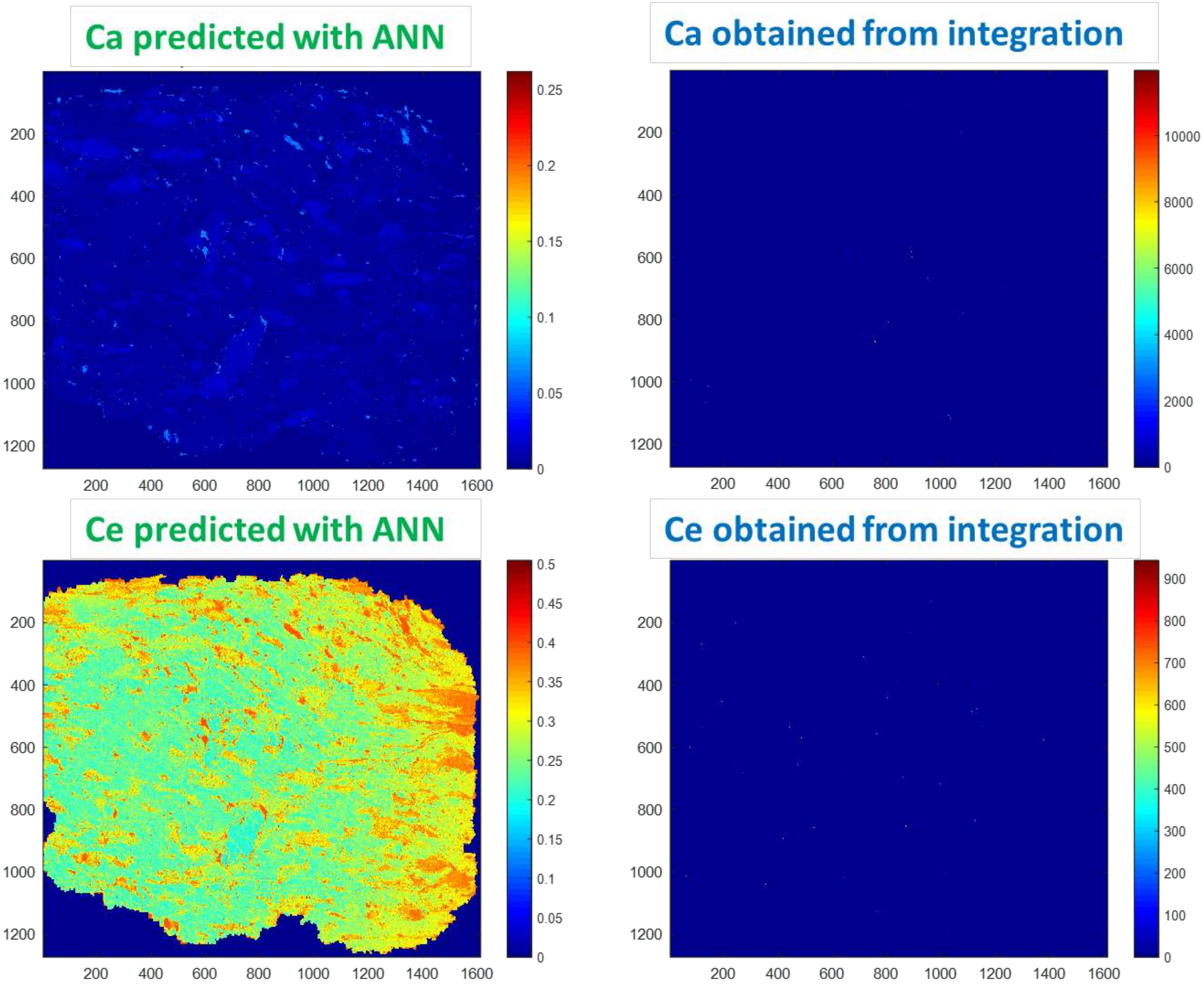

Fig. II-24 Comparison of elemental maps generated with ANN and the classical signal integration method (Ca and Ce)

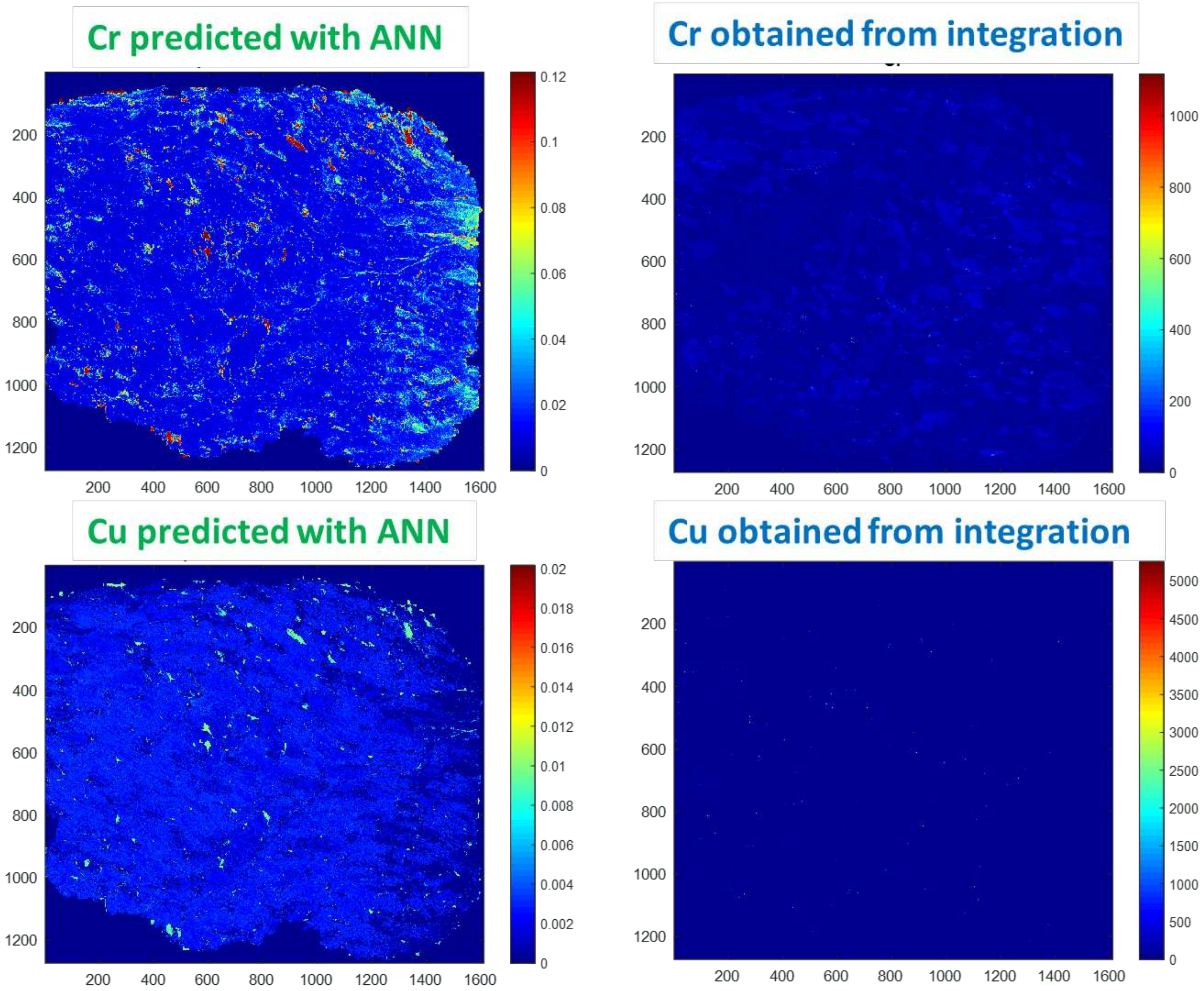

Cr predicted with ANN

Cr obtained from integration

Cu predicted with ANN

Cu obtained from integration

Fig. II-25 Comparison of elemental maps generated with ANN and the classical signal integration method (Cr and Cu)

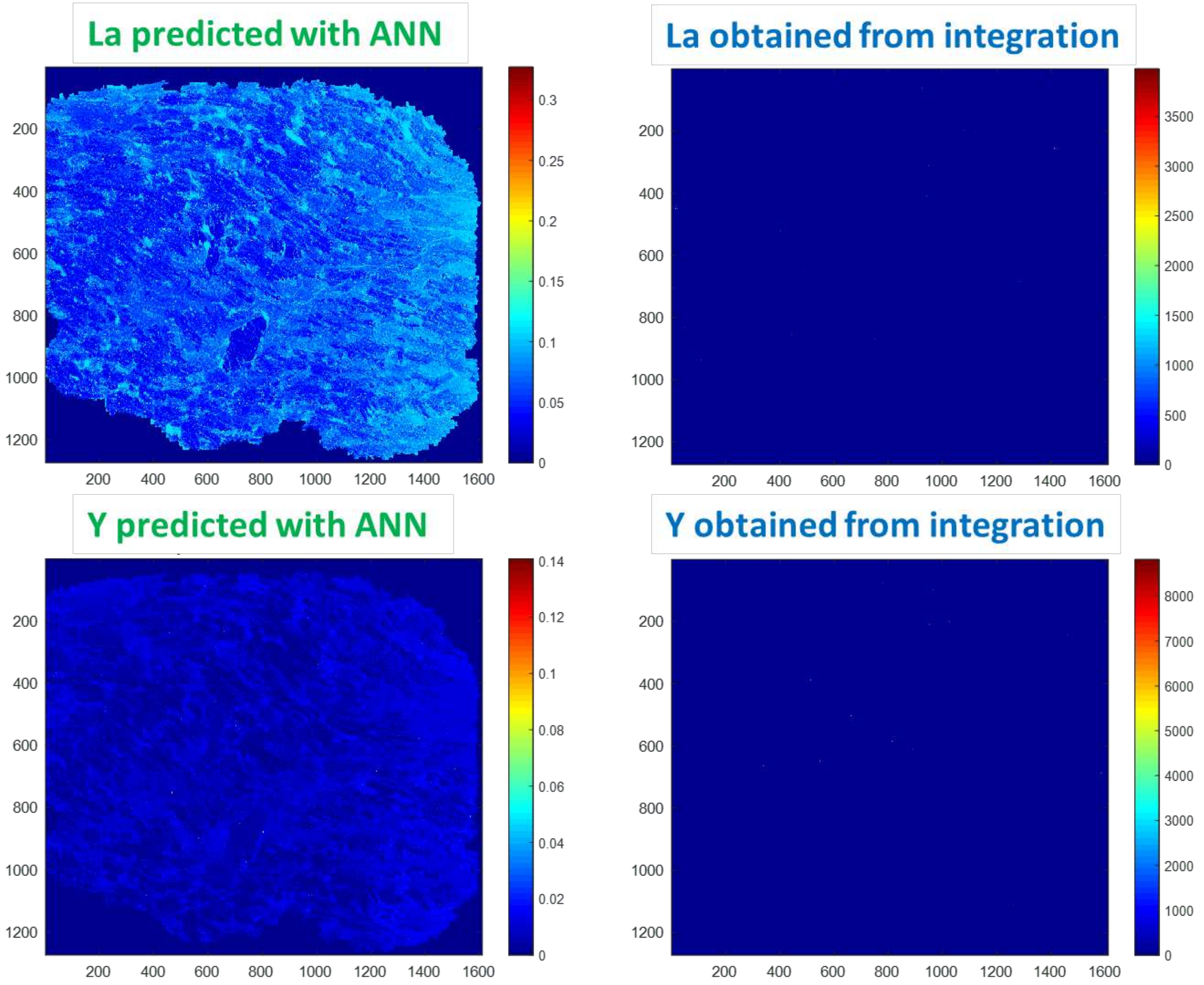

La predicted with ANN

La obtained from integration

Y predicted with ANN

Y obtained from integration

Fig. II-26 Comparison of elemental maps generated with ANN and the classical signal integration method (La and Y)

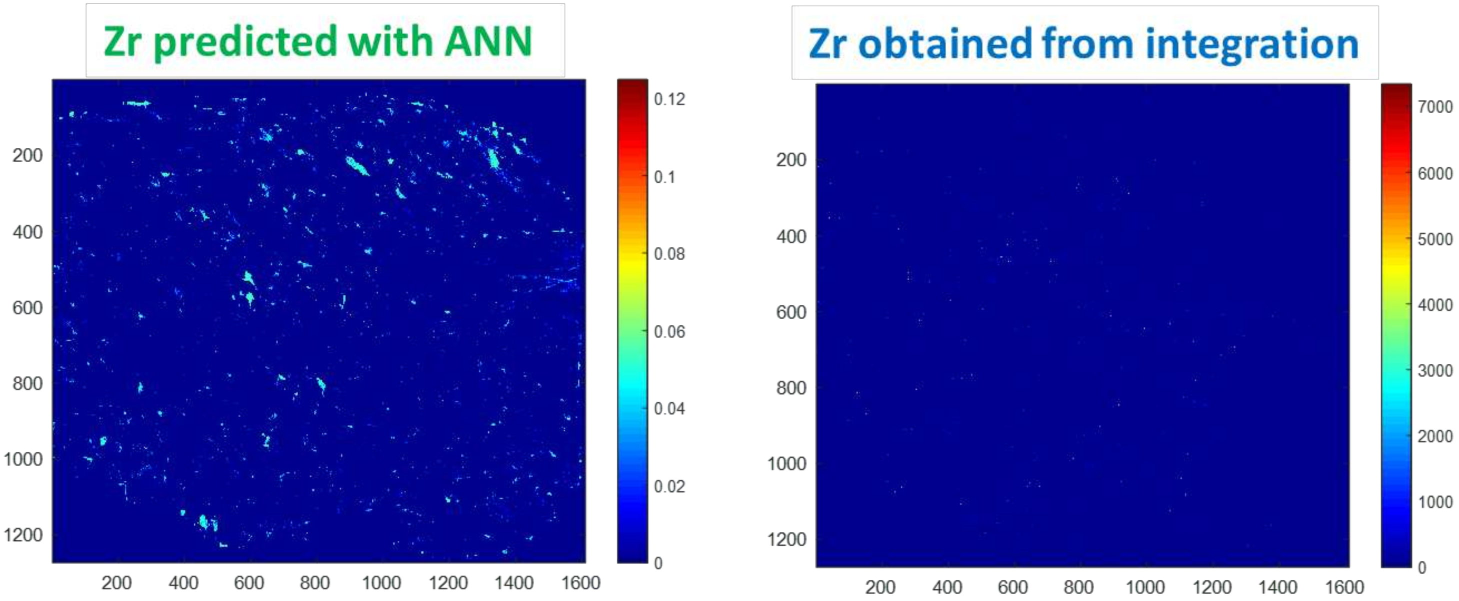

Zr predicted with ANN

Zr obtained from integration

Fig. II-27 Comparison of elemental maps generated with ANN and the classical signal integration method (Zr)

II.3. Conclusion and perspectives

The objective of this research was to study the feasibility of a robust quantitative LIBS imaging analysis in the face of variations in plasma temperature and electron density. Indeed, the natural heterogeneity of a sample means that these two parameters are undeniably not constant over its entire surface, with repercussions on the intensities of the emission lines of its constitutive elements. In the context of imaging, we produce astronomical quantities of spectra today and it is impossible for many reasons to know these parameters for each pixel. The correction of the intensities of the acquired spectra on the basis of these parameters is therefore not possible. The originality of the work in this thesis was to propose the construction of a quantitative predictive model based on spectra with controlled and known variations of the plasma electron density and temperature. It is obvious that in these conditions we would have to use simulated spectra to build this model. It is true that this was a very risky gamble as it is not an ideal situation from a chemometric point of view, but we did not really have any alternatives. Based on the hypothesis of strong non-linearity between the spectra and the concentrations to be predicted, we decided to use neural networks which are known for their good ability to model under these difficult conditions. We also made this choice because we knew that we would not have any problem concerning the number of spectra available to build our model since they were simulated. To be honest, we did not expect to spend so much time on neural network optimization at the beginning of the thesis. The complexity of the data structure required a lot of optimizations concerning the architecture of the network, its training and the preprocessing of the spectral data as we have seen. The use of the final networks trained on synthetic data even had to be redesigned to be usable on our real data as we saw in the previous section. In view of these results, we can say that we have demonstrated a certain potential for this analysis concept but there are undeniably things to be done before it becomes a real tool for quantitative characterization in LIBS imaging. It is in this sense that we now present some perspectives of this work in order to converge towards this goal. To begin with, the simulated spectra should eventually take into account the phenomenon of self-absorption which is very often observed in LIBS spectra. It will also be necessary to see the influence of wavelength shifts and why not make the model robust to this perturbation. We will also have to work on the establishment of a criterion which authorizes us or not to use a neural network on a given real spectrum. Indeed, it is obvious that spectra with a low overall intensity (and therefore relatively high noise) are problematic. We also observed in this work that it was very inconvenient not to have a chemical map of the proportions of the elements from a reference method for a final validation of the concept. We still have to find one, although we know that this will be very complicated. Finally, we have seen that the networks used in this thesis have classical architectures that we have known in chemometrics for decades. For the record, these same neural are now called shallow neural networks. They are so called to differentiate them from deep neural networks which have been developed recently, which demonstrate formidable predictive capacity under very specific conditions. These neural networks are deep because they have a very large number of hidden layers with particular architectures accompanied by learning functions adapted to these new characteristics. It would therefore be interesting to see if we could use such a network to simultaneously predict all the concentrations of the elements of interest from the LIBS spectrum.

Chapter III

Finding exotic pixels in big LIBS imaging datasets

III. FINDING EXOTIC PIXELS IN BIG LIBS IMAGING DATASETS

III.1. Introduction

Laser-induced breakdown spectroscopy (LIBS) imaging is actually becoming an essential tool to characterize complex samples in many scientific domains [196–200]. As we have seen in previous sections, in this spectroscopic technique, a pulse laser beam focused on the sample surface generates a plasma from a small amount of vaporized material. Due to the electronic relaxation of excited atoms and ions, an emission spectrum characteristic of the elemental composition of the sample can be acquired using an optical spectrometer. In LIBS imaging experiments, the sample surface is explored in a raster scanning mode (i.e. acquisition of one spectrum for each spatial position of a predefined grid) covering the region of interest. An elemental image can then be generated from the acquired dataset using a simple signal integration of a given emission line. The richness of this imaging approach lies in its many advantages that cannot be observed simultaneously in any other spectroscopic technique. Indeed, LIBS imaging has multi-elemental capabilities, a high acquisition rate (≥100 spectra/s), full compatibility with optical microscopy and ease of use on samples without almost any size restriction (up to several tens of cm²), all under atmospheric conditions. On top of that, this technique has a high field of view and a spatial resolution around 10 µm coupled with a limit of detection in the order of weight ppm. It is thus very convenient to explore a sample at the micronic scale by acquiring several million spectra in just hours. It is also very interesting to look at the evolution of LIBS imaging over time, which is well illustrated in Fig. III-1. We observe here a real explosion of the number of pixels on a very limited time scale, roughly by a factor of 10 every 2 years since the 2010s. More precisely, this figure presents the work of Motto-Ros *et al.* on the detection of nanoparticles in the kidney [201]. This evolution is of course explained by regular instrumental developments allowing the acquisition of more and more spectra in a limited time but without compromising their quality. In a way we can say that everything is going well with regard to the acquisition of spectral data in LIBS imaging. Concerning data analysis in LIBS, we see today big differences between the two frameworks of bulk analysis and imaging. Indeed, researchers have quickly learned that multivariate data analysis could bring valuable tools for qualitative and quantitative explorations of samples at the bulk level, for instance by developing regression or classification models as we have seen in chapter one.

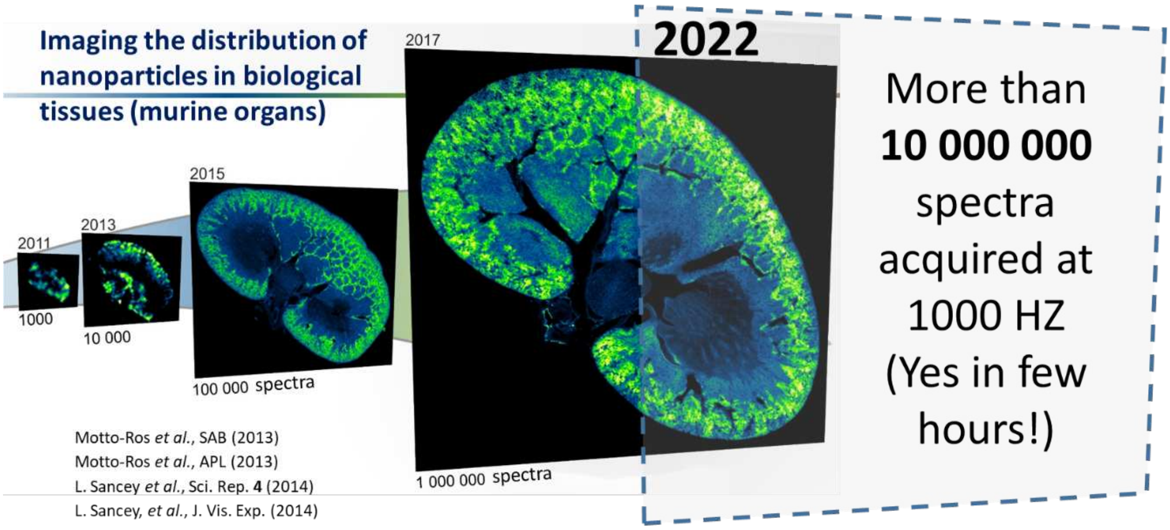

Fig. III-1 The evolution of LIBS imaging

At the imaging level, there is a relatively limited number of papers dealing with the use of multivariate data analysis in the LIBS community. Indeed, elemental images are, in general, generated from single emission wavelengths, even though the whole spectral domain could be used. The application of chemometric approaches to imaging datasets is in fact more complex, both from a conceptual and practical point of view. Although a large part of the LIBS community is increasingly sensitive to the use of chemometric tools, understanding the concept of hyperspectral imaging, finding appropriate tools for data exploration, and finally interpreting their outputs represent a big task for many non-expert researchers. In addition, it is clear that managing millions of spectra increases the difficulty of this task even if they know the great potential of chemometrics. This is not just about the availability of computational resources, but also, the development of new data exploration tools able to manage such big data structures. Beyond this opinion, which may seem a bit negative, we must consider that there is an evolution of chemometrics within the LIBS community with a real increase of competences, even if the number of publications on the subject is still limited. From this first observation, we could say that everything is going well in the field of LIBS imaging and there are no real obstacles to overcome. So what is the problem? The problem lies in the fact that we want to know everything about the sample we are analyzing, which is quite commendable for a scientist. More precisely, we want to extract information on both major and minor compounds and even traces. However, minor compounds and traces are often present on a small number of pixels representing a very small variance in the spectral dataset. Unfortunately, the majority of chemometric algorithms exploiting the concept of expressed variance do not (or hardly) allow the detection of these compounds, especially when the signal-to-noise ratio is limited. It is therefore the purpose of this chapter to introduce the IFF algorithm (Interesting features finder) that we have developed in this thesis, the objective of which is to give all compounds a chance to be detected regardless of their concentration [202].

III.2. The paper published in SAB

Spectrochimica Acta Part B: Atomic Spectroscopy 195 (2022) 106508

Contents lists available at ScienceDirect

Spectrochimica Acta Part B: Atomic Spectroscopy

journal homepage: www.elsevier.com/locate/sab

Interesting features finder (IFF): Another way to explore spectroscopic imaging data sets giving minor compounds and traces a chance to express themselves

Qicheng Wu [a], César Marina-Montes [b], Jorge O. Cáceres [c], Jesús Anzano [b], Vincent Motto-Ros [d], Ludovic Duponchel [a,*]

[a] Univ. Lille, CNRS, UMR 8516 – LASIRE – Laboratoire de Spectroscopie pour Les Interactions, La Réactivité et L'Environnement, Lille F-59000, France
[b] Laser Lab, Chemistry & Environment Group, Department of Analytical Chemistry, Faculty of Sciences, University of Zaragoza, Pedro Cerbuna 12, 50009 Zaragoza, Spain
[c] Laser Chemistry Research Group, Department of Analytical Chemistry, Faculty of Chemistry, Complutense University of Madrid, Plaza de Ciencias 1, 28040 Madrid, Spain
[d] Institut Lumière Matière, UMR 5306, Université Lyon 1 – CNRS, Université de Lyon, Villeurbanne 69622, France

ARTICLE INFO

Keywords:
LIBS imaging
Chemometrics
Spectral selection
Minor compounds
Traces
Pixel detection

ABSTRACT

Today, we acquire larger and larger spectroscopic imaging data sets on complex samples. Even before proceeding with a spectroscopic analysis, we often have information concerning for example the presence of major compounds. However, we are not in the same position regarding the presence and location of minor compounds and traces in the sample, while this is generally a more interesting piece of information. Modern spectroscopic imaging uses chemometric tools that allow the simultaneous exploration of the entire spectral range available. These well-tested tools, such as principal component analysis, often exploit the variance contained in the data set to extract maximum chemical information. In general, we can say that these approaches are quite efficient but they are not completely adapted to the characteristics of the data acquired during a spectral imaging experiment. Indeed, such data sets have generally a limited signal to noise ratio and minor compounds and traces are often present on a small number of pixels compared to the total number in the considered data set. It is then quite possible that these compounds are present in a sample but not detected by the chosen multivariate tool. The goal of this work is to introduce an approach called *Interesting Features Finder* (IFF) able to retrieve minor compounds and traces independently of the variance they may express in the spectral data set. Like other state of the art methods, it uses the notion of convex hull but with the great advantage of working directly on the raw data, without prior projection to reduce their dimensionality. By means of a synthetic spectral data set and a micro-LIBS (laser-induced breakdown spectroscopy) imaging one acquired on a sample taken in Antarctica, we will show the potential of this approach in terms of sensitivity of detection of compounds but also of robustness against noise.

1. Introduction

Chemometrics began in the 1970s driven by a few far-sighted individuals who perceived the power of applying computer-based algorithms to processing analytical data [1]. This was of course possible as soon as they had enough data on the samples they wanted to explore and this is exactly what spectroscopy would bring. At the same time, it was demonstrated that it is possible to predict the concentrations of products of interest in complex samples by means of their near-infrared spectra introduced in a multivariate regression model, which would completely change the field of analytical chemistry and many other fields [2,3]. It is obvious that the history of vibrational spectroscopy is closely linked to that of chemometrics. Vibrational spectroscopy has first of all shown by its needs the way that chemometrics should take for a better valorization of the acquired spectral data. After several decades, the roles are even reversed in the sense that new concepts of data processing using particular data structures can lead us to think about new instrumental developments able to generate such data.

---

* Corresponding author.
E-mail address: ludovic.duponchel@univ-lille.fr (L. Duponchel).

https://doi.org/10.1016/j.sab.2022.106508
Received 1 July 2022; Received in revised form 28 July 2022; Accepted 30 July 2022

What we have just described for vibrational spectroscopy has been observed and is still observed for all spectroscopies, Laser-Induced Breakdown Spectroscopy (LIBS) being no exception to this evolution with of course different timing. The 1960s saw the birth of LIBS, with instrumental development focusing on microanalysis [4]. For many years, this spectroscopy has been primarily a physicists' technique used for bulk analysis. It is only since the 2000s that researchers have been highlighting the real analytical potential of LIBS microanalysis and imaging [5]. Their works has shown that this imaging technique has many interesting characteristics that few analytical techniques can claim, such as acquisition rates of up to 1000 Hz (i.e. 1000 spectra/s) [6], a spatial resolution at the micrometer scale [7], allowing a spectral and spatial exploration of very large areas of a sample [8]. In the last ten years, we have seen a clear acceleration of LIBS imaging with increasingly fast, accurate and reproducible measurements. The amount of data acquired has also increased significantly since we have gone from about 1000 spectra acquired for a sample in 2010 to more than 10 million spectra today, an increase in the amount of data by a factor of 10 every 2 years [9–11]. It should be noted that LIBS imaging is certainly the only one to have shown such a rapid evolution over such a short period. As a first sight, the low bandwidth of the observed emission lines suggests that a simple integration of the signal at a given wavelength should allow us to generate a map of an element of interest. Specialists in the field know that one must be careful on this last point. Indeed, the richness of the elemental spectra and the presence of many elements in heterogeneous samples does not allow us to unanimously ensure that the selected wavelength is specific to a single element. Therefore, chemical maps generated in this way should be treated with the utmost caution. In order to address this issue but also to propose a more exhaustive exploration of LIBS imaging data sets, chemometric methodologies have been developed in recent years to simultaneously explore the whole spectral range available. Tools as simple as Principal Component Analysis (PCA) [12] but also more advanced methodologies based on classification [13], clustering [14], or even spectral unmixing in the context of data fusion between LIBS and Plasma Induced Luminescence (PIL) [15] or LIBS and Raman spectroscopies [16] have been implemented and much more [17]. However, we had to adapt our data processing methodologies because the application of these classical chemometrics tools is not without difficulty when the spectral data set contains more than one million spectra.

The previous paragraphs tend to show the excellent dynamism of LIBS imaging with more and more reliable and fast instrumentations associated to chemometric analysis for the exploration of always-larger data sets. However, a problem persists in the multivariate processing of spectral data. Indeed, during the exploration of a data set we want to be as exhaustive as possible and therefore detect both major and minor compounds and traces. Unfortunately, minor compounds and traces are often present on a small number of pixels (compared to the total number of pixels in the data set) therefore associated with very low explained variances. This is the problem because the majority of chemometric algorithms using the concept of expressed variance do not (or hardly) allow the detection of these compounds, especially when the signal to noise ratio is limited. The aim of this work is to introduce a new algorithm called *Interesting Features Finder* (IFF), based on the concept of convex hull, capable of detecting the presence of compounds whether they are major, minor or trace. In the following sections, we will first describe the IFF algorithm and what it can bring compared to a state-of-the-art approach, called *Essential Spectral Pixels* (ESP) [18,19]. We will then introduce a synthetic data set as well as a LIBS imaging data set from an Antarctic aerosol measurement campaign. Finally, we will apply our approach to show what it can bring to the exploration of of complex samples.

2. Material and methods

2.1. Interesting features finder (IFF)

In order to understand the IFF algorithm, we need to represent our spectra in a different but commonly used way in chemometrics. This allows us to make a mental representation quite different from the spectra we observe on our computer. Therefore, a spectrum is considered as a point (or a vector) in a multidimensional space as represented in Fig. 1a. This multidimentional space has as many dimensions as there are wavelengths (p) in a spectrum. As observed, a data set takes the form of a cloud of points with varying densities throughout the volume. The questions that arise now are: what is the convex hull of such a point cloud (i.e. the spectral data set) and why can it be useful for our data exploration problem? A convex hull is a geometric object with applications in many scientific fields as varied as pure mathematics [20], statistics [21], economics [22], ethology [23] or quantum physics [24] to name a few. As represented in Fig. 1b, the convex hull is the region bounded by a balloon that would deflate as it contracts to its minimum, carried by the outer points of the point cloud. The number of points on the convex hull (only 4 spectra for this toy example) is then very limited compared to the total number of spectra in the data set. All the interest of this concept lies in the fact that, mathematically, all the spectra inside the convex hull are linear combinations of the spectra on its surface. Consequently, major / minor compounds and traces can potentially be found on the surface of the convex hull regardless of the variance they may express in the data set. So how to find the convex hull of a data set? The majority of the software proposing the calculation of the convex hull of a data set uses the *Quickhull* algorithm published in 1996 [25]. This is the approach proposed in the well-known *Matlab* computing environment but is also found in many others. However, it is very difficult and even sometimes impossible to calculate the convex hull of a data set when it is huge and more importantly when the number of dimensions of the considered data space exceeds 5–6. Of course, we have always much more than 5–6 wavelengths in our spectral range and our LIBS imaging data sets are getting bigger and bigger (sometimes with several million spectra). Aware of the interest of the convex hull, a team of chemometricians has recently proposed to use PCA beforehand in order to reduce the number of dimensions to investigate in a method they called ESP [18,19]. Very interesting results were published with the method by keeping only the scores of the first 5 or 6 principal components on which the convex hull could be extracted. From our point of view, using a preliminary compression method and fixing a number of components a priori remains rather risky in our case. Indeed, this would mean potentially losing any chance of seeing traces or even minor compounds despite obtaining the convex hull. It is in this sense that we propose in this work a direct calculation of the convex hull on the raw data set (i.e. whatever the number of spectral variables and the total number of pixels) using the *Interesting Features Finder* (IFF) tool we have developed.

The IFF algorithm is finally based on a rather simple idea since we successively project the whole data set on a large number of randomly drawn vectors. Fig. 1c illustrates this principle. Given a first random vector in the data space, we make an orthogonal projection of all spectra of the data set onto it. We then identify the 2 spectra with the most extreme coordinates on this axis. Next, we keep this information in a list and update the selection frequency of a spectrum if it has already been selected for previous random vectors. After the exploitation of a large number of random vectors (10,000−100,000), the final list contains the most interesting spectra of the data set, their selection frequency being used to measure their importance. In order to further reduce the list of selected pixels, we keep only the pixels with a selection frequency higher than 2% compared to the most frequently selected pixel in the data set, which represents 100%. At first sight, the choice of this percentage may seem arbitrary. This criterion can appear quite arbitrary. Nevertheless, we should not forget that this method is unsupervised and thus corresponds to a blind analysis of the dataset. Future users will have to modify

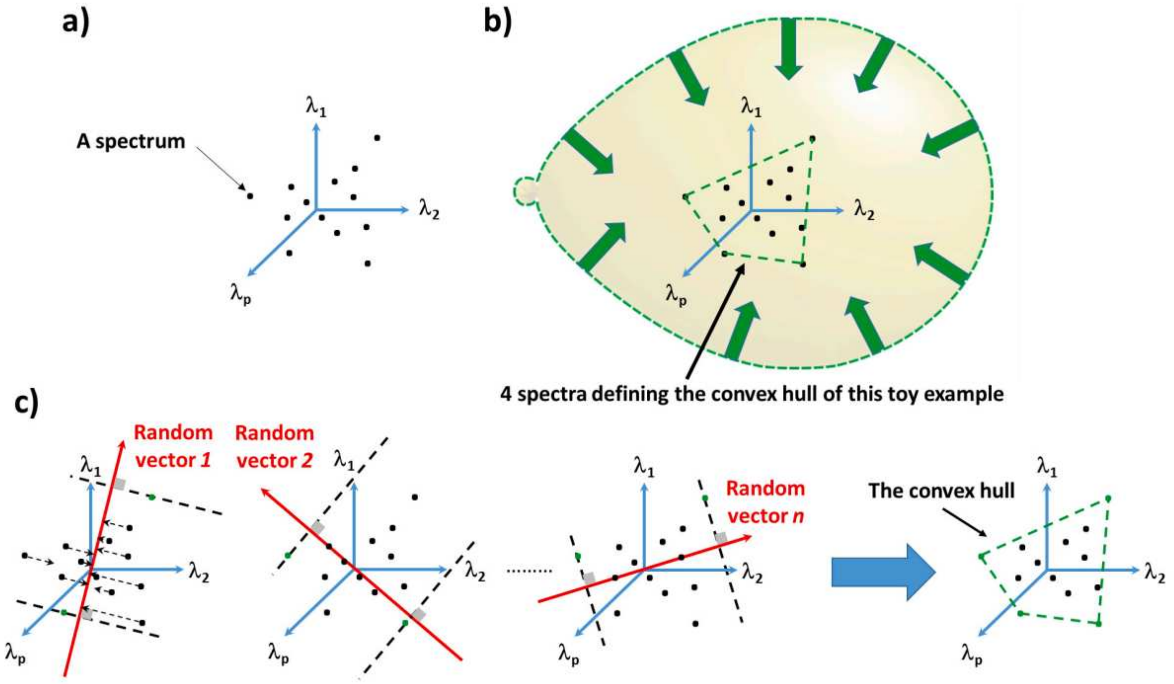

Fig. 1. a) Representation of a spectroscopic data set in a multidimensional space and b) the corresponding convex hull. c) Successive steps of the IFF algorithm in order to obtain the convex hull of the data set from its raw form.

this percentage according to the signal-to-noise ratio of the dataset. However, they will have to take the largest percentage possible in order to keep a limited list of pixels at the risk of losing the interest of the concept with a final list that would be unmanageable.

All calculations in this work have been performed under the Matlab 2016b environment. The Matlab code of the *IFF* algorithm is provided in the supplementary material.

2.2. *Spectroscopic data sets*

The first data set used in this work consist of synthetic LIBS spectra we have generated considering a small spectral range. The advantage of using such simulations lies in the fact that all the parameters potentially influencing a given problem are under control. Then it will be possible to generate spectral interferences between the present elements but also apply different noise levels. Since we will have generated these data, we have access to a ground truth concerning, in our case, the presence of pure pixels in the selection of spectra proposed by the ESP and IFF approaches. Fig. 1S in supplementary material shows the seven pure spectra considered in this simulation containing 500 spectral variables each. We have then generated 230,230 synthetic spectra by linear combinations of these 7 pure spectra considering concentrations varying from 0 to 1 by step of 0.05 imposing the constraint to have the sum of the 7 concentrations equal to 1. A white noise varying from 2 to 8% of the average intensity of the spectrum has also been added to each spectrum, which allow to test the robustness of the approaches to this often very critical parameter in the analysis of spectroscopic data. Fig. 2S in supplementary material shows as an example a spectrum of a mixture extracted from the data set containing approximately the same concentration for the 7 elements as a function of the applied noise level. It is easy to notice that the observation of the 7 contributions in the considered spectrum is already difficult when the noise is absent but also that the four most intense spectral contributions initially observed are at the limit of the detection for the most important noise levels.

The second data set considered in this work is a real one. It was obtained through LIBS imaging measurements made on one of the atmospheric aerosol samples collected during the 2018/2019 Spanish Antarctic campaign in the surroundings of the Spanish Antarctic Research station “Gabriel de Castilla” on Deception Island (62°58′09”S, 60°42′33”W). The objective of the study was to better understand the origin of airborne particles in this specific region of the globe. We only give here the main information concerning the sample preparation and the acquisition parameters for this LIBS imaging experiment, readers interested in the subject being invited to a previous work already published [26]. Regarding the preparation of the sample, air particles were first collected in a circular quartz microfiber filter paper through a high-volume sampler (30.6 m^3 /h) considering a total sampling time of 72 h. We then cut a small part of the filter for analysis by LIBS imaging. The micro LIBS instrumental setup used in this study has also been previously described in detail elsewhere [27,28]. In short, a Q-switched Nd:YAG laser (Centurion GRM, Quantel) working at 1064 nm, with a pulse duration of 8 ns, 8 μm beam diameter and a repetition rate of 100 Hz, was used for plasma creation. The laser pulse was vertically focused onto the sample by a 15× magnification objective (LMM-15XeP01, Thorlabs) creating a typical crater size in the range of 6–7 μm. The instrument was equipped with a motorized translation 3-axis (XYZ) stage in order to generate the mapping. Plasma light was collected by a quartz lens and fiber bundle connected to a Czerny-Turner spectrometer (Shamrock 500, Andor Technology) assembled with an intensified charge-coupled device (ICCD) camera (iStar, Andor Technology). Under these conditions, we were able to acquire a spectral data cube of size 380 pixels × 126 pixels × 1845 wavelengths, i.e. 47,800 spectra acquired in just under 8 min in the 294.45–374.35 nm spectral domain.

3. Results and discussion

The objective of this first part is to evaluate the potential of our IFF algorithm against the state of the art in the field of chemometrics, i.e. the ESP algorithm, by considering an increasing level of complexity through a decrease of the signal to noise ratio on the simulated data set. It seemed interesting to start with the exploration of a trivial case, i.e. the data set of 230,230 spectra without added noise. Thus, the ESP approach was applied on the data set considering 5 principal components to compress the initial data while 10,000 random vectors were considered for IFF. Not surprisingly, both approaches extracted only the 7 pure spectra. Nevertheless, we notice an interesting property of the ESP algorithm, already underlined in previous works [18,19], which despite a limited number of 5 principal components is able to select the 7 pure spectra. We will now see that things change radically as soon as noise is present. The ESP and IFF methods are then applied to the 2% noise data set under the same conditions as before. The 7 pure spectra are again well selected by both approaches in these new conditions but they are now included in a list of 294 spectra for ESP and 88 for IFF. In order to observe the distribution of the selected spectra within the data set, we represent them all within a PCA space in Figs. 2 and 3 for the ESP and IFF methods respectively. Thus, for each hyperplane defined by a combination of two principal components, the green dots represent the pure spectra selected by the considered algorithm. The red dots represent the other selected spectra also present in the list, while the blue dots represent all the other spectra in the data set. Beyond the number of selected spectra, which is very different between the two approaches, we notice in these two figures that the spectra selected by IFF are localized around the pure spectra while the selection is much more diffuse for ESP. We notice here an interesting property of IFF which, in spite of the absence of filtering (since it works on the raw data), finds the pure spectra present in the data set. If we now look at a noise level of 4%, things become much more complicated. Under these new conditions, the ESP approach selects 327 spectra, a list in which only 5 pure spectra are present (the first and the sixth being absent). On its side, the IFF method selects 186 spectra, the 7 pure spectra being included in this list. There is a clear increase in the number of spectra selected for the IFF approach compared to the 2% noise level. As before, these two selections are represented in a PCA space in Figs. 3S and 4S of supplementary material for the ESP and IFF approaches respectively. The color coding of the spectra is the same as before. Additionally, back dots represent the pure spectra present in the data set but not selected by the approach. We can make the same observation as before on the distribution of the spectra selected by the two approaches. Finally, if we now look at the highest noise level of 8%, the situation is naturally even more extreme. The ESP method selects 232 spectra in which only 4 pure spectra are present. The IFF method selects 788 spectra containing the 7 pure spectra. It is undeniable that the number of spectra selected by IFF increases a lot compared to the previous noise level. Nevertheless, this number must be relativized in the sense that it remains limited compared to the 232,230 spectra present in the data set but also because we have simulated here more than degraded measurement conditions. These two selections are also represented in a PCA space in Figs. 5S and 6S of supplementary material. At first sight, it seems surprising to see the difference between the IFF and ESP approaches in the face of an increasing noise level, even though the latter uses a prior PCA filtering step. We could then naturally say to ourselves that this number of 5 components used in the ESP approach is perhaps too limited. Table 1 shows the evolution of the spectra selection made by the ESP approach considering an increasing number of principal components on the same data set at 8% noise. We observe that the increase in the number of components allows us to go from 4 to 5 pure spectra detected without ever being able to detect all the pure ones in the data set even for a number of 9 principal components. The use of a larger number of components is also accompanied by a clear increase in the number of spectra selected and the calculation time. This first part, based on the exploitation of simulated spectral data, allowed us to show the relevance of the selection of spectra proposed by the IFF algorithm with a certain robustness against the noise very often observed in single shot LIBS analysis.

The second part of this study focusses on the exploration of the LIBS imaging data set acquired on the atmospheric aerosol sample. Before going into the actual application of the IFF approach on such a data set, it is interesting to go back to the exploration procedure that we usually use in spectroscopic imaging. In a first step, we usually calculate the mean spectrum from the 47,800 spectra of the data set (Fig. 4a). On this spectrum, we quickly identify the element Si which is mainly contained in the quartz filter but also other elements such as Na, Al, Ca, and Fe. Without a prior knowledge of the analyzed sample, the usual procedure would be to select a given wavelength from the observation of this spectrum in order to generate a distribution map of the supposed element. As a second step, we can also generate a global integration image by summing for each pixel all the intensities over the whole spectral domain (Fig. 4b). The color scale used here is logarithmic because there is a very large dynamic on the integrated values. This representation validates the particulate character of our sample but naturally without giving any chemical information since this information is lost during the integration of the signals. We then have two options for further exploration of the data set depending on whether or not we want to use chemometric tools. If not, we will generate classical distribution maps for the elements mentioned above by selecting specific wavelengths a priori. This task, which seems to be very simple, hides in fact a rather long procedure if one wishes to generate the least biased chemical maps. Indeed, for a given element, we must find a wavelength in the spectral range without interference, which is very likely in LIBS due to the richness of the spectra and the large number of elements present. If we want to have another point of view on these data, it is then advisable to use chemometric tools for a multivariate exploration that is to say exploiting simultaneously all the wavelengths. The first tool used in this case is often PCA, which is a simple, quick and quite effective approach. It is a multivariate factorial method based on the criterion of maximum expressed variance. It compresses the data for an easier observation of the spectral variations present in the data set. The application of this approach to our LIBS data set showed that 7 principal components were needed to describe the spectral variations it contains, expressing 97.93% of the total variance. Higher principal components where not considered since they only exhibit noise structures. This evaluation was done using the scree plot presented in the supplementary material (Fig. 7S). Fig. 5 shows these 7 principal components and the associated scores maps. As can be seen, the multivariate nature of PCA brings to light correlations and/or anti-correlations between elements at the spectral level, but also their relative contributions to the score maps at the spatial level. So for example, the red pixels of the score map 1 have relatively higher concentrations of the elements Si, Na, Fe, Al and Ca (which are correlated) than the blue pixels in this same map. Component 2 shows an anti-correlation between several elements. More precisely, the red pixels of the score map 2 have relatively more Na and Si and less Fe and Al than the blue ones and vice versa. Principal component 3 is interesting since it shows for the first time the presence of Cr correlated to Fe and Ca but also anti-correlated to Na and Al. It was not possible to see Cr in the mean spectrum. The principal component 4 shows above all a Si contribution, this time specific to the quartz filter as one can suppose in front of the absence of particulate structure on the associated score map. While principal component 5 contains elements already mentioned with of course different concentration ratios, components 6 and 7 allow in turn to detect the presence of Ti, not easily observable on the mean spectrum. As we can see, PCA offers an interesting exploration of the data set but the spatially unstructured nature of our sample (with no continuous region often observed on other samples) makes the comparison of score maps and pixel collocations more than delicate. Moreover, it focuses primarily on the relative variations at the spectral level without really highlighting the particular character of certain particles located on specific pixels. We then applied the IFF approach on the same data set considering 10,000 random vectors. As a result, 45 interesting pixels out of the 48,132 present in the data set have been selected. The spatial localization of these spectra and their selection frequencies are shown in Fig. 8S and Table 1S respectively in supplementary material. At the time, this result seemed quite surprising because it was quite unlikely to have 45 types of particles in such a sample. The correlation matrix between all these spectra was therefore calculated (Fig. 9S in supplementary material). Not surprisingly, many correlations greater

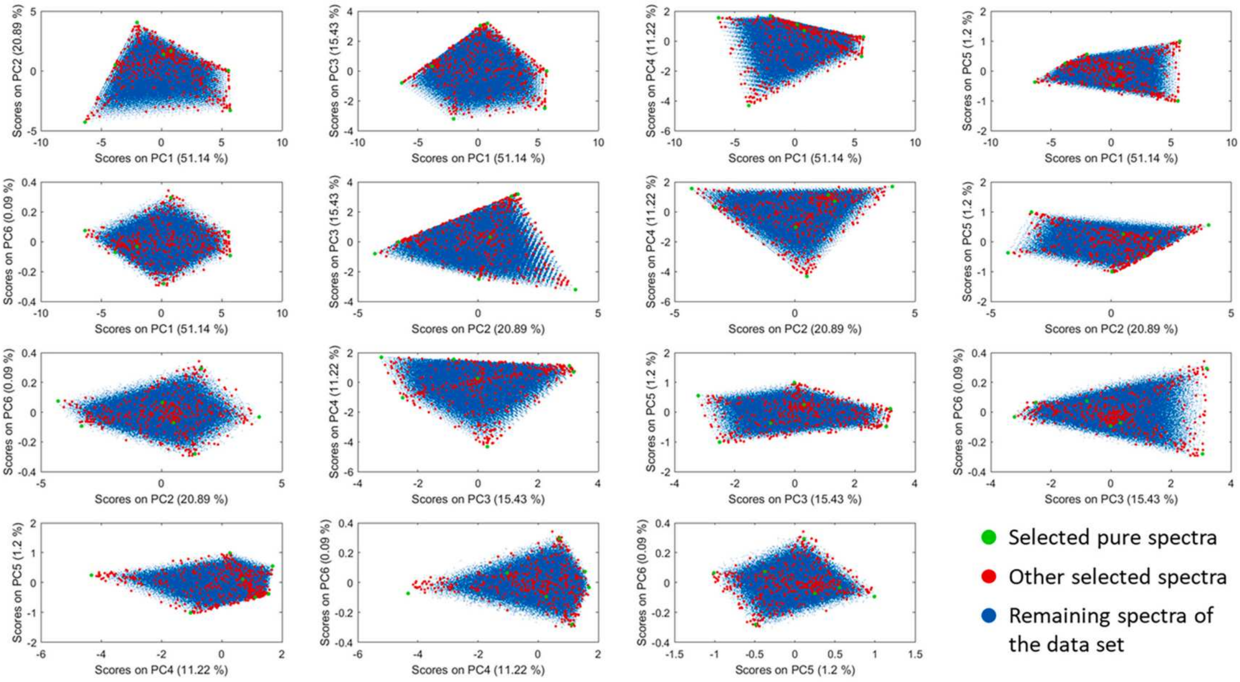

Fig. 2. Representation of the pixels selected by ESP vs the rest of the data set in a PCA space considering a 2% noise level.

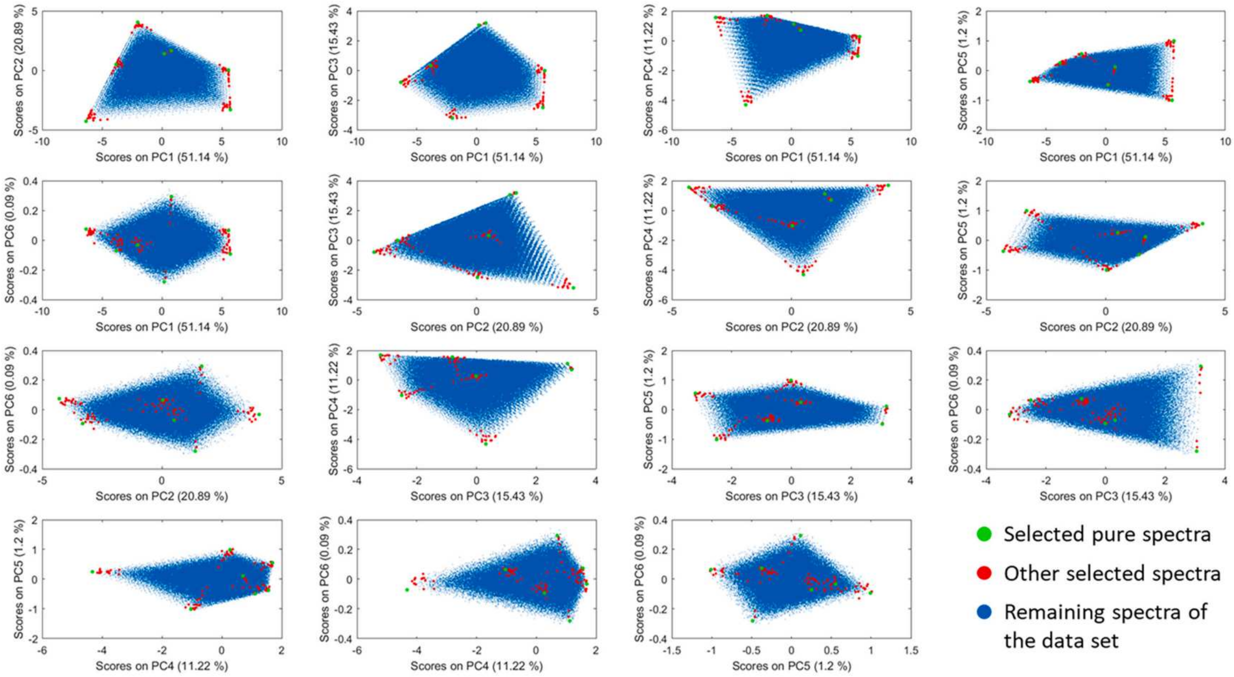

Fig. 3. Representation of the pixels selected by IFF vs the rest of the data set in a PCA space considering a 2% noise level.

Table 1
Evolution of the spectra selection made by the ESP approach considering an increasing number of principal components on the same data set at 8% noise.

Number of PCs used in the ESP approach	Number of selected spectra	Pure spectra included in the selection (/ 7)	Computation time (s)
5	232	4	1
6	707	5	10
7	1468	5	21
8	2764	5	62
9	4708	5	650

than 0.96 are observed. For example, spectrum 1 is very similar to the spectra 4, 29, 39 and 41 with correlations of 0.96, 0.99, 0.99 and 0.96 respectively. This is due to the fact that there are very small variations in elemental concentration between these spectra with, to a lesser extent, the noise that also participates in the phenomenon. As a consequence, a correlation higher than 0.96 allowed us to group the spectra into 16 distinct families obtained using the mean spectrum of each group. We should not misunderstand here the efficiency of the IFF algorithm which accounts for all types of variations from the largest to the most subtle. The 45 spectra are thus well located on the convex hull but from an analytical point of view, there are in fact only 16 typical spectra represented in Fig. 6. First of all, we find in these spectra the contributions of the elements detected during the PCA but we now also have specific elemental concentration ratios for each of them. We recall here that by definition, none of these spectra can be found by linear combinations of the others, which allows us to insist on their representativeness within the data set. On the other hand, all the spectra in the data set are potentially linear combinations of these 16 representative spectra. The most interesting in this selection is certainly the detection of Cu and Ni present in the contributions 5, 14 and 16 respectively. It was not possible to observe these elements either in the mean spectrum or even with PCA despite its recognized sensitivity. For information, the application of the ESP approach considering 6 principal components on this same data set, generates a list of 133 spectra containing all the types of particles presented in Fig. 6 except the three previously mentioned. The detection of Cu and Ni is therefore not possible in this case. Moreover, an increase in the number of components does not change the situation. This work has shown that the IFF algorithm has interesting capabilities to identify compounds present in a complex sample independently of their concentration while being relatively robust to the noise often present on the spectra. It is obvious that such an approach complements the range of chemometric tools such as PCA by offering a completely different view of the spectral data.

4. Conclusion

The detection of minor and trace compounds is always a delicate task in analytical chemistry. It is even more challenging today in LIBS imaging as we generate ever larger spectral data sets. As we have seen in this work, classical chemometrics tools are not always optimal to extract such information. It is in this sense that we have introduced the IFF approach in order to extract these compounds of interest independently of the variance they may express in the data set. The originality of the algorithm concerns the direct exploitation of the data (i.e. without prior compression) in order to extract the convex envelope. By means of a simulated dataset and a LIBS imaging one acquired on atmospheric aerosols, we have highlighted the sensitivity of our approach but also its potential robustness against noise, which is particularly important in the context of spectroscopic imaging. Two questions could then legitimately be asked: when and how to use such a tool? Many researchers who are new to chemometrics think that there must be an ideal tool to exhaustively extract all the information contained in a data set. This is not the case and we must instead use different tools, each with its own advantages and disadvantages, in order to obtain the least biased vision of the chemical system we are exploring. In other words, we add the IFF approach to the chemometric toolbox next to PCA or many others. If we are not familiar with the concepts of chemometrics, we can use the IFF approach without much thought. It will then present us with a selection of spectra that we will be able to observe and from which we will most probably be able to observe unsuspected emission lines since they are not visible on the mean spectrum. We can then generate maps by integrating the signal at these wavelengths. If, on the contrary, we want to go further in chemometric exploration, we could use this selection of spectra to generate initial estimates of the pure compounds present in the explored sample in order to do a signal unmixing as for example with MCR-ALS but this is beyond the scope of this work [15].

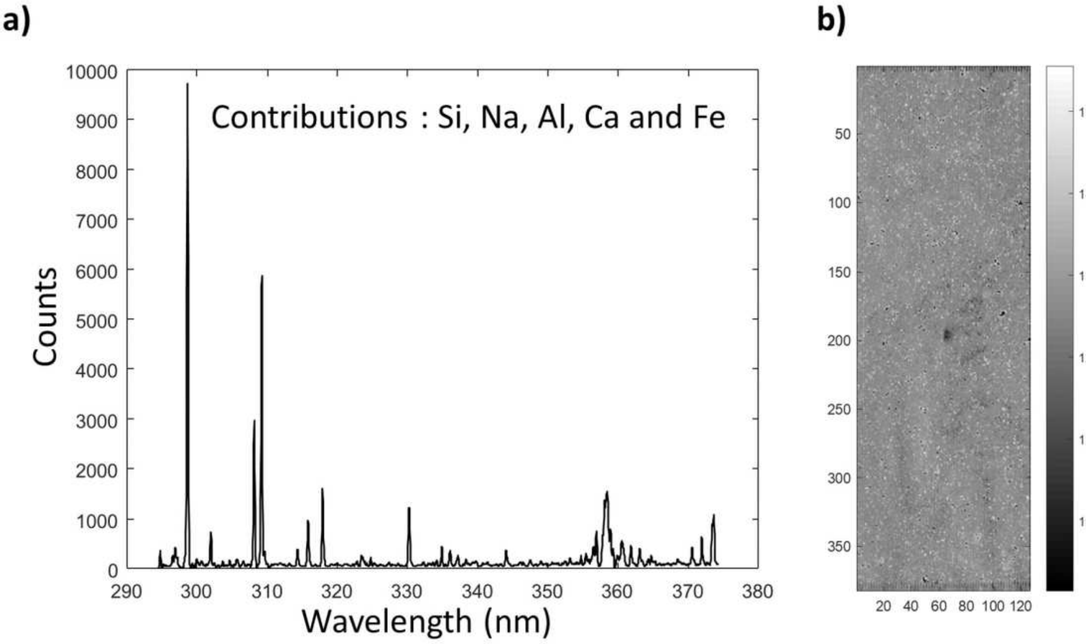

Fig. 4. a) The mean spectrum of the data set. b) The global integration image.

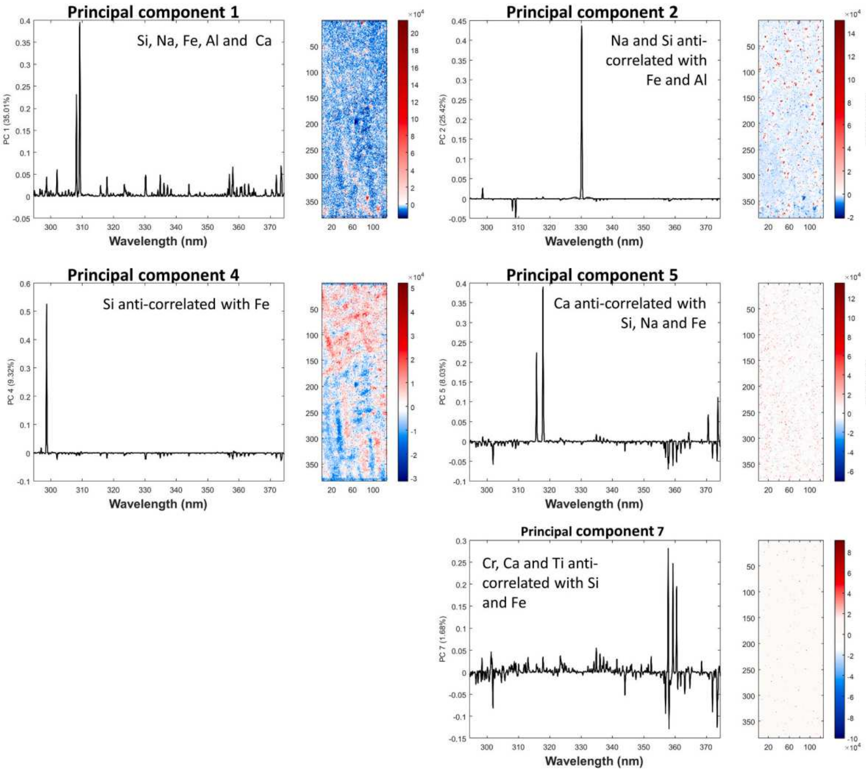

Fig. 5. Principal component analysis (PCA) of the LIBS imaging data set.

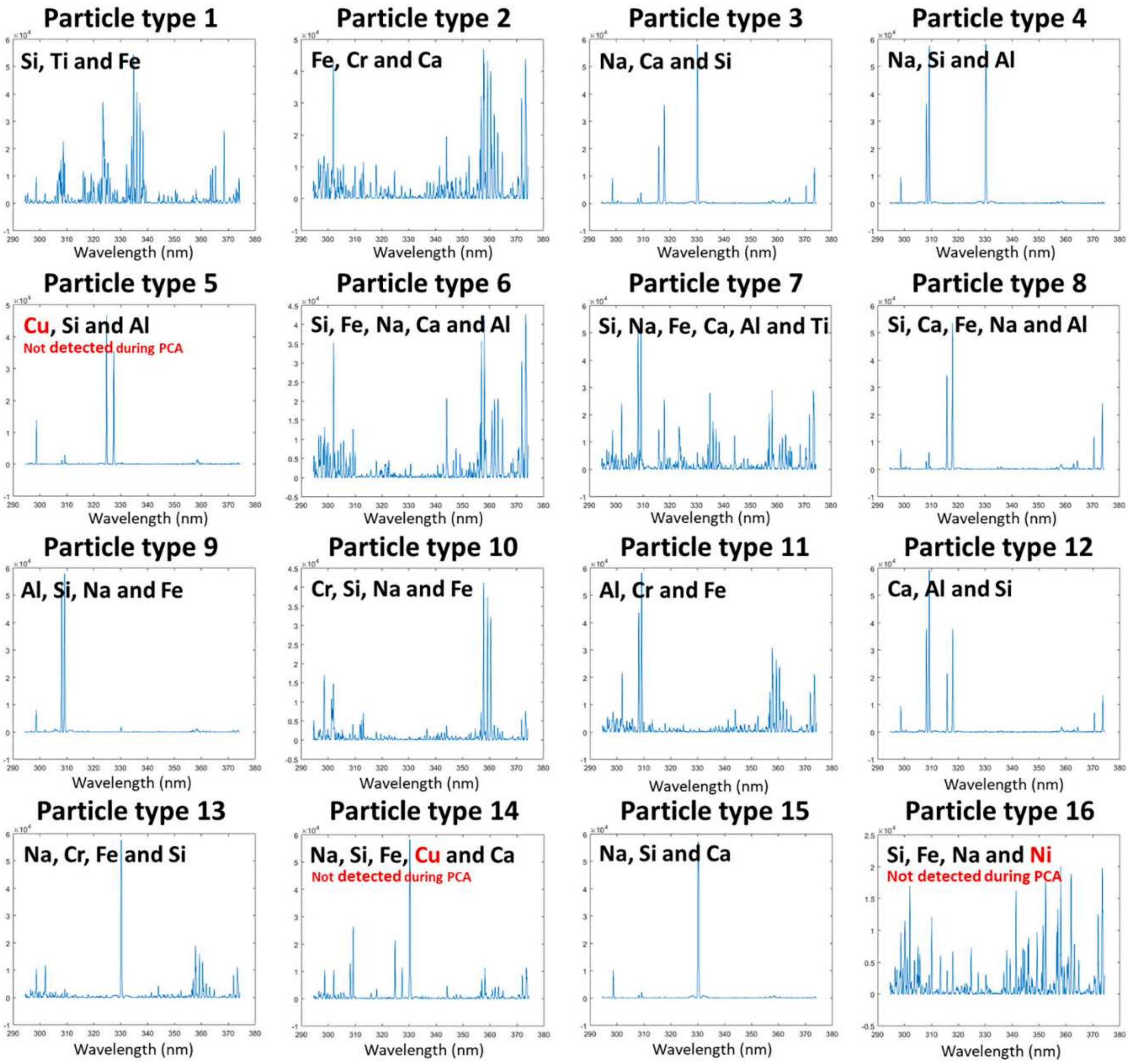

Fig. 6. Representation of the final list of the 16 typical spectra.

Author statement

All authors participated equally in this work.

Aknowledgement

This work was partially supported by the French region Rhônes Alpes Auvergne (Optolyse, CPER2016) and the French National Research Agency (ANR- Diagem project).

Declaration of Competing Interest

The authors declare that they have no known competing financial interests or personal relationships that could have appeared to influence the work reported in this paper.

Data availability

The authors do not have permission to share data.

Appendix A. Supplementary data

Supplementary data to this article can be found online at https://doi.org/10.1016/j.sab.2022.106508.

References

[1] D. Duewer, Bruce R. Kowalski, 7 Mar 1942 to 1 Dec 2012, Aust. J. Chem. 28 (2014) (7 Mar 1942) 319–320, https://doi.org/10.1002/cem.2622.

[2] I. Ben-Gera, K.H. Norris, Determination of moisture content in soybeans by direct spectrophotometry, Israel, J. Agric. Res. 18 (1968) 125–132.

[3] I. Ben-Gera, K.H. Norris, Direct spectrophotometric determination of fat and moisture in meat products, J. Food Sci. 33 (1968) 64–67.

[4] M. Baudelet, B.W. Smith, The first years of laser-induced breakdown spectroscopy, J. Anal. At. Spectrom. 28 (2013) 624–629, https://doi.org/10.1039/C3JA50027F.

[5] P. Fichet, J.-L. Lacour, D. Menut, P. Mauchien, A. Rivoallan, C. Fabre, J. Dubessy, M.-C. Boiron, Micro LIBS technique, in: A.W. Miziolek, I. Schechter, V. Palleschi (Eds.), Laser Induced Breakdown Spectroscopy, Cambridge University Press, Cambridge, 2006, pp. 539–555, https://doi.org/10.1017/CBO9780511541261.017.

[6] H. Bette, R. Noll, High speed laser-induced breakdown spectrometry for scanning microanalysis, J. Phys. D. Appl. Phys. 37 (2004) 1281–1288, https://doi.org/10.1088/0022-3727/37/8/018.

[7] D. Menut, P. Fichet, J.-L. Lacour, A. Rivoallan, P. Mauchien, Micro-laser-induced breakdown spectroscopy technique: a powerful method for performing quantitative surface mapping on conductive and nonconductive samples, Appl. Opt. 42 (2003) 6063, https://doi.org/10.1364/AO.42.006063.

[8] J.M. Vadillo, J.J. Laserna, Laser-induced plasma spectrometry: truly a surface analytical tool, Spectrochim. Acta B At. Spectrosc. 59 (2004) 147–161, https://doi.org/10.1016/j.sab.2003.11.006.

[9] V. Motto-Ros, L. Sancey, X.C. Wang, Q.L. Ma, F. Lux, X.S. Bai, G. Panczer, O. Tillement, J. Yu, Mapping nanoparticles injected into a biological tissue using laser-induced breakdown spectroscopy, Spectrochim. Acta B At. Spectrosc. 87 (2013) 168–174, https://doi.org/10.1016/j.sab.2013.05.020.

[10] Y. Gimenez, B. Busser, F. Trichard, A. Kulesza, J.M. Laurent, V. Zaun, F. Lux, J. M. Benoit, G. Panczer, P. Dugourd, O. Tillement, F. Pelascini, L. Sancey, V. Motto-Ros, 3D imaging of nanoparticle distribution in biological tissue by laser-induced breakdown spectroscopy, Sci. Rep. 6 (2016) 29936, https://doi.org/10.1038/srep29936.

[11] X. Le Guével, M. Henry, V. Motto-Ros, E. Longo, M.I. Montañez, F. Pelascini, O. de La Rochefoucauld, P. Zeitoun, J.-L. Coll, V. Josserand, L. Sancey, Elemental and optical imaging evaluation of zwitterionic gold nanoclusters in glioblastoma mouse models, Nanoscale. 10 (2018) 18657–18664, https://doi.org/10.1039/C8NR05299A.

[12] S. Moncayo, L. Duponchel, N. Mousavipak, G. Panczer, F. Trichard, B. Bousquet, F. Pelascini, V. Motto-Ros, Exploration of megapixel hyperspectral LIBS images using principal component analysis, J. Anal. At. Spectrom. 33 (2018) 210–220, https://doi.org/10.1039/C7JA00398F.

[13] J. Vrábel, E. Képeš, L. Duponchel, V. Motto-Ros, C. Fabre, S. Connemann, F. Schreckenberg, P. Prasse, D. Riebe, R. Junjuri, M.K. Gundawar, X. Tan, P. Pořízka, J. Kaiser, Classification of challenging laser-induced breakdown spectroscopy soil sample data - EMSLIBS contest, Spectrochim. Acta B At. Spectrosc. 169 (2020), 105872, https://doi.org/10.1016/j.sab.2020.105872.

[14] A. Nardecchia, C. Fabre, J. Cauzid, F. Pelascini, V. Motto-Ros, L. Duponchel, Detection of minor compounds in complex mineral samples from millions of spectra: a new data analysis strategy in LIBS imaging, Anal. Chim. Acta 1114 (2020) 66–73, https://doi.org/10.1016/j.aca.2020.04.005.

[15] A. Nardecchia, A. de Juan, V. Motto-Ros, M. Gaft, L. Duponchel, Data fusion of LIBS and PIL hyperspectral imaging: understanding the luminescence phenomenon of a complex mineral sample, Anal. Chim. Acta 1192 (2022), 339368, https://doi.org/10.1016/j.aca.2021.339368.

[16] A. Nardecchia, A. de Juan, V. Motto-Ros, C. Fabre, L. Duponchel, LIBS and Raman data fusion: an original approach based on the use of chemometric methodologies, Spectrochim. Acta B At. Spectrosc. (2022). Submitted.

[17] A. Limbeck, L. Brunnbauer, H. Lohninger, P. Pořízka, P. Modlitbová, J. Kaiser, P. Janovszky, A. Kéri, G. Galbács, Methodology and applications of elemental mapping by laser induced breakdown spectroscopy, Anal. Chim. Acta 1147 (2021) 72–98, https://doi.org/10.1016/j.aca.2020.12.054.

[18] M. Ghaffari, N. Omidikia, C. Ruckebusch, Essential spectral pixels for multivariate curve resolution of chemical images, Anal. Chem. 91 (2019) 10943–10948, https://doi.org/10.1021/acs.analchem.9b02890.

[19] L. Coic, P.-Y. Sacré, A. Dispas, C. De Bleye, M. Fillet, C. Ruckebusch, P. Hubert, É. Ziemons, Selection of essential spectra to improve the multivariate curve resolution of minor compounds in complex pharmaceutical formulations, Anal. Chim. Acta 1198 (2022), 339532, https://doi.org/10.1016/j.aca.2022.339532.

[20] V.V. Prasolov, Polynomials, Springer Berlin Heidelberg, Berlin, Heidelberg, 2004, https://doi.org/10.1007/978-3-642-03980-5.

[21] P.J. Rousseeuw, I. Ruts, J.W. Tukey, The Bagplot: A Bivariate Boxplot, 2022, p. 7.

[22] P. Nicola, General Competitive Equilibrium, in: Mainstream Mathematical Economics in the 20th Century, Springer Berlin Heidelberg, Berlin, Heidelberg, 2000, pp. 197–215, https://doi.org/10.1007/978-3-662-04238-0_16.

[23] E.B. Nilsen, S. Pedersen, J.D.C. Linnell, Can minimum convex polygon home ranges be used to draw biologically meaningful conclusions? Ecol. Res. 23 (2008) 635–639, https://doi.org/10.1007/s11284-007-0421-9.

[24] E. Rieffel, W. Polak, Quantum Computing: A Gentle Introduction, The MIT Press, Cambridge, Mass, 2011.

[25] C.B. Barber, D.P. Dobkin, H. Huhdanpaa, The quickhull algorithm for convex hulls, ACM Trans. Math. Softw. 22 (1996) 469–483, https://doi.org/10.1145/235815.235821.

[26] C. Marina-Montes, V. Motto-Ros, L.V. Pérez-Arribas, J. Anzano, M. Millán-Martínez, J.O. Cáceres, Aerosol analysis by micro laser-induced breakdown spectroscopy: a new protocol for particulate matter characterization in filters, Anal. Chim. Acta 1181 (2021), 338947, https://doi.org/10.1016/j.aca.2021.338947.

[27] J.O. Cáceres, F. Pelascini, V. Motto-Ros, S. Moncayo, F. Trichard, G. Panczer, A. Marín-Roldán, J.A. Cruz, I. Coronado, J. Martín-Chivelet, Megapixel multi-elemental imaging by laser-induced breakdown spectroscopy, a technology with considerable potential for paleoclimate studies, Sci. Rep. 7 (2017) 1–11, https://doi.org/10.1038/s41598-017-05437-3.

[28] L. Jolivet, V. Motto-Ros, L. Sorbier, T. Sozinho, C.-P. Lienemann, Quantitative imaging of carbon in heterogeneous refining catalysts, J. Anal. At. Spectrom. 35 (2020) 896–903, https://doi.org/10.1039/C9JA00434C.

Supplementary Material

The Matlab code of the IFF algorithm

```matlab
function [ind,freq] = iff(sp, num_randvect)

% Aim of the function: selection of the purest spectra in a dataset
%
% INPUTS
%   sp : the dataset you want to explore with spectra alongs the rows
%   num_randvect : number of randow vectors to be generated (should be higher
%   than 10000)
% OUTPUTS
%    ind: indexes of selected spectra (sorted by decreasing order of selection
frequency
%   freq : selection frequency of each spectrum in ind

%%%%%%%%%%%%%%%%%%%%%%%%%%%%%%%%%%%%%%%%%%%%%%%%%%%%%%%%%%%%%%%%%%%%%%%%%%%%%%
%% If you use this code in your research, please cite the reference:        %%
%% Qicheng Wu, César Marina-Montes, Jorge O. Cáceres, Jesús Anzano,         %%
%% Vincent Motto-Ros, Ludovic Duponchel, Interesting Features Finder (IFF): %%
%% another way to explore spectroscopic imaging datasets giving minor      %%
%% compounds and traces a chance to express themselves, Spectrochimica      %%
%% Acta B (2022).                                                           %%
%%%%%%%%%%%%%%%%%%%%%%%%%%%%%%%%%%%%%%%%%%%%%%%%%%%%%%%%%%%%%%%%%%%%%%%%%%%%%%

[li,co] = size(sp);

% Mean centering of the dataset
m = mean(sp);
sp_cent = sp - repmat(m,li,1);

% Generation of 'num_randvect' random vectors
randvect = 2*rand(num_randvect,co)-1;

% Initialization of the selection frequency list
votes = zeros(li, 1);

% Projection of all the data onto a random vector in the loop
h = waitbar(0,'Selection in progress...');
for k=1:num_randvect
    %disp(k)
     tmp = randvect(k,:)*sp_cent';
    [val, ind] = max(tmp);
    votes(ind,1) = votes(ind,1) + 1;
    [val, ind] = min(tmp);
    votes(ind,1) = votes(ind,1) + 1;
    waitbar(k / num_randvect)
end;
close(h);

%Sorting spectra in a decreasing order of frequency selection
[freq, ind] = sort(votes, 'descend');
```

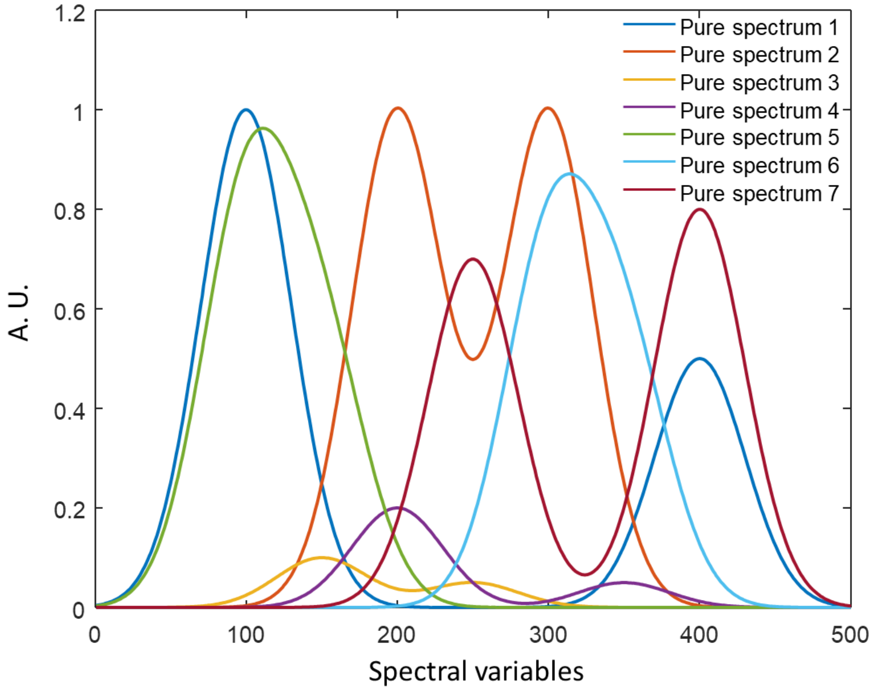

Figure 1S: the seven pure spectra used in the simulated dataset.

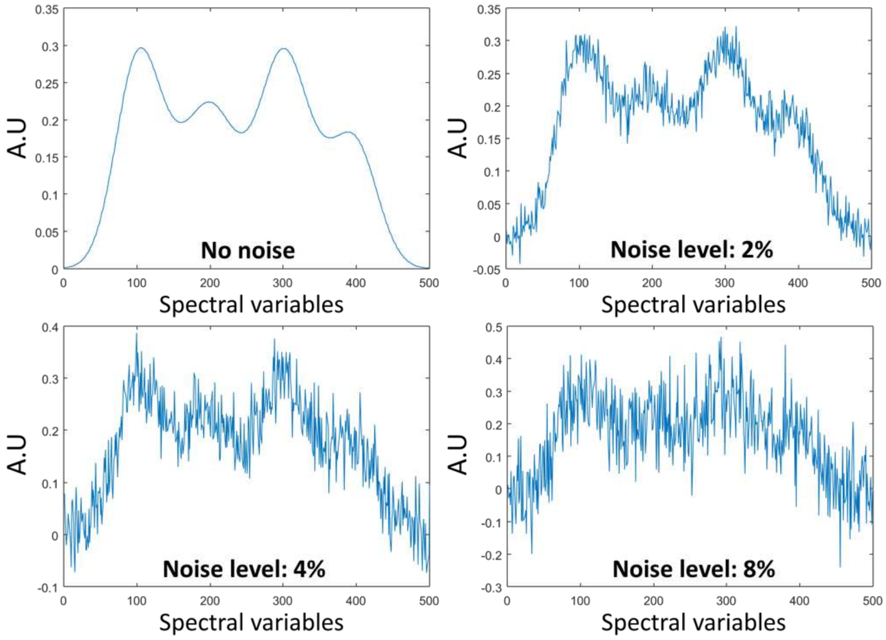

Figure 2S: an example of a spectrum of a mixture extracted from the dataset containing approximately the same concentration for the 7 elements as a function of the applied noise level.

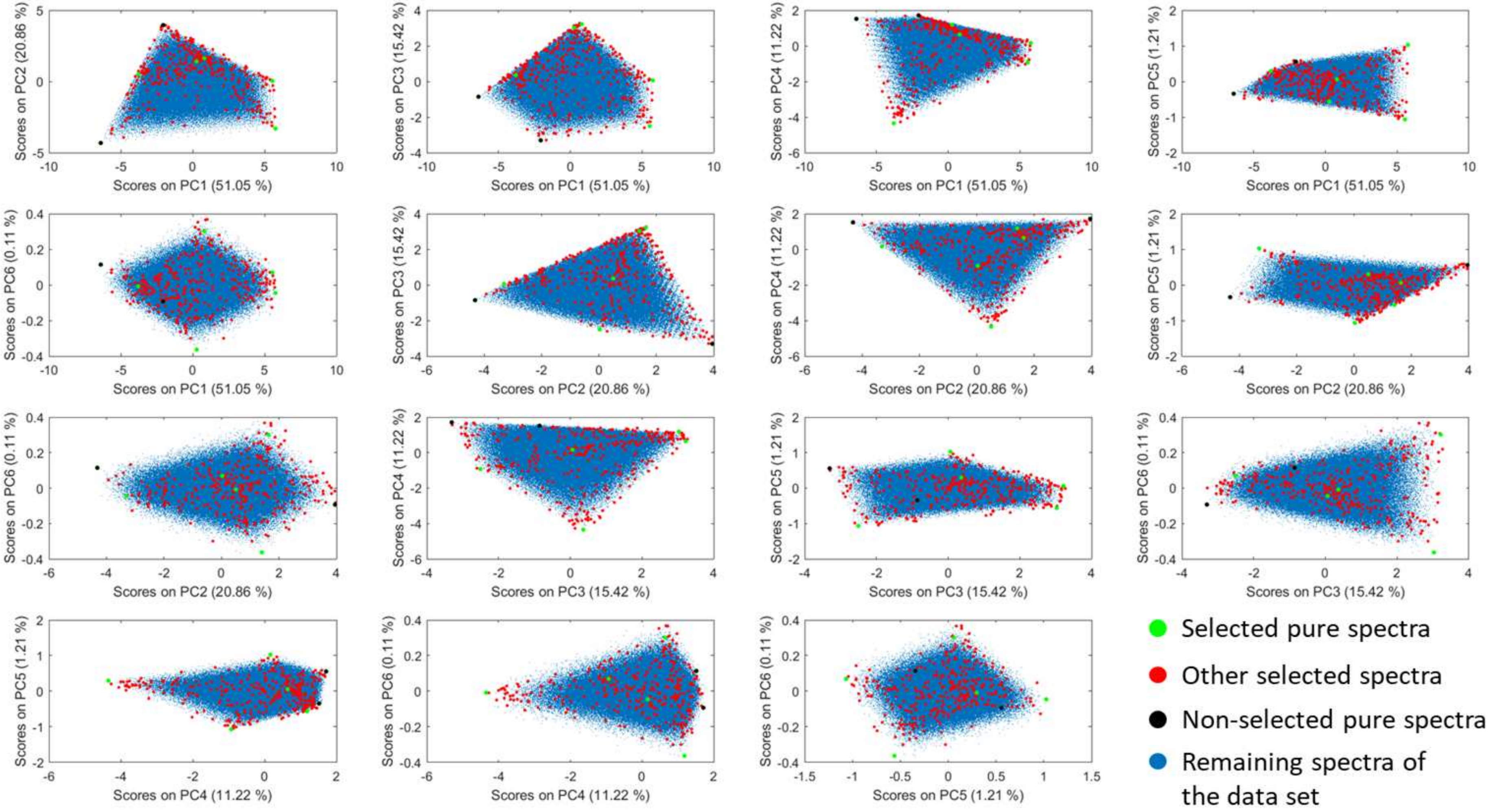

Figure 3S: representation of the pixels selected by ESP vs the rest of the dataset in a PCA space considering a 4% noise level.

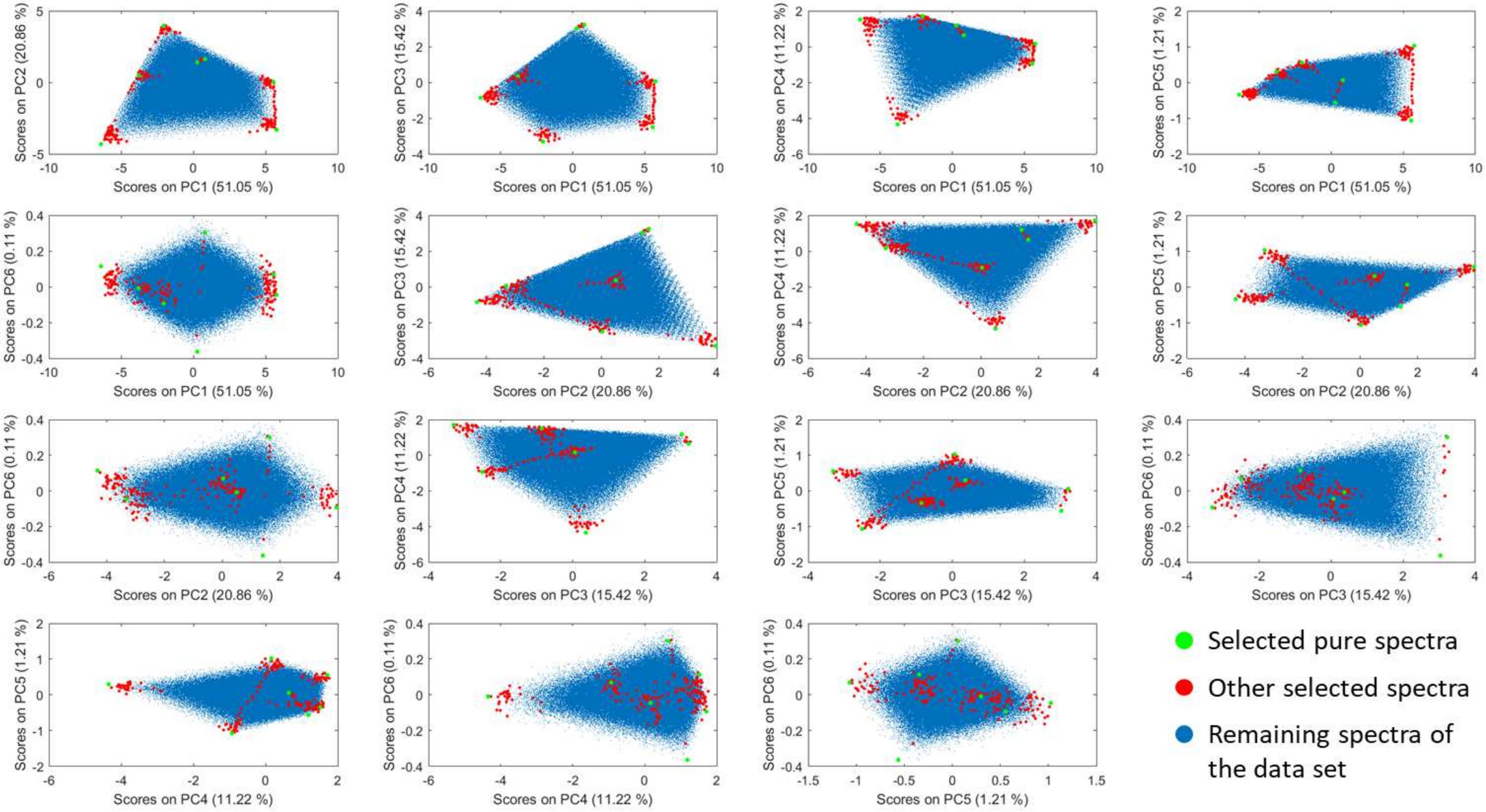

Figure 4S: representation of the pixels selected by IFF vs the rest of the dataset in a PCA space considering a 4% noise level.

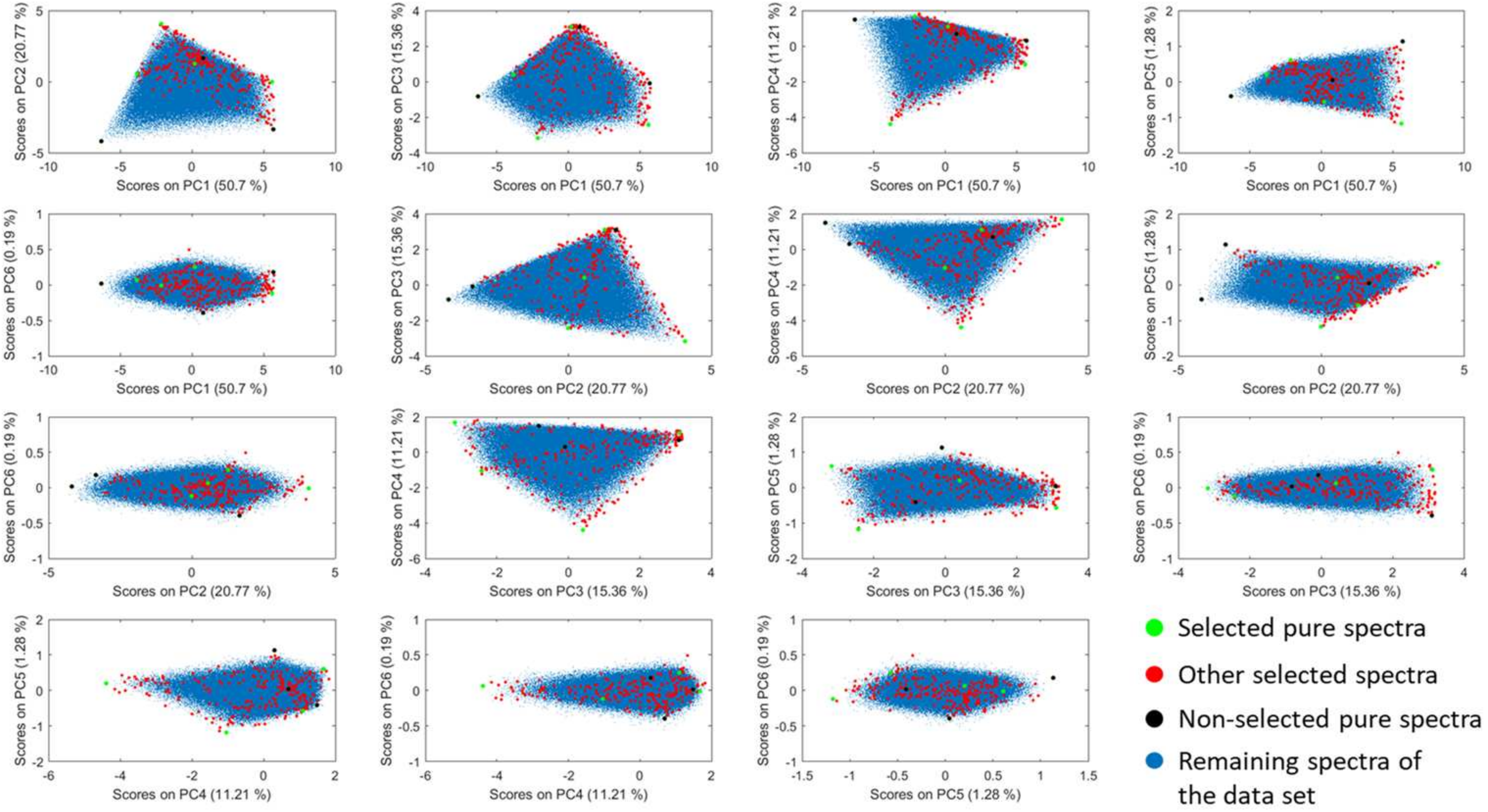

Figure 5S: representation of the pixels selected by ESP vs the rest of the dataset in a PCA space considering a 8% noise level.

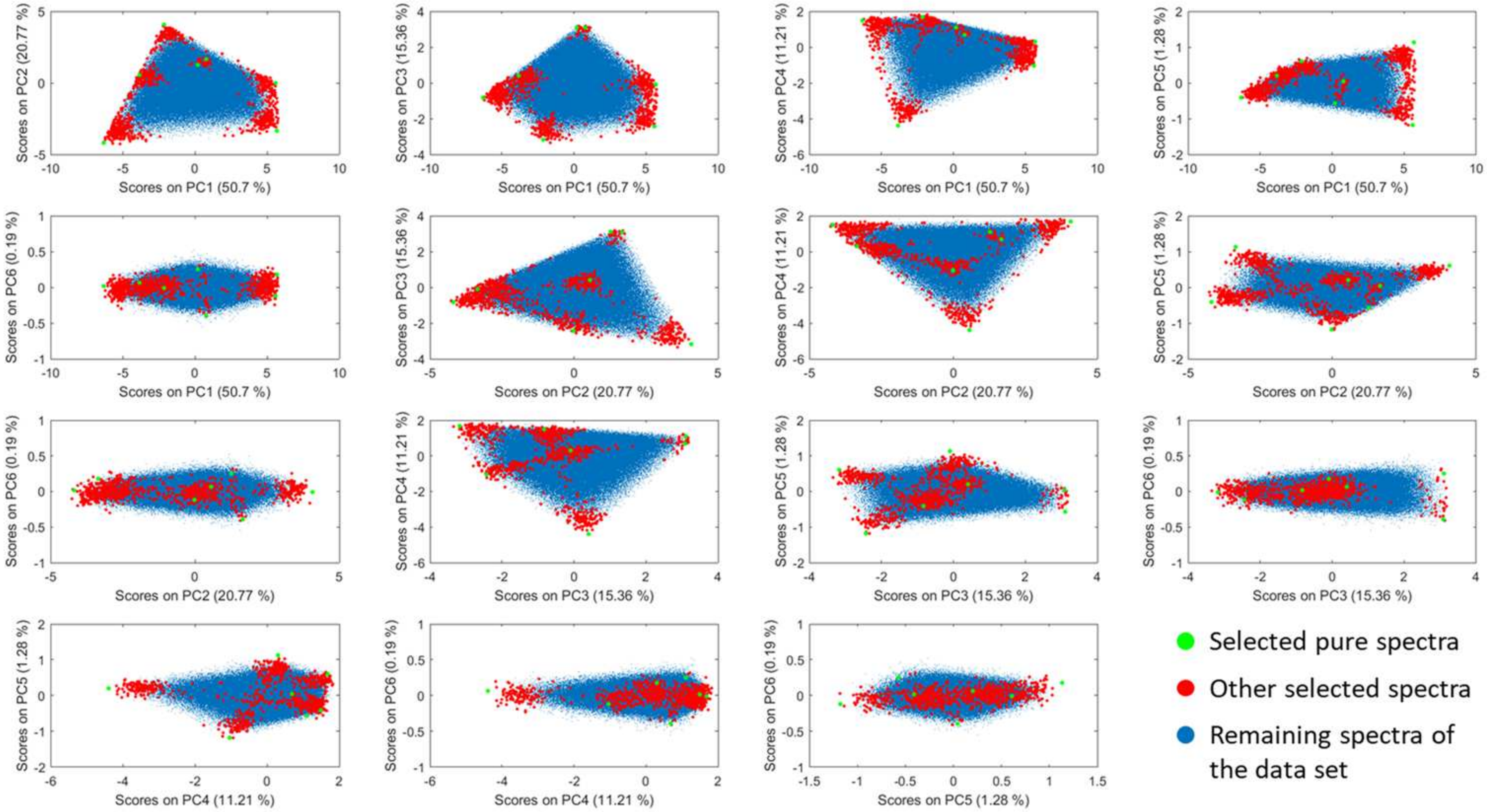

Figure 6S: representation of the pixels selected by IFF vs the rest of the dataset in a PCA space considering a 8% noise level.

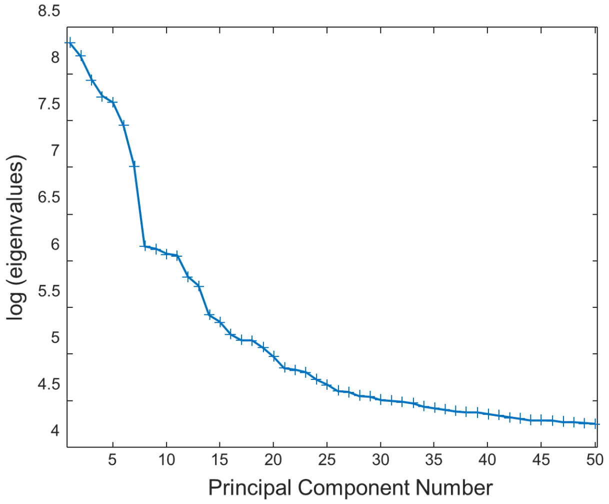

Figure 7S: Scree plot of eigenvalues.

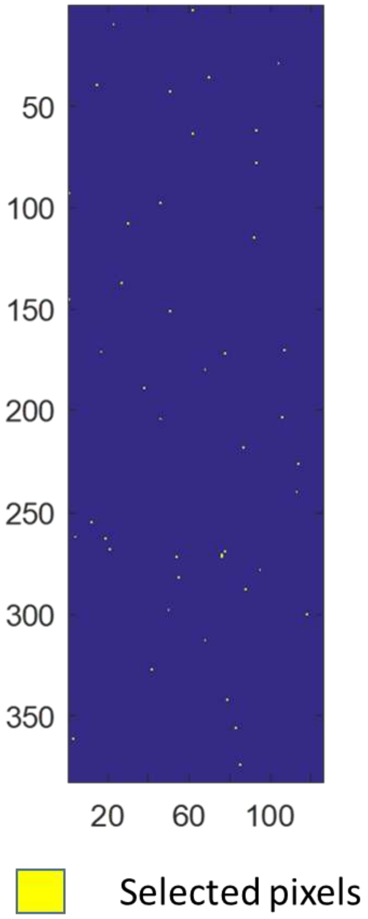

Figure 8S: Localization of selected pixels.

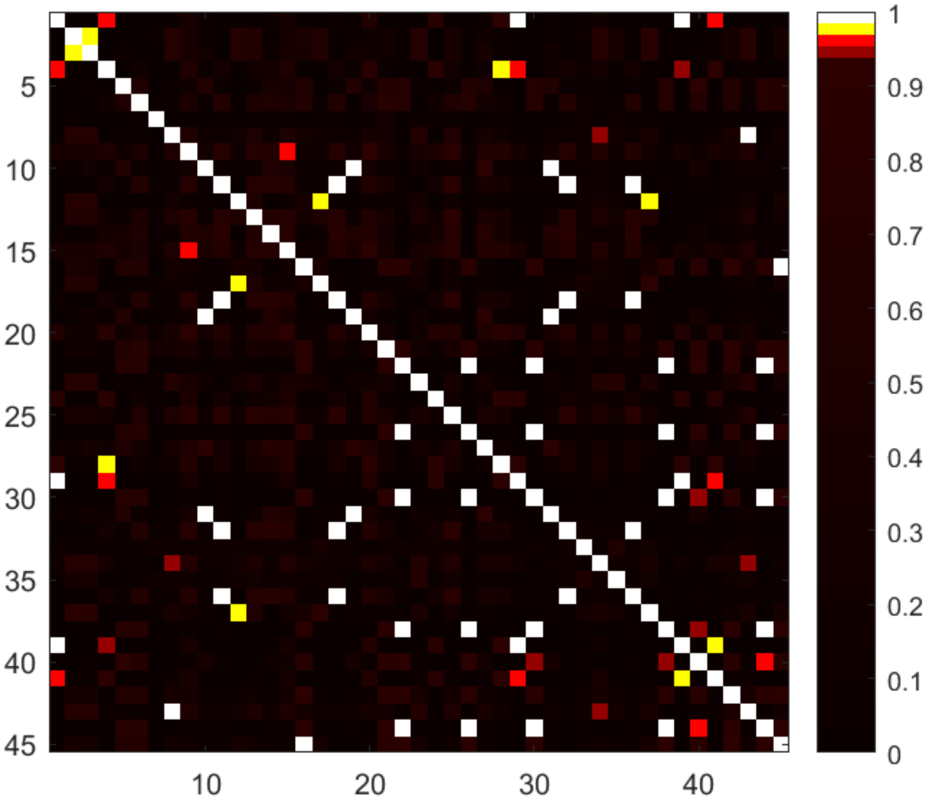

Figure 9S: the correlation matrix of the 45 selected spectra from IFF.

Table 1S: The list of the 45 selected pixels obtained from the IFF algorithm and their selection frequencies.

Spectrum index in the dataset	Selection frequency (/ 10000)	Spectrum index in the dataset	Selection frequency (/ 10000)	Spectrum index in the dataset	Selection frequency (/ 10000)
33905	2530	26157	288	1791	114
14706	1627	16372	255	33453	108
20901	1495	1508	180	11569	107
17777	1433	4840	179	29969	107
19399	1163	6666	173	32845	87
29304	1123	10452	170	29305	86
43407	1047	19526	160	30521	86
35605	965	528	159	21293	84
23688	695	32063	146	35260	83
19634	576	26777	138	43775	80
30066	505	7522	137	8291	75
45377	381	35589	117	17671	68
23749	369	8797	116	26290	67
40696	369	41045	115	36569	64
5771	366	476	114	39758	54

III.3. Conclusion and perspectives

With this chapter, we have demonstrated that the IFF approach allow us to select a short list of interesting pixels (potentially the purest ones) contained in LIBS imaging datasets whatever their explained variance. We thus answer the question posed since we have potentially access to the major and minor constituents and the traces. From an operational point of view, the calculations are done in a very reasonable time (a few minutes for the particle dataset) which is interesting but the calculation is also quite simple. The questions that arise now are how we might value the results of such an approach but also what the prospects might be. There are actually two ways of looking at this. First, if a researcher with little or no experience of chemometrics wishes to exploit the concept, he or she could systematically apply the IFF approach and then look at the spectra that have been selected. Being a specialist in LIBS spectroscopy, he/she will then be able to detect elements that are not expected and perhaps not visible on the mean spectrum of the considered dataset. It would then be possible to select a wavelength of the unsuspected element from which, by integrating the signal, a chemical map could be generated. Second, researchers with chemometrics skills could use this list of selected pixels in different ways but these remain proposals that need to be validated. This list of pixels should first help to evaluate the rank of the data matrices, i.e. the potential number of pure species present in the system. In the context of signal unmixing (such as MCR-ALS), it could also allow to generate better initial estimates of pure spectral profiles. This selection of pixels could also be seen as a compressed version of the original dataset. As a consequence, this would allow to use algorithms that are difficult to apply to datasets of several hundred thousand or even millions of spectra as other researchers in our team have already done in recent work [203].

GENERAL CONCLUSION

Since its birth, LIBS spectroscopy has come a long way. It is now used as a tool for characterizing complex materials in many industrial fields but also in all scientific fields. It is obvious that the Mars exploration has shed light on this technique, which was not known by all despite its formidable characteristics. Since the 2000s, LIBS imaging has also made a gigantic leap forward as we are now able to generate hyperspectral data cubes of several million spectra acquired in a few hours for a given sample at the micron scale spatial resolution. Over the past decade, LIBS imaging specialists have become aware that chemometrics tools can allow them to explore and exploit their data in different ways than traditional data analysis used on LIBS spectra. The LIBS imaging chemometrics publications now show that we can get a more comprehensive and less biased view of our complex samples. Nevertheless, LIBS imaging has specific characteristics that classical techniques such as vibrational spectroscopy do not have, the phenomenon of photon-matter interaction being from our point of view much more complex. It was clear that some classical chemometrics methods were not fully adapted to these characteristics and it was therefore the objective of this thesis to propose new chemometrics processing methodologies to overcome these obstacles. We therefore addressed two issues of interest to the LIBS community, namely proposing a method capable of making quantitative estimates of elements from the spectra independent of the temperature and electron density of the plasma but also proposing a new data processing strategy giving us a better chance of detecting minor elements and traces in complex samples. In order to answer the first problem, we implemented neural networks trained on simulated LIBS spectral data. This was a very long optimization phase with many pitfalls but we were able to answer the different problems posed throughout this thesis. Of course, this research does not stop here as the proposed neural networks are not yet optimal and their application to real LIBS imaging data needs to be studied further as new constraints have been raised. The second part of this thesis focused on the fact that current chemometric methods are poorly adapted to the detection of minor elements and traces in the LIBS spectra of complex samples. It is important to note that this is one of the strong points of LIBS spectroscopy, which has a very high dynamic range and therefore allows elemental contributions from % to ppm to appear in these spectra. We therefore understand that information on low concentration compounds is present in LIBS spectra but that we do not really have the tools to highlight them in a multivariate analysis approach. We have therefore implemented a strategy based on the mathematical concept of convex hull of the spectral dataset to overcome this problem. This research was also a success as it allowed us to demonstrate that we could detect spectra of some minor particles in an Antarctic sample that had not been detected with conventional chemometrics tools. In conclusion, both aspects of this thesis are undoubtedly hot topics in LIBS imaging. We are therefore convinced that this work will very soon be the beginning of many research projects focused on the improvement of these two concepts or even on their use in more global chemometrics methodologies.

REFERENCES

[1] T.O. Owolabi, M.A. Gondal, Development of hybrid extreme learning machine based chemo-metrics for precise quantitative analysis of LIBS spectra using internal reference pre-processing method, Anal. Chim. Acta. 1030 (2018) 33–41. https://doi.org/10.1016/j.aca.2018.05.029.

[2] R. Barbini, F. Colao, R. Fantoni, A. Palucci, S. Ribezzo, H.J.L. van der Steen, M. Angelone, Semi-quantitative time resolved LIBS measurements, Appl. Phys. B Lasers Opt. 65 (1997) 101–107. https://doi.org/10.1007/s003400050256.

[3] D.A. Hartzler, J.C. Jain, D.L. McIntyre, Development of a subsurface LIBS sensor for in situ groundwater quality monitoring with applications in CO2 leak sensing in carbon sequestration, Sci. Rep. 9 (2019) 4430. https://doi.org/10.1038/s41598-019-41025-3.

[4] S. Tzortzakis, D. Anglos, D. Gray, Ultraviolet laser filaments for remote laser-induced breakdown spectroscopy (LIBS) analysis: applications in cultural heritage monitoring, Opt. Lett. 31 (2006) 1139. https://doi.org/10.1364/OL.31.001139.

[5] R.R. Hark, L.J. East, Forensic Applications of LIBS, in: S. Musazzi, U. Perini (Eds.), Laser-Induc. Breakdown Spectrosc., Springer Berlin Heidelberg, Berlin, Heidelberg, 2014: pp. 377–420. https://doi.org/10.1007/978-3-642-45085-3_14.

[6] J.R. Almirall, S. Umpierrez, W. Castro, I. Gornushkin, J. Winefordner, Forensic elemental analysis of materials by laser induced breakdown spectroscopy (LIBS), in: E.M. Carapezza (Ed.), Orlando, Florida, USA, 2005: p. 657. https://doi.org/10.1117/12.605754.

[7] M.Z. Martin, N. Labbé, N. André, R. Harris, M. Ebinger, S.D. Wullschleger, A.A. Vass, High resolution applications of laser-induced breakdown spectroscopy for environmental and forensic applications, Spectrochim. Acta Part B At. Spectrosc. 62 (2007) 1426–1432. https://doi.org/10.1016/j.sab.2007.10.046.

[8] S.C. Jantzi, J.R. Almirall, Characterization and forensic analysis of soil samples using laser-induced breakdown spectroscopy (LIBS), Anal. Bioanal. Chem. 400 (2011) 3341–3351. https://doi.org/10.1007/s00216-011-4869-7.

[9] K.Y. Yamamoto, D.A. Cremers, M.J. Ferris, L.E. Foster, Detection of Metals in the Environment Using a Portable Laser-Induced Breakdown Spectroscopy Instrument, Appl. Spectrosc. 50 (1996) 222–233. https://doi.org/10.1366/0003702963906519.

[10] Russell.S. Harmon, F.C. De Lucia, A.W. Miziolek, K.L. McNesby, R.A. Walters, P.D. French, Laser-induced breakdown spectroscopy (LIBS) – an emerging field-portable sensor technology for real-time, ***in-situ*** geochemical and environmental analysis, Geochem. Explor. Environ. Anal. 5 (2005) 21–28. https://doi.org/10.1144/1467-7873/03-059.

[11] S. Pandhija, N.K. Rai, A.K. Rai, S.N. Thakur, Contaminant concentration in environmental samples using LIBS and CF-LIBS, Appl. Phys. B. 98 (2010) 231–241. https://doi.org/10.1007/s00340-009-3763-x.

[12] R.T. Wainner, R.S. Harmon, A.W. Miziolek, K.L. McNesby, P.D. French, Analysis of environmental lead contamination: comparison of LIBS field and laboratory instruments ઙ, At. Spectrosc. (2001) 17.

[13] X. Yu, Y. Li, X. Gu, J. Bao, H. Yang, L. Sun, Laser-induced breakdown spectroscopy application in environmental monitoring of water quality: a review, Environ. Monit. Assess. 186 (2014) 8969–8980. https://doi.org/10.1007/s10661-014-4058-1.

[14] M. Dell'Aglio, R. Gaudiuso, G.S. Senesi, A. De Giacomo, C. Zaccone, T.M. Miano, O. De Pascale, Monitoring of Cr, Cu, Pb, V and Zn in polluted soils by laser induced

breakdown spectroscopy (LIBS), J. Environ. Monit. 13 (2011) 1422. https://doi.org/10.1039/c0em00780c.

[15] L.F. Viana, Y.R. Súarez, C.A.L. Cardoso, S.M. Lima, L.H. da C. Andrade, S.E. Lima-Junior, Use of fish scales in environmental monitoring by the application of Laser-Induced Breakdown Spectroscopy (LIBS), Chemosphere. 228 (2019) 258–263. https://doi.org/10.1016/j.chemosphere.2019.04.070.

[16] K. Melessanaki, M. Mateo, S.C. Ferrence, P.P. Betancourt, D. Anglos, The application of LIBS for the analysis of archaeological ceramic and metal artifacts, Appl. Surf. Sci. 197–198 (2002) 156–163. https://doi.org/10.1016/S0169-4332(02)00459-2.

[17] A. Giakoumaki, K. Melessanaki, D. Anglos, Laser-induced breakdown spectroscopy (LIBS) in archaeological science—applications and prospects, Anal. Bioanal. Chem. 387 (2007) 749–760. https://doi.org/10.1007/s00216-006-0908-1.

[18] M.Z. Martin, N. Labbé, T.G. Rials, S.D. Wullschleger, Analysis of preservative-treated wood by multivariate analysis of laser-induced breakdown spectroscopy spectra, Spectrochim. Acta Part B At. Spectrosc. 60 (2005) 1179–1185. https://doi.org/10.1016/j.sab.2005.05.022.

[19] Z. Chen, H. Li, M. Liu, R. Li, Fast and sensitive trace metal analysis in aqueous solutions by laser-induced breakdown spectroscopy using wood slice substrates, Spectrochim. Acta Part B At. Spectrosc. 63 (2008) 64–68. https://doi.org/10.1016/j.sab.2007.11.010.

[20] J.R. Cordeiro, M.I.V. Martinez, R.W.C. Li, A.P. Cardoso, L.C. Nunes, F.J. Krug, T.R.L.C. Paixão, C.S. Nomura, J. Gruber, Identification of Four Wood Species by an Electronic Nose and by LIBS, Int. J. Electrochem. 2012 (2012) 1–5. https://doi.org/10.1155/2012/563939.

[21] X. Cui, Q. Wang, Y. Zhao, X. Qiao, G. Teng, Laser-induced breakdown spectroscopy (LIBS) for classification of wood species integrated with artificial neural network (ANN), Appl. Phys. B. 125 (2019) 56. https://doi.org/10.1007/s00340-019-7166-3.

[22] J. Kang, R. Li, Y. Wang, Y. Chen, Y. Yang, Ultrasensitive detection of trace amounts of lead in water by LIBS-LIF using a wood-slice substrate as a water absorber, J. Anal. At. Spectrom. 32 (2017) 2292–2299. https://doi.org/10.1039/C7JA00244K.

[23] H.M. Solo-Gabriele, T.G. Townsend, D.W. Hahn, T.M. Moskal, N. Hosein, J. Jambeck, G. Jacobi, Evaluation of XRF and LIBS technologies for on-line sorting of CCA-treated wood waste, Waste Manag. 24 (2004) 413–424. https://doi.org/10.1016/j.wasman.2003.09.006.

[24] N.K. Rai, A.K. Rai, LIBS—An efficient approach for the determination of Cr in industrial wastewater, J. Hazard. Mater. 150 (2008) 835–838. https://doi.org/10.1016/j.jhazmat.2007.10.044.

[25] D. Girón, T. Delgado, J. Ruiz, L.M. Cabalín, J.J. Laserna, In-situ monitoring and characterization of airborne solid particles in the hostile environment of a steel industry using stand-off LIBS, Measurement. 115 (2018) 1–10. https://doi.org/10.1016/j.measurement.2017.09.046.

[26] R. Kumar, A.K. Rai, D. Alamelu, S.K. Aggarwal, Monitoring of toxic elements present in sludge of industrial waste using CF-LIBS, Environ. Monit. Assess. 185 (2013) 171–180. https://doi.org/10.1007/s10661-012-2541-0.

[27] W.T.Y. Mohamed, Improved LIBS limit of detection of Be, Mg, Si, Mn, Fe and Cu in aluminum alloy samples using a portable Echelle spectrometer with ICCD camera, Opt. Laser Technol. 40 (2008) 30–38. https://doi.org/10.1016/j.optlastec.2007.04.004.

[28] M. Suchoňová, J. Krištof, M. Pribula, M. Veis, F.L. Tabarés, P. Veis, Analysis of LiSn alloy at several depths using LIBS, Fusion Eng. Des. 117 (2017) 175–179. https://doi.org/10.1016/j.fusengdes.2016.08.010.

[29] T.L. Thiem, R.H. Salter, J.A. Gardner, Y.I. Lee, J. Sneddon, Quantitative Simultaneous Elemental Determinations in Alloys Using Laser-Induced Breakdown Spectroscopy (LIBS) in an Ultra-High Vacuum, Appl. Spectrosc. 48 (1994) 58–64. https://doi.org/10.1366/0003702944027615.

[30] J.P. Castro, E.R. Pereira-Filho, Twelve different types of data normalization for the proposition of classification, univariate and multivariate regression models for the direct analyses of alloys by laser-induced breakdown spectroscopy (LIBS), J. Anal. At. Spectrom. 31 (2016) 2005–2014. https://doi.org/10.1039/C6JA00224B.

[31] H. Ji, Y. Ding, L. Zhang, Y. Hu, X. Zhong, Review of aerosol analysis by laser-induced breakdown spectroscopy, Appl. Spectrosc. Rev. (2020) 1–28. https://doi.org/10.1080/05704928.2020.1780604.

[32] G. Kim, K. Kim, H. Maeng, H. Lee, K. Park, Development of Aerosol-LIBS (Laser Induced Breakdown Spectroscopy) for Real-time Monitoring of Process-induced Particles, Aerosol Air Qual. Res. 19 (2019) 455–460. https://doi.org/10.4209/aaqr.2018.08.0312.

[33] A.N. Williams, S. Phongikaroon, Laser-Induced Breakdown Spectroscopy (LIBS) in a Novel Molten Salt Aerosol System, Appl. Spectrosc. 71 (2017) 744–749. https://doi.org/10.1177/0003702816648965.

[34] K. Park, G. Cho, J. Kwak, Development of an Aerosol Focusing-Laser Induced Breakdown Spectroscopy (Aerosol Focusing-LIBS) for Determination of Fine and Ultrafine Metal Aerosols, Aerosol Sci. Technol. 43 (2009) 375–386. https://doi.org/10.1080/02786820802662947.

[35] D.W. Hahn, M.M. Lunden, Detection and Analysis of Aerosol Particles by Laser-Induced Breakdown Spectroscopy, Aerosol Sci. Technol. 33 (2000) 30–48. https://doi.org/10.1080/027868200410831.

[36] L.J. Radziemski, D.A. Cremers, Laser-induced plasmas and applications, Marcel Dekker Inc, United States, 1989. http://inis.iaea.org/search/search.aspx?orig_q=RN:21088099.

[37] L.J. Radziemski, T.R. Loree, D.A. Cremers, Laser-Induced Breakdown Spectroscopy (LIBS): A New Spectrochemical Technique, in: D.K. Killinger, A. Mooradian (Eds.), Opt. Laser Remote Sens., Springer Berlin Heidelberg, Berlin, Heidelberg, 1983: pp. 303–307. https://doi.org/10.1007/978-3-540-39552-2_39.

[38] M. Casini, M. Harith, V. Palleschi, A. Salvetti, D. Singh, M. Vaselli, Detection of pollutants in air by Time-Resolved LIBS System, in: 1990: p. 1990.

[39] A. Ciucci, M. Corsi, V. Palleschi, S. Rastelli, A. Salvetti, E. Tognoni, New Procedure for Quantitative Elemental Analysis by Laser-Induced Plasma Spectroscopy, Appl. Spectrosc. 53 (1999) 960–964. https://doi.org/10.1366/0003702991947612.

[40] A.I. Whitehouse, J. Young, I.M. Botheroyd, S. Lawson, C.P. Evans, J. Wright, Remote material analysis of nuclear power station steam generator tubes by laser-induced breakdown spectroscopy, Spectrochim. Acta Part B At. Spectrosc. 56 (2001) 821–830. https://doi.org/10.1016/S0584-8547(01)00232-4.

[41] D.W. Hahn, N. Omenetto, Laser-Induced Breakdown Spectroscopy (LIBS), Part I: Review of Basic Diagnostics and Plasma– Particle Interactions: Still-Challenging Issues Within the Analytical Plasma Community, (n.d.) 32.

[42] R. Menzel, Photonics: linear and nonlinear interactions of laser light and matter, 2nd ed, Springer, Berlin ; New York, 2007.

[43] J.-L. Beduneau, Y. Ikeda, Spatial characterization of laser-induced sparks in air, J. Quant. Spectrosc. Radiat. Transf. 84 (2004) 123–139. https://doi.org/10.1016/S0022-4073(03)00136-5.

[44] E.A. Stefaniak, A. Worobiec, S. Potgieter-Vermaak, A. Alsecz, S. Török, R. Van Grieken, Molecular and elemental characterisation of mineral particles by means of

parallel micro-Raman spectrometry and Scanning Electron Microscopy/Energy Dispersive X-ray Analysis, Spectrochim. Acta Part B At. Spectrosc. 61 (2006) 824–830. https://doi.org/10.1016/j.sab.2006.04.009.

[45] S.G. Kazarian, K.L.A. Chan, Micro- and Macro-Attenuated Total Reflection Fourier Transform Infrared Spectroscopic Imaging: Plenary Lecture at the 5th International Conference on Advanced Vibrational Spectroscopy, 2009, Melbourne, Australia, Appl. Spectrosc. 64 (2010) 135A-152A. https://doi.org/10.1366/000370210791211673.

[46] K. Amponsah-Manager, N. Omenetto, B.W. Smith, I.B. Gornushkin, J.D. Winefordner, Microchip laser ablation of metals: investigation of the ablation process in view of its application to laser-induced breakdown spectroscopy, J. Anal. At. Spectrom. 20 (2005) 544. https://doi.org/10.1039/b419109a.

[47] M. Wälle, J. Koch, L. Flamigni, S. Heiroth, T. Lippert, W. Hartung, D. Günther, Detection efficiencies in nano- and femtosecond laser ablation inductively coupled plasma mass spectrometry, Spectrochim. Acta Part B At. Spectrosc. 64 (2009) 109–112. https://doi.org/10.1016/j.sab.2008.10.021.

[48] A. Vogel, V. Venugopalan, Mechanisms of Pulsed Laser Ablation of Biological Tissues, Chem. Rev. 103 (2003) 577–644. https://doi.org/10.1021/cr010379n.

[49] B. Sallé, C. Chaléard, V. Detalle, J.L. Lacour, P. Mauchien, C. Nouvellon, A. Semerok, Laser ablation efficiency of metal samples with UV laser nanosecond pulses, Appl. Surf. Sci. 138–139 (1999) 302–305. https://doi.org/10.1016/S0169-4332(98)00495-4.

[50] A. Semerok, C. Chaléard, V. Detalle, J.-L. Lacour, P. Mauchien, P. Meynadier, C. Nouvellon, B. Sallé, P. Palianov, M. Perdrix, G. Petite, Experimental investigations of laser ablation efficiency of pure metals with femto, pico and nanosecond pulses, Appl. Surf. Sci. 138–139 (1999) 311–314. https://doi.org/10.1016/S0169-4332(98)00411-5.

[51] P.W.J.M. Boumans, Sputtering in a glow discharge for spectrochemical analysis, Anal. Chem. 44 (1972) 1219–1228. https://doi.org/10.1021/ac60315a015.

[52] R. Fabbro, E. Fabre, F. Amiranoff, C. Garban-Labaune, J. Virmont, M. Weinfeld, C.E. Max, Laser-wavelength dependence of mass-ablation rate and heat-flux inhibition in laser-produced plasmas, Phys. Rev. A. 26 (1982) 2289–2292. https://doi.org/10.1103/PhysRevA.26.2289.

[53] T.J. Goldsack, J.D. Kilkenny, B.J. MacGowan, S.A. Veats, P.F. Cunningham, C.L.S. Lewis, M.H. Key, P.T. Rumsby, W.T. Toner, The variation of mass ablation rate with laser wavelength and target geometry, Opt. Commun. 42 (1982) 55–59. https://doi.org/10.1016/0030-4018(82)90089-X.

[54] F. Dahmani, Ablation scaling in laser-produced plasmas with laser intensity, laser wavelength, and target atomic number, Phys. Fluids B Plasma Phys. 4 (1992) 1585–1588. https://doi.org/10.1063/1.860067.

[55] R. Wennrich, K. Dittrich, U. Bonitz, Matrix interference in laser atomic absorption spectrometry, Spectrochim. Acta Part B At. Spectrosc. 39 (1984) 657–666. https://doi.org/10.1016/0584-8547(84)80152-4.

[56] J.-M. Gagne, P. Pianarosa, F. Lafleur, G. Perrault, Low-power continuous-wave laser atomisation for spectrochemical analysis, J. Anal. At. Spectrom. 3 (1988) 683. https://doi.org/10.1039/ja9880300683.

[57] C.R. Phipps, T.P. Turner, R.F. Harrison, G.W. York, W.Z. Osborne, G.K. Anderson, X.F. Corlis, L.C. Haynes, H.S. Steele, K.C. Spicochi, T.R. King, Impulse coupling to targets in vacuum by KrF, HF, and CO_2 single-pulse lasers, J. Appl. Phys. 64 (1988) 1083–1096. https://doi.org/10.1063/1.341867.

[58] R.H. Huddlestone, ed., Plasma diagnostic techniques, Acad. Press, New York, 1965.

[59] M. Capitelli, A. Casavola, G. Colonna, A. De Giacomo, Laser-induced plasma expansion: theoretical and experimental aspects, Spectrochim. Acta Part B At. Spectrosc. 59 (2004) 271–289. https://doi.org/10.1016/j.sab.2003.12.017.

[60] H.R. Griem, Validity of Local Thermal Equilibrium in Plasma Spectroscopy, Phys. Rev. 131 (1963) 1170–1176. https://doi.org/10.1103/PhysRev.131.1170.

[61] G. Cristoforetti, A. De Giacomo, M. Dell'Aglio, S. Legnaioli, E. Tognoni, V. Palleschi, N. Omenetto, Local Thermodynamic Equilibrium in Laser-Induced Breakdown Spectroscopy: Beyond the McWhirter criterion, Spectrochim. Acta Part B At. Spectrosc. 65 (2010) 86–95. https://doi.org/10.1016/j.sab.2009.11.005.

[62] C. Aragón, J.A. Aguilera, Characterization of laser induced plasmas by optical emission spectroscopy: A review of experiments and methods, Spectrochim. Acta Part B At. Spectrosc. 63 (2008) 893–916. https://doi.org/10.1016/j.sab.2008.05.010.

[63] J.A. Aguilera, C. Aragón, Characterization of a laser-induced plasma by spatially resolved spectroscopy of neutral atom and ion emissions., Spectrochim. Acta Part B At. Spectrosc. 59 (2004) 1861–1876. https://doi.org/10.1016/j.sab.2004.08.003.

[64] H.-Y. Moon, K.K. Herrera, N. Omenetto, B.W. Smith, J.D. Winefordner, On the usefulness of a duplicating mirror to evaluate self-absorption effects in laser induced breakdown spectroscopy, Spectrochim. Acta Part B At. Spectrosc. 64 (2009) 702–713. https://doi.org/10.1016/j.sab.2009.06.011.

[65] A.P. Thorne, A.P. Thorne, Spectrophysics, 2. ed, Chapman and Hall, London, 1988.

[66] C.T.J. Alkemade, ed., Metal vapours in flames, 1st ed, Pergamon Press, Oxford [Oxfordshire] ; New York, 1982.

[67] A.W. Miziolek, V. Palleschi, I. Schechter, eds., Laser-induced breakdown spectroscopy (LIBS): fundamentals and applications, Cambridge University Press, Cambridge, UK ; New York, 2006.

[68] P.W.J.M. Boumans, Theory of Spectrochemical Excitation, Springer US, Boston, MA, 1995. https://doi.org/10.1007/978-1-4684-8428-1.

[69] G.J. Bastiaans, R.A. Mangold, The calculation of electron density and temperature in Ar spectroscopic plasmas from continuum and line spectra, Spectrochim. Acta Part B At. Spectrosc. 40 (1985) 885–892. https://doi.org/10.1016/0584-8547(85)80059-8.

[70] A. Sola, M.D. Calzada, A. Gamero, On the use of the line-to-continuum intensity ratio for determining the electron temperature in a high-pressure argon surface-microwave discharge, J. Phys. Appl. Phys. 28 (1995) 1099–1110. https://doi.org/10.1088/0022-3727/28/6/012.

[71] H.C. Liu, X.L. Mao, J.H. Yoo, R.E. Russo, Early phase laser induced plasma diagnostics and mass removal during single-pulse laser ablation of silicon, Spectrochim. Acta Part B At. Spectrosc. 54 (1999) 1607–1624. https://doi.org/10.1016/S0584-8547(99)00092-0.

[72] J. Torres, J. Jonkers, M.J. van de Sande, J.J.A.M. van der Mullen, A. Gamero, A. Sola, An easy way to determine simultaneously the electron density and temperature in high-pressure plasmas by using Stark broadening, J. Phys. Appl. Phys. 36 (2003) L55–L59. https://doi.org/10.1088/0022-3727/36/13/101.

[73] J. Ashkenazy, R. Kipper, M. Caner, Spectroscopic measurements of electron density of capillary plasma based on Stark broadening of hydrogen lines, Phys. Rev. A. 43 (1991) 5568–5574. https://doi.org/10.1103/PhysRevA.43.5568.

[74] W. Lochte-Holtgreven, J. Richter, Plasma Diagnostics, North-Holland Publishing Company, 1968. https://books.google.fr/books?id=JiNRAAAAMAAJ.

[75] Y. Iida, Effects of atmosphere on laser vaporization and excitation processes of solid samples, Spectrochim. Acta Part B At. Spectrosc. 45 (1990) 1353–1367. https://doi.org/10.1016/0584-8547(90)80188-O.

[76] X.Z. Zhao, L.J. Shen, T.X. Lu, K. Niemax, Spatial distributions of electron density in microplasmas produced by laser ablation of solids, Appl. Phys. B Photophysics Laser Chem. 55 (1992) 327–330. https://doi.org/10.1007/BF00333075.

[77] I.B. Gornushkin, L.A. King, B.W. Smith, N. Omenetto, J.D. Winefordner, Line broadening mechanisms in the low pressure laser-induced plasma, Spectrochim. Acta Part B At. Spectrosc. 54 (1999) 1207–1217. https://doi.org/10.1016/S0584-8547(99)00064-6.

[78] Ş. Yalçin, D.R. Crosley, G.P. Smith, G.W. Faris, Influence of ambient conditions on the laser air spark, Appl. Phys. B Lasers Opt. 68 (1999) 121–130. https://doi.org/10.1007/s003400050596.

[79] J.M. de Regt, F.P.J. de Groote, J.A.M. van der Mullen, D.C. Schram, Comparison of active and passive spectroscopic methods to investigate atmospheric inductively coupled plasmas, Spectrochim. Acta Part B At. Spectrosc. 51 (1996) 1371–1383. https://doi.org/10.1016/0584-8547(96)01491-7.

[80] R.M. Measures, N. Drewell, P. Cardinal, Laser interaction based on resonance saturation (LIBORS): an alternative to inverse bremsstrahlung for coupling laser energy into a plasma, Appl. Opt. 18 (1979) 1824. https://doi.org/10.1364/AO.18.001824.

[81] C.G. Gill, A.W. Garrett, P.H. Hemberger, N.S. Nogar, Selective laser ablation/ionization for ion trap mass spectrometry: resonant laser ablation, Spectrochim. Acta Part B At. Spectrosc. 51 (1996) 851–862. https://doi.org/10.1016/0584-8547(96)01467-X.

[82] C. Goueguel, S. Laville, F. Vidal, M. Chaker, M. Sabsabi, Resonant laser-induced breakdown spectroscopy for analysis of lead traces in copper alloys, J. Anal. At. Spectrom. 26 (2011) 2452. https://doi.org/10.1039/c1ja10112a.

[83] R.C. Wiens, R.E. Arvidson, D.A. Cremers, M.J. Ferris, J.D. Blacic, F.P. Seelos, K.S. Deal, Combined remote mineralogical and elemental identification from rovers: Field and laboratory tests using reflectance and laser-induced breakdown spectroscopy: IDENTIFICATION USING REFLECTANCE AND LIBS, J. Geophys. Res. Planets. 107 (2002) FIDO 3-1-FIDO 3-14. https://doi.org/10.1029/2000JE001439.

[84] A. Cousin, O. Forni, S. Maurice, O. Gasnault, C. Fabre, V. Sautter, R.C. Wiens, J. Mazoyer, Laser induced breakdown spectroscopy library for the Martian environment, Spectrochim. Acta Part B At. Spectrosc. 66 (2011) 805–814. https://doi.org/10.1016/j.sab.2011.10.004.

[85] M. Dong, J. Lu, S. Yao, Z. Zhong, J. Li, J. Li, W. Lu, Experimental study on the characteristics of molecular emission spectroscopy for the analysis of solid materials containing C and N, Opt. Express. 19 (2011) 17021. https://doi.org/10.1364/OE.19.017021.

[86] V. Lazic, A. Palucci, S. Jovicevic, M. Carpanese, Detection of explosives in traces by laser induced breakdown spectroscopy: Differences from organic interferents and conditions for a correct classification, Spectrochim. Acta Part B At. Spectrosc. 66 (2011) 644–655. https://doi.org/10.1016/j.sab.2011.07.003.

[87] I. Gobernado-Mitre, A.C. Prieto, V. Zafiropulos, Y. Spetsidou, C. Fotakis, On-Line Monitoring of Laser Cleaning of Limestone by Laser-Induced Breakdown Spectroscopy and Laser-Induced Fluorescence, Appl. Spectrosc. 51 (1997) 1125–1129. https://doi.org/10.1366/0003702971941944.

[88] M.F. Alberghina, R. Barraco, M. Brai, T. Schillaci, L. Tranchina, Integrated analytical methodologies for the study of corrosion processes in archaeological bronzes, Spectrochim. Acta Part B At. Spectrosc. 66 (2011) 129–137. https://doi.org/10.1016/j.sab.2010.12.010.

[89] M. Gatti, V. Palleschi, A. Salvetti, D.P. Singh, M. Vaselli, Spherical shock waves in laser produced plasmas in gas, Opt. Commun. 69 (1988) 141–146. https://doi.org/10.1016/0030-4018(88)90299-4.

[90] L.M. Cabalín, J.J. Laserna, Atomic emission spectroscopy of laser-induced plasmas generated with an annular-shaped laser beam, J Anal Spectrom. 19 (2004) 445–450. https://doi.org/10.1039/B315856J.

[91] K.T. Rodolfa, D.A. Cremers, Capabilities of Surface Composition Analysis Using a Long Laser-Induced Breakdown Spectroscopy Spark, Appl. Spectrosc. 58 (2004) 367–375. https://doi.org/10.1366/000370204773580185.

[92] V. Lednev, S.M. Pershin, A.F. Bunkin, Laser beam profile influence on LIBS analytical capabilities: single vs. multimode beam, J. Anal. At. Spectrom. 25 (2010) 1745. https://doi.org/10.1039/c0ja00017e.

[93] C. Gallou, J.B. Sirven, Plasma Emission Collection for Characterization and Analytical Optimization, (2007).

[94] D.W. Hahn, N. Omenetto, Laser-Induced Breakdown Spectroscopy (LIBS), Part II: Review of Instrumental and Methodological Approaches to Material Analysis and Applications to Different Fields, Appl. Spectrosc. 66 (2012) 347–419. https://doi.org/10.1366/11-06574.

[95] J. van Dijk, G.M.W. Kroesen, A. Bogaerts, Plasma modelling and numerical simulation, J. Phys. Appl. Phys. 42 (2009) 190301. https://doi.org/10.1088/0022-3727/42/19/190301.

[96] A. Bogaerts, M. Aghaei, D. Autrique, H. Lindner, Z.Y. Chen, W. Wendelen, Computer Simulations of Laser Ablation, Plume Expansion and Plasma Formation, Adv. Mater. Res. 227 (2011) 1–10. https://doi.org/10.4028/www.scientific.net/AMR.227.1.

[97] I.B. Gornushkin, U. Panne, Radiative models of laser-induced plasma and pump-probe diagnostics relevant to laser-induced breakdown spectroscopy, Spectrochim. Acta Part B At. Spectrosc. 65 (2010) 345–359. https://doi.org/10.1016/j.sab.2010.03.021.

[98] J.M. Mermet, P. Mauchien, J.L. Lacour, Processing of shot-to-shot raw data to improve precision in laser-induced breakdown spectrometry microprobe, Spectrochim. Acta Part B At. Spectrosc. 63 (2008) 999–1005. https://doi.org/10.1016/j.sab.2008.06.003.

[99] R.D. Cowan, G.H. Dieke, Self-Absorption of Spectrum Lines, Rev. Mod. Phys. 20 (1948) 418–455. https://doi.org/10.1103/RevModPhys.20.418.

[100] D.M.D. Pace, C.A. D'Angelo, G. Bertuccelli, Calculation of Optical Thicknesses of Magnesium Emission Spectral Lines for Diagnostics of Laser-Induced Plasmas, Appl. Spectrosc. 65 (2011) 1202–1212. https://doi.org/10.1366/11-06348.

[101] N. Omenetto, J.D. Winefordner, C.Th.J. Alkemade, An expression for the atomic fluorescence and thermal-emission intensity under conditions of near saturation and arbitrary self-absorption, Spectrochim. Acta Part B At. Spectrosc. 30 (1975) 335–341. https://doi.org/10.1016/0584-8547(75)80031-0.

[102] J.-M. Mermet, Calibration in atomic spectrometry: A tutorial review dealing with quality criteria, weighting procedures and possible curvatures, Spectrochim. Acta Part B At. Spectrosc. 65 (2010) 509–523. https://doi.org/10.1016/j.sab.2010.05.007.

[103] E. Voigtman, Limits of detection and decision. Part 1, Spectrochim. Acta Part B At. Spectrosc. 63 (2008) 115–128. https://doi.org/10.1016/j.sab.2007.11.015.

[104] W. Lee, J. Wu, Y. Lee, J. Sneddon, Recent Applications of Laser-Induced Breakdown Spectrometry: A Review of Material Approaches, Appl. Spectrosc. Rev. 39 (2004) 27–97. https://doi.org/10.1081/ASR-120028868.

[105] M. Thompson, S.L.R. Ellison, A review of interference effects and their correction in chemical analysis with special reference to uncertainty, Accreditation Qual. Assur. 10 (2005) 82–97. https://doi.org/10.1007/s00769-004-0871-5.

[106] W.B. Barnett, V.A. Fassel, R.N. Kniseley, Theoretical principles of internal standardization in analytical emission spectroscopy, Spectrochim. Acta Part B At. Spectrosc. 23 (1968) 643–664. https://doi.org/10.1016/0584-8547(68)80045-X.

[107] N.B. Zorov, A.A. Gorbatenko, T.A. Labutin, A.M. Popov, A review of normalization techniques in analytical atomic spectrometry with laser sampling: From single to multivariate correction, Spectrochim. Acta Part B At. Spectrosc. 65 (2010) 642–657. https://doi.org/10.1016/j.sab.2010.04.009.

[108] A.M. Leach, G.M. Hieftje, Methods for shot-to-shot normalization in laser ablation with an inductively coupled plasma time-of-flight mass spectrometer, J. Anal. At. Spectrom. 15 (2000) 1121–1124. https://doi.org/10.1039/b001968m.

[109] J.A. Aguilera, C. Aragón, V. Madurga, J. Manrique, Study of matrix effects in laser induced breakdown spectroscopy on metallic samples using plasma characterization by emission spectroscopy, Spectrochim. Acta Part B At. Spectrosc. 64 (2009) 993–998. https://doi.org/10.1016/j.sab.2009.07.007.

[110] J.D. Winefordner, I.B. Gornushkin, T. Correll, E. Gibb, B.W. Smith, N. Omenetto, Comparing several atomic spectrometric methods to the super stars: special emphasis on laser induced breakdown spectrometry, LIBS, a future super star, J. Anal. At. Spectrom. 19 (2004) 1061. https://doi.org/10.1039/b400355c.

[111] L. De Galan, G.F. Samaey, The possibility of absolute atomic absorption and atomic emission flame spectrometric analysis, Anal. Chim. Acta. 50 (1970) 39–50. https://doi.org/10.1016/S0003-2670(00)80925-3.

[112] B.V. L'vov, Electrothermal atomization—the way toward absolute methods of atomic absorption analysis, Spectrochim. Acta Part B At. Spectrosc. 33 (1978) 153–193. https://doi.org/10.1016/0584-8547(78)80039-1.

[113] W. Slavin, G.R. Carnrick, The possibility of standardless furnace atomic absorption spectroscopy, Spectrochim. Acta Part B At. Spectrosc. 39 (1984) 271–282. https://doi.org/10.1016/0584-8547(84)80035-X.

[114] N. Omenetto, Laser-induced fluorescence in a furnace: A viable approach to absolute analysis?, Mikrochim. Acta. 104 (1991) 277–285. https://doi.org/10.1007/BF01245515.

[115] J.-L. Pouchou, Standardless X-ray analysis of bulk specimens, Mikrochim. Acta. 114–115 (1994) 33–52. https://doi.org/10.1007/BF01244532.

[116] D.E. Newbury, C.R. Swyt, R.L. Myklebust, "Standardless" Quantitative Electron Probe Microanalysis with Energy-Dispersive X-ray Spectrometry: Is It Worth the Risk?, Anal. Chem. 67 (1995) 1866–1871. https://doi.org/10.1021/ac00107a017.

[117] Q. Yu, R. Huang, L. Li, L. Lin, W. Hang, J. He, B. Huang, Applicability of Standardless Semiquantitative Analysis of Solids by High-Irradiance Laser Ionization Orthogonal Time-of-Fight Mass Spectrometry, Anal. Chem. 81 (2009) 4343–4348. https://doi.org/10.1021/ac900141z.

[118] A. Hulanicki, Absolute methods in analytical chemistry (Technical Report), Pure Appl. Chem. 67 (1995) 1905–1911. https://doi.org/10.1351/pac199567111905.

[119] K.K. Herrera, E. Tognoni, N. Omenetto, B.W. Smith, J.D. Winefordner, Semi-quantitative analysis of metal alloys, brass and soil samples by calibration-free laser-induced breakdown spectroscopy: recent results and considerations, J. Anal. At. Spectrom. 24 (2009) 413. https://doi.org/10.1039/b820493d.

[120] E. Tognoni, G. Cristoforetti, S. Legnaioli, V. Palleschi, Calibration-Free Laser-Induced Breakdown Spectroscopy: State of the art, Spectrochim. Acta Part B At. Spectrosc. 65 (2010) 1–14. https://doi.org/10.1016/j.sab.2009.11.006.

[121] T.S. West, E.J. Bowen, Reviews of books, Trans. Faraday Soc. 65 (1969) 1952. https://doi.org/10.1039/tf9696501952.

[122] N. Omenetto, ed., Analytical laser spectroscopy, Wiley, New York, 1979.

[123] J. Uebbing, J. Brust, W. Sdorra, F. Leis, K. Niemax, Reheating of a Laser-Produced Plasma by a Second Pulse Laser, Appl. Spectrosc. 45 (1991) 1419–1423. https://doi.org/10.1366/0003702914335445.

[124] A. De Giacomo, M. Dell'Aglio, D. Bruno, R. Gaudiuso, O. De Pascale, Experimental and theoretical comparison of single-pulse and double-pulse laser induced breakdown spectroscopy on metallic samples, Spectrochim. Acta Part B At. Spectrosc. 63 (2008) 805–816. https://doi.org/10.1016/j.sab.2008.05.002.

[125] R. Sattmann, V. Sturm, R. Noll, Laser-induced breakdown spectroscopy of steel samples using multiple Q-switch Nd:YAG laser pulses, J. Phys. Appl. Phys. 28 (1995) 2181–2187. https://doi.org/10.1088/0022-3727/28/10/030.

[126] V. Sturm, R. Sattmann, R. Noll, Optical fiber transmission of multipleQ-switch Nd: YAG laser pulses with microsecond interpulse separations, Appl. Phys. B Laser Opt. 63 (1996) 363–370. https://doi.org/10.1007/BF01828739.

[127] V. Sturm, J. Vrenegor, R. Noll, M. Hemmerlin, Bulk analysis of steel samples with surface scale layers by enhanced laser ablation and LIBS analysis of C, P, S, Al, Cr, Cu, Mn and Mo, J. Anal. At. Spectrom. 19 (2004) 451. https://doi.org/10.1039/b315637k.

[128] G. Galbács, N. Jedlinszki, G. Cseh, Z. Galbács, L. Túri, Accurate quantitative analysis of gold alloys using multi-pulse laser induced breakdown spectroscopy and a correlation-based calibration method, Spectrochim. Acta Part B At. Spectrosc. 63 (2008) 591–597. https://doi.org/10.1016/j.sab.2008.03.001.

[129] N. Jedlinszki, G. Galbács, An evaluation of the analytical performance of collinear multi-pulse laser induced breakdown spectroscopy, Microchem. J. 97 (2011) 255–263. https://doi.org/10.1016/j.microc.2010.09.009.

[130] G. Galbács, V. Budavári, Z. Geretovszky, Multi-pulse laser-induced plasma spectroscopy using a single laser source and a compact spectrometer, J. Anal. At. Spectrom. 20 (2005) 974. https://doi.org/10.1039/b504373e.

[131] R. García, A. Báez, Atomic absorption spectrometry (AAS), At. Absorpt. Spectrosc. 1 (2012) 1–13.

[132] K.F. Khan, Application, principle and operation of ICP-OES in pharmaceutical analysis, (n.d.) 3.

[133] F. Lia, M. Zammit Mangion, C. Farrugia, Application of Elemental Analysis via Energy Dispersive X-ray Fluorescence (ED-XRF) for the Authentication of Maltese Extra Virgin Olive Oil, Agriculture. 10 (2020) 71. https://doi.org/10.3390/agriculture10030071.

[134] J.A.M. Vrielink, R.M. Tiggelaar, J.G.E. Gardeniers, L. Lefferts, Applicability of X-ray fluorescence spectroscopy as method to determine thickness and composition of stacks of metal thin films: A comparison with imaging and profilometry, Thin Solid Films. 520 (2012) 1740–1744. https://doi.org/10.1016/j.tsf.2011.08.049.

[135] M. Alfeld, W. De Nolf, S. Cagno, K. Appel, D.P. Siddons, A. Kuczewski, K. Janssens, J. Dik, K. Trentelman, M. Walton, A. Sartorius, Revealing hidden paint layers in oil paintings by means of scanning macro-XRF: a mock-up study based on Rembrandt's "An old man in military costume," J Anal Spectrom. 28 (2013) 40–51. https://doi.org/10.1039/C2JA30119A.

[136] S.K. Hussain Shah, J. Iqbal, P. Ahmad, M.U. Khandaker, S. Haq, M. Naeem, Laser induced breakdown spectroscopy methods and applications: A comprehensive review, Radiat. Phys. Chem. 170 (2020) 108666. https://doi.org/10.1016/j.radphyschem.2019.108666.

[137] S.D. Brown, T.B. Blank, S.T. Sum, L.G. Weyer, Chemometrics, Anal. Chem. 66 (1994) 315–359. https://doi.org/10.1021/ac00084a014.

[138] G. Kim, J. Kwak, J. Choi, K. Park, Detection of Nutrient Elements and Contamination by Pesticides in Spinach and Rice Samples Using Laser-Induced Breakdown Spectroscopy (LIBS), J. Agric. Food Chem. 60 (2012) 718–724. https://doi.org/10.1021/jf203518f.

[139] M.G. Nespeca, A.L. Vieira, D.S. Júnior, J.A.G. Neto, E.C. Ferreira, Detection and quantification of adulterants in honey by LIBS, Food Chem. 311 (2020) 125886. https://doi.org/10.1016/j.foodchem.2019.125886.

[140] K. Liu, D. Tian, X. Deng, H. Wang, G. Yang, Rapid classification of plastic bottles by laser-induced breakdown spectroscopy (LIBS) coupled with partial least squares discrimination analysis based on spectral windows (SW-PLS-DA), J. Anal. At. Spectrom. 34 (2019) 1665–1671. https://doi.org/10.1039/C9JA00105K.

[141] A.K. Myakalwar, S. Sreedhar, I. Barman, N.C. Dingari, S. Venugopal Rao, P. Prem Kiran, S.P. Tewari, G. Manoj Kumar, Laser-induced breakdown spectroscopy-based investigation and classification of pharmaceutical tablets using multivariate chemometric analysis, Talanta. 87 (2011) 53–59. https://doi.org/10.1016/j.talanta.2011.09.040.

[142] P. Pease, V. Tchakerian, Source provenance of carbonate grains in the Wahiba Sand Sea, Oman, using a new LIBS method, Aeolian Res. 15 (2014) 203–216. https://doi.org/10.1016/j.aeolia.2014.06.001.

[143] V.C. Costa, F.W.B. Aquino, C.M. Paranhos, E.R. Pereira-Filho, Identification and classification of polymer e-waste using laser-induced breakdown spectroscopy (LIBS) and chemometric tools, Polym. Test. 59 (2017) 390–395. https://doi.org/10.1016/j.polymertesting.2017.02.017.

[144] D. Pokrajac, A. Lazarevic, V. Kecman, A. Marcano, Y. Markushin, T. Vance, N. Reljin, S. McDaniel, N. Melikechi, Automatic Classification of Laser-Induced Breakdown Spectroscopy (LIBS) Data of Protein Biomarker Solutions, Appl. Spectrosc. 68 (2014) 1067–1075. https://doi.org/10.1366/14-07488.

[145] A.M. Neiva, M.A. Chagas Jacinto, M. Mello de Alencar, S.N. Esteves, E.R. Pereira-Filho, Proposition of classification models for the direct evaluation of the quality of cattle and sheep leathers using laser-induced breakdown spectroscopy (LIBS) analysis, RSC Adv. 6 (2016) 104827–104838. https://doi.org/10.1039/C6RA22337K.

[146] N.C. Dingari, I. Barman, A.K. Myakalwar, S.P. Tewari, M. Kumar Gundawar, Incorporation of Support Vector Machines in the LIBS Toolbox for Sensitive and Robust Classification Amidst Unexpected Sample and System Variability, Anal. Chem. 84 (2012) 2686–2694. https://doi.org/10.1021/ac202755e.

[147] K.-Q. Yu, Y.-R. Zhao, F. Liu, Y. He, Laser-Induced Breakdown Spectroscopy Coupled with Multivariate Chemometrics for Variety Discrimination of Soil, Sci. Rep. 6 (2016) 27574. https://doi.org/10.1038/srep27574.

[148] G. Vítková, K. Novotný, L. Prokeš, A. Hrdlička, J. Kaiser, J. Novotný, R. Malina, D. Prochazka, Fast identification of biominerals by means of stand-off laser-induced breakdown spectroscopy using linear discriminant analysis and artificial neural networks, Spectrochim. Acta Part B At. Spectrosc. 73 (2012) 1–6. https://doi.org/10.1016/j.sab.2012.05.010.

[149] L. Sheng, T. Zhang, G. Niu, K. Wang, H. Tang, Y. Duan, H. Li, Classification of iron ores by laser-induced breakdown spectroscopy (LIBS) combined with random forest (RF), J. Anal. At. Spectrom. 30 (2015) 453–458. https://doi.org/10.1039/C4JA00352G.

[150] Q.-S. Sun, S.-G. Zeng, Y. Liu, P.-A. Heng, D.-S. Xia, A new method of feature fusion and its application in image recognition, Pattern Recognit. 38 (2005) 2437–2448. https://doi.org/10.1016/j.patcog.2004.12.013.

[151] S. Desai, E.V. Raghavendra, B. Yegnanarayana, A.W. Black, K. Prahallad, Voice conversion using Artificial Neural Networks, in: 2009 IEEE Int. Conf. Acoust. Speech Signal Process., IEEE, Taipei, Taiwan, 2009: pp. 3893–3896. https://doi.org/10.1109/ICASSP.2009.4960478.

[152] B-Tech, Vellore Institute of Technology, Vellore, India., D. Datta, P.E. David, Assistant Professor (Sr. Grade), Vellore Institute of Technology, Vellore, India, D. Mittal, B-Tech, Vellore Institute of Technology, Vellore, India., A. Jain, B-Tech, Vellore Institute of Technology, Vellore, India., Neural Machine Translation using Recurrent Neural Network, Int. J. Eng. Adv. Technol. 9 (2020) 1395–1400. https://doi.org/10.35940/ijeat.D7637.049420.

[153] F. Amato, A. López, E.M. Peña-Méndez, P. Vaňhara, A. Hampl, J. Havel, Artificial neural networks in medical diagnosis, J. Appl. Biomed. 11 (2013) 47–58. https://doi.org/10.2478/v10136-012-0031-x.

[154] N. Omar, Z. ‘Amirah Johari, M. Smith, Predicting fraudulent financial reporting using artificial neural network, J. Financ. Crime. 24 (2017) 362–387. https://doi.org/10.1108/JFC-11-2015-0061.

[155] R. Sattmann, I.M. Nch, H. Krause, R. Noll, S. Couris, A. Hatziapostolou, A. Mavromanolakis, C. Fotakis, E. Larrauri, R. Miguel, Laser-Induced Breakdown Spectroscopy for Polymer Identi® cation, (n.d.) 6.

[156] M. Boueri, V. Motto-Ros, W.-Q. Lei, Q.-L. Ma, L.-J. Zheng, H.-P. Zeng, J. Yu, Identification of Polymer Materials Using Laser-Induced Breakdown Spectroscopy Combined with Artificial Neural Networks, Appl. Spectrosc. 65 (2011) 307–314. https://doi.org/10.1366/10-06079a.

[157] A. Ramil, A.J. López, A. Yáñez, Application of artificial neural networks for the rapid classification of archaeological ceramics by means of laser induced breakdown spectroscopy (LIBS), Appl. Phys. A. 92 (2008) 197–202. https://doi.org/10.1007/s00339-008-4481-7.

[158] A. Koujelev, M. Sabsabi, V. Motto-Ros, S. Laville, S.L. Lui, Laser-induced breakdown spectroscopy with artificial neural network processing for material identification, Planet. Space Sci. 58 (2010) 682–690. https://doi.org/10.1016/j.pss.2009.06.022.

[159] X. Li, S. Yang, R. Fan, X. Yu, D. Chen, Discrimination of soft tissues using laser-induced breakdown spectroscopy in combination with k nearest neighbors (kNN) and support vector machine (SVM) classifiers, Opt. Laser Technol. 102 (2018) 233–239. https://doi.org/10.1016/j.optlastec.2018.01.028.

[160] V.K. Unnikrishnan, K.S. Choudhari, S.D. Kulkarni, R. Nayak, V.B. Kartha, C. Santhosh, Analytical predictive capabilities of Laser Induced Breakdown Spectroscopy (LIBS) with Principal Component Analysis (PCA) for plastic classification, RSC Adv. 3 (2013) 25872. https://doi.org/10.1039/c3ra44946g.

[161] C.A. Akpovo, J.A. Martinez Jr, D.E. Lewis, J. Branch, A. Schroeder, M.D. Edington, L. Johnson, Regional discrimination of oysters using laser-induced breakdown spectroscopy, Anal. Methods. 5 (2013) 3956. https://doi.org/10.1039/c3ay40491a.

[162] D.F. Andrade, E.R. Pereira-Filho, Direct Determination of Contaminants and Major and Minor Nutrients in Solid Fertilizers Using Laser-Induced Breakdown Spectroscopy (LIBS), J. Agric. Food Chem. 64 (2016) 7890–7898. https://doi.org/10.1021/acs.jafc.6b04028.

[163] D.A. Rusak, A.E. Zeleniak, J.L. Obuhosky, S.M. Holdren, C.A. Noldy, Quantitative determination of calcium, magnesium, and zinc in fingernails by laser-induced breakdown spectroscopy, Talanta. 117 (2013) 55–59. https://doi.org/10.1016/j.talanta.2013.08.022.

[164] V. Sturm, R. Fleige, M. de Kanter, R. Leitner, K. Pilz, D. Fischer, G. Hubmer, R. Noll, Laser-Induced Breakdown Spectroscopy for 24/7 Automatic Liquid Slag Analysis at a Steel Works, Anal. Chem. 86 (2014) 9687–9692. https://doi.org/10.1021/ac5022425.

[165] V.K. Unnikrishnan, R. Nayak, P. Devangad, M.M. Tamboli, C. Santhosh, G.A. Kumar, D.K. Sardar, Calibration based laser-induced breakdown spectroscopy (LIBS) for quantitative analysis of doped rare earth elements in phosphors, Mater. Lett. 107 (2013) 322–324. https://doi.org/10.1016/j.matlet.2013.06.036.

[166] R.J. Lasheras, C. Bello-Gálvez, J.M. Anzano, Quantitative analysis of oxide materials by laser-induced breakdown spectroscopy with argon as an internal standard, Spectrochim. Acta Part B At. Spectrosc. 82 (2013) 65–70. https://doi.org/10.1016/j.sab.2013.01.005.

[167] G. Bilge, B. Sezer, K.E. Eseller, H. Berberoglu, H. Koksel, I.H. Boyaci, Ash analysis of flour sample by using laser- i nduced breakdown spectroscopy, Spectrochim. Acta Part B At. Spectrosc. 124 (2016) 74–78. https://doi.org/10.1016/j.sab.2016.08.023.

[168] G. Bilge, B. Sezer, K.E. Eseller, H. Berberoglu, A. Topcu, I.H. Boyaci, Determination of whey adulteration in milk powder by using laser induced breakdown spectroscopy, Food Chem. 212 (2016) 183–188. https://doi.org/10.1016/j.foodchem.2016.05.169.

[169] R.B. Anderson, R.V. Morris, S.M. Clegg, J.F. Bell, R.C. Wiens, S.D. Humphries, S.A. Mertzman, T.G. Graff, R. McInroy, The influence of multivariate analysis methods and target grain size on the accuracy of remote quantitative chemical analysis of rocks using laser induced breakdown spectroscopy, Icarus. 215 (2011) 608–627. https://doi.org/10.1016/j.icarus.2011.07.034.

[170] Z. Hou, Z. Wang, T. Yuan, J. Liu, Z. Li, W. Ni, A hybrid quantification model and its application for coal analysis using laser induced breakdown spectroscopy, J. Anal. At. Spectrom. 31 (2016) 722–736. https://doi.org/10.1039/C5JA00475F.

[171] T. Yuan, Z. Wang, Z. Li, W. Ni, J. Liu, A partial least squares and wavelet-transform hybrid model to analyze carbon content in coal using laser-induced breakdown spectroscopy, Anal. Chim. Acta. 807 (2014) 29–35. https://doi.org/10.1016/j.aca.2013.11.027.

[172] Z. Wang, Y. Chu, F. Chen, Z. Sheng, L. Guo, Multivariate quantitative analysis of metal elements in steel using laser-induced breakdown spectroscopy, Appl. Opt. 58 (2019) 7615. https://doi.org/10.1364/AO.58.007615.

[173] K.K. Ayyalasomayajula, F. Yu-Yueh, J.P. Singh, D.L. McIntyre, J. Jain, Application of laser-induced breakdown spectroscopy for total carbon quantification in soil samples, Appl. Opt. 51 (2012) B149. https://doi.org/10.1364/AO.51.00B149.

[174] Zhang Xu, Yao Ming-Yin, Liu Mu-Hua, Key Laboratory of Optics-Electronics Application of Biomaterials, College of Engineering, Jiangxi Agricultural University, Nanchang 330045, China, Quantitative analysis of cadmium in navel orange by laser-induced breakdown spectroscopy combined with partial least squares, Acta Phys. Sin. 62 (2013) 044211. https://doi.org/10.7498/aps.62.044211.

[175] K. Li, L. Guo, C. Li, X. Li, M. Shen, Z. Zheng, Y. Yu, R. Hao, Z. Hao, Q. Zeng, Y. Lu, X. Zeng, Analytical-performance improvement of laser-induced breakdown spectroscopy for steel using multi-spectral-line calibration with an artificial neural network, J. Anal. At. Spectrom. 30 (2015) 1623–1628. https://doi.org/10.1039/C5JA00089K.

[176] T. Zhang, S. Wu, J. Dong, J. Wei, K. Wang, H. Tang, X. Yang, H. Li, Quantitative and classification analysis of slag samples by laser induced breakdown spectroscopy (LIBS) coupled with support vector machine (SVM) and partial least square (PLS) methods, J. Anal. At. Spectrom. 30 (2015) 368–374. https://doi.org/10.1039/C4JA00421C.

[177] J. Yang, C. Yi, J. Xu, X. Ma, A laser induced breakdown spectroscopy quantitative analysis method based on the robust least squares support vector machine regression model, J. Anal. At. Spectrom. 30 (2015) 1541–1551. https://doi.org/10.1039/C5JA00009B.

[178] S. Wu, T. Zhang, H. Tang, K. Wang, X. Yang, H. Li, Quantitative analysis of nonmetal elements in steel using laser-induced breakdown spectroscopy combined with random forest, Anal. Methods. 7 (2015) 2425–2432. https://doi.org/10.1039/C4AY02601B.

[179] J. El Haddad, M. Villot-Kadri, A. Ismaël, G. Gallou, K. Michel, D. Bruyère, V. Laperche, L. Canioni, B. Bousquet, Artificial neural network for on-site quantitative analysis of soils using laser induced breakdown spectroscopy, Spectrochim. Acta Part B At. Spectrosc. 79–80 (2013) 51–57. https://doi.org/10.1016/j.sab.2012.11.007.

[180] Wang Chun-Long, Liu Jian-Guo, Zhao Nan-Jing, Ma Ming-Jun, Wang Yin, Hu Li, Zhang Da-Hai, Yu Yang, Meng De-Shuo, Zhang Wei, Liu Jing, Zhang Yu-Jun, Liu Wen-Qing, Key Laboratory of Environment Optics and Technology, Institute of Anhui Optics Fine Mechanics, Chinese Academy of Sciences, Hefei 230031, China, Comparative analysis of quantitative method on heavy metal detection in water with laser-induced breakdown spectroscopy, Acta Phys. Sin. 62 (2013) 125201. https://doi.org/10.7498/aps.62.125201.

[181] T. Zhang, L. Liang, K. Wang, H. Tang, X. Yang, Y. Duan, H. Li, A novel approach for the quantitative analysis of multiple elements in steel based on laser-induced breakdown spectroscopy (LIBS) and random forest regression (RFR), J Anal Spectrom. 29 (2014) 2323–2329. https://doi.org/10.1039/C4JA00217B.

[182] R. Gaudiuso, M. Dell'Aglio, O. De Pascale, S. Loperfido, A. Mangone, A. De Giacomo, Laser-induced breakdown spectroscopy of archaeological findings with calibration-free inverse method: Comparison with classical laser-induced breakdown spectroscopy and conventional techniques, Anal. Chim. Acta. 813 (2014) 15–24. https://doi.org/10.1016/j.aca.2014.01.020.

[183] E. D'Andrea, S. Pagnotta, E. Grifoni, S. Legnaioli, G. Lorenzetti, V. Palleschi, B. Lazzerini, A hybrid calibration-free/artificial neural networks approach to the quantitative analysis of LIBS spectra, Appl. Phys. B. 118 (2015) 353–360. https://doi.org/10.1007/s00340-014-5990-z.

[184] Z. Wang, C. Yan, J. Dong, T. Zhang, J. Wei, H. Li, Acidity analysis of iron ore based on calibration-free laser-induced breakdown spectroscopy (CF-LIBS) combined with a binary search algorithm (BSA), RSC Adv. 6 (2016) 76813–76823. https://doi.org/10.1039/C6RA13038K.

[185] J. Dong, L. Liang, J. Wei, H. Tang, T. Zhang, X. Yang, K. Wang, H. Li, A method for improving the accuracy of calibration-free laser-induced breakdown spectroscopy (CF-LIBS) using determined plasma temperature by genetic algorithm (GA), J. Anal. At. Spectrom. 30 (2015) 1336–1344. https://doi.org/10.1039/C4JA00470A.

[186] W.S. Mcculloch, W. Pitts, A LOGICAL CALCULUS OF THE IDEAS IMMANENT IN NERVOUS ACTIVITY, (n.d.) 17.

[187] P.J. Werbos, Backpropagation through time: what it does and how to do it, Proc. IEEE. 78 (1990) 1550–1560. https://doi.org/10.1109/5.58337.

[188] D.E. Rumelhart, G.E. Hinton, R.J. Williams, Learning Internal Representations by Error Propagation, in: Parallel Distrib. Process. Explor. Microstruct. Cogn. Vol 1 Found., MIT Press, Cambridge, MA, USA, 1986: pp. 318–362.

[189] T. Kohonen, Self-organized formation of topologically correct feature maps, Biol. Cybern. 43 (1982) 59–69. https://doi.org/10.1007/BF00337288.

[190] J. J. HOPFIELD, Neural networks and physical systems with emergent collective computational abilities, Proc. NatL Acad. Sci. USA. (1982). https://doi.org/10.1073/pnas.79.8.2554.

[191] M.J.D. POWELL, Radial basis functions for multivariable interpolation : A review, Algorithms Approx. (1987). https://ci.nii.ac.jp/naid/10000092862/en/.

[192] R.J. Williams, D. Zipser, A Learning Algorithm for Continually Running Fully Recurrent Neural Networks, Neural Comput. 1 (1989) 270–280. https://doi.org/10.1162/neco.1989.1.2.270.

[193] Atomic spectral line database from CD-ROM 23 of R. L. Kurucz., (n.d.). https://www.cfa.harvard.edu/amp/ampdata/kurucz23/sekur.html (accessed February 16, 2021).

[194] V. Motto-Ros, S. Moncayo, F. Trichard, F. Pelascini, Investigation of signal extraction in the frame of laser induced breakdown spectroscopy imaging, Spectrochim. Acta Part B At. Spectrosc. 155 (2019) 127–133. https://doi.org/10.1016/j.sab.2019.04.004.

[195] W. Huang, S. Foo, Neural network modeling of salinity variation in Apalachicola River, Water Res. 36 (2002) 356–362. https://doi.org/10.1016/S0043-1354(01)00195-6.

[196] L. Jolivet, M. Leprince, S. Moncayo, L. Sorbier, C.-P. Lienemann, V. Motto-Ros, Review of the recent advances and applications of LIBS-based imaging, Spectrochim. Acta Part B At. Spectrosc. 151 (2019) 41–53. https://doi.org/10.1016/j.sab.2018.11.008.

[197] R. Gaudiuso, N. Melikechi, Z.A. Abdel-Salam, M.A. Harith, V. Palleschi, V. Motto-Ros, B. Busser, Laser-induced breakdown spectroscopy for human and animal health: A review, Spectrochim. Acta Part B At. Spectrosc. 152 (2019) 123–148. https://doi.org/10.1016/j.sab.2018.11.006.

[198] C. Fabre, D. Devismes, S. Moncayo, F. Pelascini, F. Trichard, A. Lecomte, B. Bousquet, J. Cauzid, V. Motto-Ros, Elemental imaging by laser-induced breakdown spectroscopy for the geological characterization of minerals, J. Anal. At. Spectrom. 33 (2018) 1345–1353. https://doi.org/10.1039/C8JA00048D.

[199] J.O. Cáceres, F. Pelascini, V. Motto-Ros, S. Moncayo, F. Trichard, G. Panczer, A. Marín-Roldán, J.A. Cruz, I. Coronado, J. Martín-Chivelet, Megapixel multi-elemental imaging by Laser-Induced Breakdown Spectroscopy, a technology with considerable potential for paleoclimate studies, Sci. Rep. 7 (2017) 1–11. https://doi.org/10.1038/s41598-017-05437-3.

[200] F. Trichard, F. Gaulier, J. Barbier, D. Espinat, B. Guichard, C.-P. Lienemann, L. Sorbier, P. Levitz, V. Motto-Ros, Imaging of alumina supports by laser-induced breakdown spectroscopy: A new tool to understand the diffusion of trace metal impurities, J. Catal. 363 (2018) 183–190. https://doi.org/10.1016/j.jcat.2018.04.013.

[201] V. Motto-Ros, L. Sancey, X.C. Wang, Q.L. Ma, F. Lux, X.S. Bai, G. Panczer, O. Tillement, J. Yu, Mapping nanoparticles injected into a biological tissue using laser-induced breakdown spectroscopy, Spectrochim. Acta Part B At. Spectrosc. 87 (2013) 168–174. https://doi.org/10.1016/j.sab.2013.05.020.

[202] Q. Wu, C. Marina-Montes, J.O. Cáceres, J. Anzano, V. Motto-Ros, L. Duponchel, Interesting features finder (IFF): Another way to explore spectroscopic imaging data sets giving minor compounds and traces a chance to express themselves, Spectrochim. Acta Part B At. Spectrosc. 195 (2022) 106508. https://doi.org/10.1016/j.sab.2022.106508.

[203] A. Nardecchia, A. de Juan, V. Motto-Ros, M. Gaft, L. Duponchel, Data fusion of LIBS and PIL hyperspectral imaging: Understanding the luminescence phenomenon of a complex mineral sample, Anal. Chim. Acta. 1192 (2022) 339368. https://doi.org/10.1016/j.aca.2021.339368.

LIST OF PUBLICATION AND CONFERENCES

PUBLICATIONS

1) Wu, Q.; Marina-Montes, C.; Cáceres, J. O.; Anzano, J.; Motto-Ros, V.; Duponchel, L. Interesting Features Finder (IFF): Another Way to Explore Spectroscopic Imaging Datasets Giving Minor Compounds and Traces a Chance to Express Themselves. *Spectrochim. Acta Part B At. Spectrosc.* **2022**, *195*, 106508. https://doi.org/10.1016/j.sab.2022.106508.

CONFERENCES

International conference

1) *Robust quantitative analysis in Laser-Induced Breakdown Spectroscopy (LIBS) using artificial neural networks*. Q. Wu, V. Motto-Ros, L. Duponchel, Road to CAC2022 (Online, July 2021)
2) *Robust quantitative analysis in Laser-Induced Breakdown Spectroscopy (LIBS) using artificial neural networks (ANN)*. Q. Wu, V. Motto-Ros, L. Duponchel, SCIX 2021(Rhode Island, USA, October 2021)
3) *Robust quantitative analysis in Laser-Induced Breakdown Spectroscopy (LIBS) using artificial neural networks (ANN)*. Q. Wu, V. Motto-Ros, L. Duponchel Chemometrics in Analytical Chemistry 2022 (Rome, Italy, August 2022)
4) *Interesting features finder (IFF): a new tool to better explore big LIBS imaging datasets?* Q. Wu, V. Motto-Ros, L. Duponchel, LIBS 2022 (Bari, Italy, September 2022)
5) *Is there a needle in this haystack?* Q. Wu, V. Motto-Ros, L. Duponchel, SCIX 2022 (Cincinnati, USA, October 2022)

National conference

1) *Multivariate data exploration in LIBS imaging, is there a needle in this haystack?* Q. Wu, V. Motto-Ros, L. Duponchel, Journée LIBS FRANCE (Marseille, France June 2022)